

# Hydrodynamic Analysis and Optimization of a Hinged-type Wave Energy Converter - SeaWEED

by

© *Meng Chen*

A thesis submitted to the  
School of Graduate Studies  
in partial fulfilment of the  
requirements for the degree of  
Master of *Engineering*

Department of *Engineering and Applied Science*  
Memorial University of Newfoundland

*May 2020*

St. John's

Newfoundland

## Abstract

This thesis presents the experimental, numerical and optimization studies on a hinged-type wave energy converter, SeaWEED (Sea Wave Energy Extraction Device), developed by Grey Island Energy. The device is considered as an improved attenuator consisting of four modules connected by adjustable truss structures.

Extensive model tests of a 1:35 scale SeaWEED model with and without the power-take-off (PTO) units have been conducted at the towing tank of Memorial University (MUN). Friction dampers were designed to mimic the PTO systems. Repeated tests were carried out at a few wave frequencies around the region with maximum responses, and good repeatability has been observed.

Potential-flow based time- and frequency- domain programs utilizing the Lagrange multiplier approach have been developed to simulate the dynamics of SeaWEED. In the time-domain program, nonlinear Froude-Krylov forces are calculated over the instantaneous wetted surfaces of the bodies under the wave profile, and the Wheeler Stretching method is applied to compute the wave pressure. The numerical results are compared with the experimental data, and good agreement is achieved.

Optimization studies have been further conducted utilizing the frequency-domain program. Various parameters, including damping coefficients of the PTO systems, lengths of truss structures and the draft of the device, are considered. The uniform design method is used for sampling, and the response surface method is employed for surrogate construction. The desirability optimization method is utilized to optimize the response. An optimal combination of parameters is determined for an intended operation site.

## Acknowledgements

First of all, I would like to express my deepest gratitude to my supervisor, Dr. Heather Peng, for her patient and invaluable academic guidance, enthusiastic encouragement, and kindness throughout my study at MUN. With her insight, support, and suggestions, I have developed a good knowledge and great interest in my research field. I am also grateful that I have the opportunity to involve in the SeaWEED project.

I would also like to thank Dr. Wei Qiu, for his professional advice and support for this work. Taking his two insightful courses helped me develop my programming skills and professional knowledge in marine hydrodynamics.

My gratitude is also extended to Brian Lundrigan, Trevor Clark, Matt Curtis, and Craig Mitchell for their kind help during the model tests. I would also like to thank the work term students, Min Zhang, Kyle Stanley, Craig Thompson, Sara White, Jackie Zhang, Florence Panisset, and Simon Xu, for their contribution to the project. Furthermore, I am grateful to my colleagues in AMHL, especially Yuzhu Li, who helped to me at the early stages of the SeaWEED project.

I would like to give special thanks to Wei Meng, who is my colleague and also my husband, for his support and concern on my academic research and my life. Moreover, I would like to thank my parents and parents-in-law for their unconditional love, support, and understanding during my entire study.

# Contents

<b>Abstract</b>	<b>ii</b>
<b>Acknowledgements</b>	<b>iii</b>
<b>List of Tables</b>	<b>viii</b>
<b>List of Figures</b>	<b>ix</b>
<b>1 Introduction</b>	<b>1</b>
1.1 Background . . . . .	1
1.1.1 Wave Energy Converters . . . . .	2
1.1.1.1 Oscillating Water Columns . . . . .	3
1.1.1.2 Oscillating Bodies . . . . .	5
1.1.1.3 Overtopping Devices . . . . .	7
1.1.2 SeaWEED (Sea Wave Energy Extraction Device) . . . . .	9
1.1.3 Constrained Dynamics . . . . .	9
1.1.4 Optimization of Simulation-based Design . . . . .	11
1.1.4.1 Selecting Sampling Points . . . . .	12
1.1.4.2 Constructing and Exploiting a Surrogate . . . . .	14

1.1.4.3	Wave Energy Converter Optimization . . . . .	16
1.2	Overview . . . . .	17
<b>2</b>	<b>Introduction and Model Tests of SeaWEED</b>	<b>19</b>
2.1	Introduction of SeaWEED . . . . .	19
2.2	Model Tests on the First Generation of SeaWEED . . . . .	22
2.3	Model Tests on the Second Generation of SeaWEED . . . . .	25
2.3.1	Test Matrix . . . . .	27
2.3.2	Test Set-up . . . . .	30
2.3.3	Pre-tests . . . . .	31
2.3.3.1	Wave Probe Calibration . . . . .	32
2.3.3.2	Load Cell Calibration . . . . .	32
2.3.3.3	Displacement Sensor Calibration . . . . .	35
2.3.3.4	Damper Calibration . . . . .	35
2.3.3.5	Synchronization of Measurements . . . . .	37
2.3.4	Experimental Data-processing . . . . .	39
<b>3</b>	<b>Time-domain Simulation of SeaWEED</b>	<b>43</b>
3.1	Mathematical Formulation . . . . .	44
3.1.1	Coordinate System Definition . . . . .	44
3.1.2	Equations of Motion . . . . .	44
3.1.3	Computation of Constraint Forces . . . . .	47
3.1.4	Computation of Nonlinear Froude-Krylov Forces . . . . .	50
3.1.5	Convergence Studies . . . . .	52
3.1.5.1	Convergence Studies on Mesh . . . . .	52

3.1.5.2	Convergence Studies on Time Step . . . . .	53
3.2	Validation Studies . . . . .	54
3.2.1	Free Hinge Conditions . . . . .	55
3.2.2	Damped Conditions . . . . .	60
<b>4</b>	<b>Frequency-domain Simulation of SeaWEED</b>	<b>72</b>
4.1	Mathematical Formulation . . . . .	72
4.1.1	Equations of Motion and Constraint Matrix . . . . .	73
4.1.2	Power Absorption in Regular and Irregular Waves . . . . .	75
4.2	Validation Studies . . . . .	77
4.2.1	First Generation SeaWEED Simulation . . . . .	77
4.2.2	Second Generation SeaWEED Simulation . . . . .	79
4.2.2.1	Free-hinged Conditions . . . . .	80
4.2.2.2	Damped Conditions . . . . .	84
<b>5</b>	<b>Optimization of the Second Generation of SeaWEED</b>	<b>95</b>
5.1	Optimization Problem . . . . .	96
5.2	Selection of Sample Points . . . . .	96
5.3	Surrogate Model Construction . . . . .	97
5.4	Optimal Response Exploration . . . . .	98
5.5	Optimization of SeaWEED . . . . .	100
5.5.1	Optimization Problem Definition . . . . .	100
5.5.2	Selection of Sampling Points and Levels . . . . .	102
5.5.3	Optimization Results . . . . .	106

<b>6 Conclusions and Future Work</b>	<b>110</b>
<b>Bibliography</b>	<b>112</b>

# List of Tables

2.1	Particulars of SeaWEED (first generation) . . . . .	24
2.2	Particulars of SeaWEED (second generation) . . . . .	27
2.3	Truss length combinations . . . . .	28
2.5	Damping cases . . . . .	28
2.4	Test matrix . . . . .	29
2.6	Scaling of quantities . . . . .	42
5.1	Geometrical design variables (full-scale) . . . . .	101
5.2	PTO damping coefficients (full-scale) . . . . .	101
5.3	Geometrical design variable level combination . . . . .	103
5.4	<i>CD</i> value . . . . .	103
5.5	Adjusted R-squared value . . . . .	104
5.6	Average error . . . . .	106
5.7	Optimal parameters (full-scale) . . . . .	107

# List of Figures

1.1	Category of WECs Based on Working Principles (IEA, 2012) . . . . .	2
1.2	WEC Working Principles (Day et al., 2015) . . . . .	3
1.3	Fixed OWCs (Falcão et al., 2000 and Torre-Enciso et al., 2009) . . . . .	4
1.4	LeanCon WEC (LeanCon) . . . . .	4
1.5	Pelamis (Yemm et al., 2012) . . . . .	5
1.6	Point Absorbers . . . . .	6
1.7	Oscillating Wave Surge Converters (AW-Energy and Renzi et al., 2014) . . . . .	7
1.8	Seawave Slot-Cone Generator (Vicinanze et al., 2008) . . . . .	8
1.9	Wave Dragon (Kofoed et al., 2006) . . . . .	8
1.10	The First Generation of SeaWEED . . . . .	10
1.11	The Second Generation of SeaWEED . . . . .	10
2.1	SeaWEED PTO System . . . . .	21
2.2	SeaWEED Ballast Tank . . . . .	22
2.3	General Arrangement of the Basin (NRC) . . . . .	23
2.4	SeaWEED Model in the NRC-IOT Basin . . . . .	23
2.5	Body and Tie-rod Length Definition . . . . .	24
2.6	Towing Tank of MUN . . . . .	26

2.7	SeaWEED Model in the Towing Tank . . . . .	26
2.8	Body and Truss Length Definition . . . . .	27
2.9	Test Set-up . . . . .	30
2.10	Friction Damper . . . . .	31
2.11	Friction Damper . . . . .	32
2.12	Wave Probe Calibration . . . . .	33
2.13	Wave Probe Calibration Results (WP3) . . . . .	33
2.14	Honeywell Model-31 Load Cell . . . . .	34
2.15	Load Cell Calibration Results (PTO-2) . . . . .	34
2.16	Displacement Sensor Calibration Results (PTO-2) . . . . .	35
2.17	Damper Calibration Apparatus . . . . .	36
2.18	Damper Calibration Results (D1) . . . . .	37
2.19	Damper Calibration Results (D2, D3 and D4) . . . . .	38
2.20	Damper Calibration Results (D5) . . . . .	38
2.21	Synchronization Input by Module NI9264 . . . . .	39
2.22	Relative Pitch Angles . . . . .	40
2.23	Damping Force and Sliding Velocity . . . . .	40
3.1	Coordinate Systems . . . . .	44
3.2	Damping Moments . . . . .	47
3.3	SeaWEED Wetted Surfaces under Waves . . . . .	50
3.4	Illustration of Wheeler Stretching Theory . . . . .	51
3.5	Convergence Study on the Mesh Size . . . . .	53
3.6	Time Histories of Simulated Hinge Motions . . . . .	54

3.7	Time Histories of Relative Displacement Error . . . . .	55
3.8	Non-dimensional Relative Pitch Angles at PTO-1 (Case T1-D0) . . .	56
3.9	Non-dimensional Relative Pitch Angles at PTO-2 (Case T1-D0) . . .	57
3.10	Non-dimensional Relative Pitch Angles at PTO-1 (Case T2-D0) . . .	57
3.11	Non-dimensional Relative Pitch Angles at PTO-2 (Case T2-D0) . . .	58
3.12	Non-dimensional Relative Pitch Angles at PTO-1 (Case T3-D0) . . .	58
3.13	Non-dimensional Relative Pitch Angles at PTO-2 (Case T3-D0) . . .	59
3.14	Non-dimensional Relative Pitch Angles at PTO-1 (Case T4-D0) . . .	59
3.15	Non-dimensional Relative Pitch Angles at PTO-2 (Case T4-D0) . . .	60
3.16	Non-dimensional Relative Pitch Angles at PTO-1 (Case T1-D1) . . .	61
3.17	Non-dimensional Relative Pitch Angles at PTO-2 (Case T1-D1) . . .	62
3.18	Full-scale Capture Width at PTO-1 (Case T1-D1) . . . . .	62
3.19	Full-scale Capture Width at PTO-2 (Case T1-D1) . . . . .	63
3.20	Non-dimensional Relative Pitch Angles at PTO-1 (Case T1-D2) . . .	63
3.21	Non-dimensional Relative Pitch Angles at PTO-2 (Case T1-D2) . . .	64
3.22	Full-scale Capture Width at PTO-1 (Case T1-D2) . . . . .	64
3.23	Full-scale Capture Width at PTO-2 (Case T1-D2) . . . . .	65
3.24	Non-dimensional Relative Pitch Angles at PTO-1 (Case T1-D3) . . .	65
3.25	Non-dimensional Relative Pitch Angles at PTO-2 (Case T1-D3) . . .	66
3.26	Full-scale Capture Width at PTO-1 (Case T1-D3) . . . . .	66
3.27	Non-dimensional Relative Pitch Angles at PTO-1 (Case T1-D4) . . .	67
3.28	Non-dimensional Relative Pitch Angles at PTO-2 (Case T1-D4) . . .	68
3.29	Full-scale Capture Width at PTO-2 (Case T1-D4) . . . . .	68
3.30	Non-dimensional Relative Pitch Angles at PTO-1 (Case T1-D5) . . .	69

3.31	Non-dimensional Relative Pitch Angles at PTO-2 (Case T1-D5) . . . . .	69
3.32	Full-scale Capture Width at PTO-1 (Case T1-D5) . . . . .	70
3.33	Full-scale Capture Width at PTO-2 (Case T1-D5) . . . . .	70
4.1	Relative Pitch Angles . . . . .	74
4.2	Non-dimensional Relative Pitch Angles at PTO-1 . . . . .	78
4.3	Non-dimensional Relative Pitch Angles at PTO-1 . . . . .	78
4.4	Full-scale Capture Width at PTO-1 . . . . .	79
4.5	Non-dimensional Relative Pitch Angles at PTO-1 (Case T1-D0) . . . . .	80
4.6	Non-dimensional Relative Pitch Angles at PTO-2 (Case T1-D0) . . . . .	81
4.7	Non-dimensional Relative Pitch Angles at PTO-1 (Case T2-D0) . . . . .	81
4.8	Non-dimensional Relative Pitch Angles at PTO-2 (Case T2-D0) . . . . .	82
4.9	Non-dimensional Relative Pitch Angles at PTO-1 (Case T3-D0) . . . . .	82
4.10	Non-dimensional Relative Pitch Angles at PTO-2 (Case T3-D0) . . . . .	83
4.11	Non-dimensional Relative Pitch Angles at PTO-1 (Case T4-D0) . . . . .	83
4.12	Non-dimensional Relative Pitch Angles at PTO-2 (Case T4-D0) . . . . .	84
4.13	Non-dimensional Relative Pitch Angles at PTO-1 (Case T1-D1) . . . . .	85
4.14	Non-dimensional Relative Pitch Angles at PTO-2 (Case T1-D1) . . . . .	85
4.15	Full-scale Capture Width at PTO-1 (Case T1-D1) . . . . .	86
4.16	Full-scale Capture Width at PTO-2 (Case T1-D1) . . . . .	86
4.17	Non-dimensional Relative Pitch Angles at PTO-1 (Case T1-D2) . . . . .	87
4.18	Non-dimensional Relative Pitch Angles at PTO-2 (Case T1-D2) . . . . .	87
4.19	Full-scale Capture Width at PTO-1 (Case T1-D2) . . . . .	88
4.20	Full-scale Capture Width at PTO-2 (Case T1-D2) . . . . .	88

4.21	Non-dimensional Relative Pitch Angles at PTO-1 (Case T1-D3) . . .	89
4.22	Non-dimensional Relative Pitch Angles at PTO-2 (Case T1-D3) . . .	90
4.23	Full-scale Capture Width at PTO-1 (Case T1-D3) . . . . .	90
4.24	Non-dimensional Relative Pitch Angles at PTO-1 (Case T1-D4) . . .	91
4.25	Non-dimensional Relative Pitch Angles at PTO-2 (Case T1-D4) . . .	91
4.26	Full-scale Capture Width at PTO-2 (Case T1-D4) . . . . .	92
4.27	Non-dimensional Relative Pitch Angles at PTO-1 (Case T1-D5) . . .	92
4.28	Non-dimensional Relative Pitch Angles at PTO-2 (Case T1-D5) . . .	93
4.29	Full-scale Capture Width at PTO-1 (Case T1-D5) . . . . .	93
4.30	Full-scale Capture Width at PTO-2 (Case T1-D5) . . . . .	94
5.1	Wave Climate Table off Cork Harbour in Ireland . . . . .	100
5.2	Damping Optimization . . . . .	102
5.3	Verification of RSM . . . . .	105
5.4	Response Surfaces for Annual Power Absorption . . . . .	108
5.5	Power Matrix of SeaWEED . . . . .	109

# Chapter 1

## Introduction

### 1.1 Background

During the past decades, renewable wave energy has become a research focus due to the ever-increasing energy consumption demand and environmental issues. Waves are created by wind blowing over the ocean surface and can travel a great distance with little energy loss (Clément et al., 2002). Comparing to other forms of renewable energies, wave energy has a relatively less adverse impact on the environment, larger energy density and power output efficiency (Drew et al., 2009). The globally available wave power is estimated as 3.7 TW, which is in the same order of magnitude of the world consumption of electrical energy (Mørk et al., 2010). Although wave-induced electricity generation is not well-developed currently (Pecher et al., 2017), its outstanding benefits encourage many countries to devote efforts into the wave energy conversion field.

### 1.1.1 Wave Energy Converters

Wave energy converters (WECs) are devices that can convert wave energy and generate electricity or other forms of energies (Day et al., 2015). Girard and son proposed the earliest patent of WEC (1799) and the first experiment of WEC was conducted during the 1800s (Gonzalez). In the 1970s, the remarkable energy crisis and a paper by Salter (1974) roused the research interest on wave power at sea. Since then, more than 1000 WEC patents have been proposed (Drew et al., 2009).

WECs can be categorized according to their working principles: oscillating water columns (OWCs), oscillating bodies (OBs), and overtopping devices (Day et al., 2015). Representative WECs of each categorization are given in Fig. 1.1, and the working principles of them are given in Fig. 1.2.

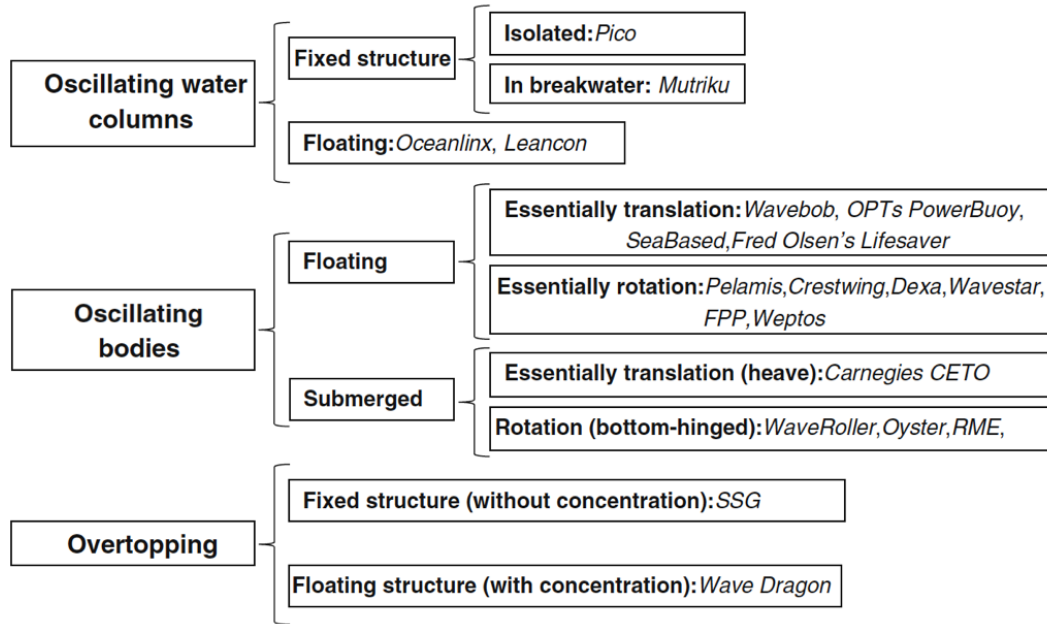


Figure 1.1: Category of WECs Based on Working Principles (IEA, 2012)

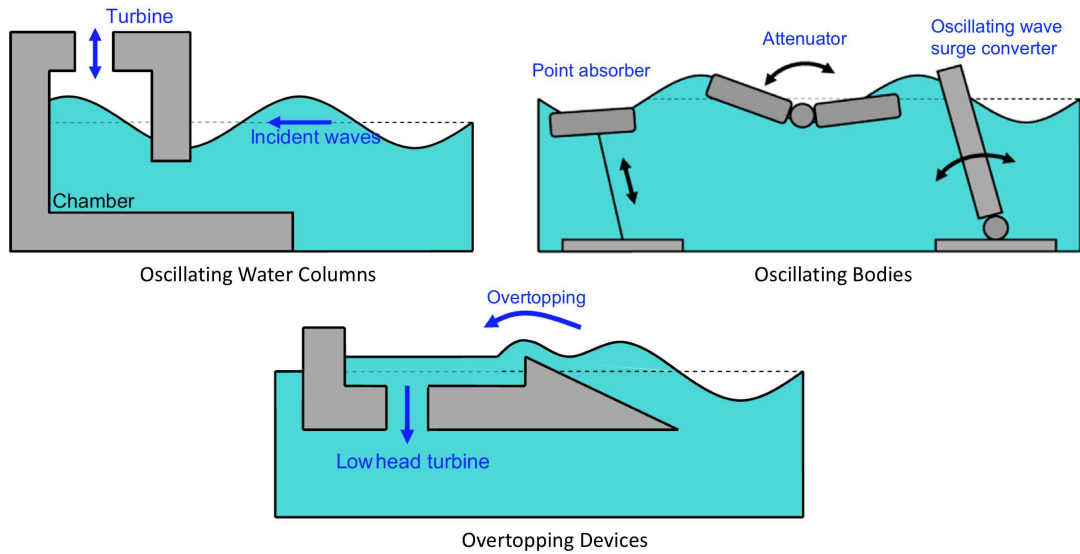


Figure 1.2: WEC Working Principles (Day et al., 2015)

### 1.1.1.1 Oscillating Water Columns

An OWC WEC consists of a semi-submerged chamber open to the sea below. As waves oscillate in the chamber, the air is forced out of the chamber and back into it. The high-velocity air then drives the turbine to generate power, as shown in Fig. 1.2.

OWC devices can be fixed on the seabed, which makes them convenient and economical to construct and maintain, such as the Pico power plant (Falcão et al., 2000) and the Mutriku breakwater wave plant (Torre-Enciso et al., 2009), as shown in Fig. 1.3.

On the other hand, The LeanCon WEC (Kofoed et al., 2008) is a large floating type OWC, which consists of a large number of chambers, as shown in Fig. 1.4. The device covers more than one wave length and utilizes an ordinary wind turbine to generate power. In addition, due to the unique design of non-return valves, the air flow can be rectified before the flow reaches the generator (Kofoed et al., 2008).



Pico Power Plant



Mutriku Breakwater Wave Plant

Figure 1.3: Fixed OWCs (Falcão et al., 2000 and Torre-Enciso et al., 2009)



Figure 1.4: LeanCon WEC (LeanCon)

### 1.1.1.2 Oscillating Bodies

Oscillating body (OB) WECs harvest energy from the relative motions between bodies driven by waves. OB WECs have diverse forms, and they can be further categorized into attenuators, point absorbers, and oscillating wave surge converters, as shown in Fig. 1.2.

The Pelamis WEC, as shown in Fig. 1.5, is a semi-submerged floating attenuator, which converts wave energy into electricity. Its articulated structure is made of five tube sections by the universal hinge joints (Yemm et al., 2012). The device weathers in head seas, and the relative pitch motions drive the hydraulic power-take-off (PTO) systems at the hinge joints.



Figure 1.5: Pelamis (Yemm et al., 2012)

Examples of point absorbers include PowerBuoy (Edwards et al., 2014), Seabased (Seabased Technology) and Wavebob (Mouwen, 2008), as shown in Fig. 1.6. PowerBuoy is a floating WEC which consists of a heave plate rigidly connected to a spar and a float moving along the spar. The float oscillates in response to waves, and the relative motions between the float and the spar drive the PTO hydraulic system and

generate power. Wavebob consists of two oscillating structures, a torus and a tank, and power is generated from the relative motions between the two parts. Different from PowerBuoy and Wavebob which float in the sea, Seabased has a base fixed on the seabed.

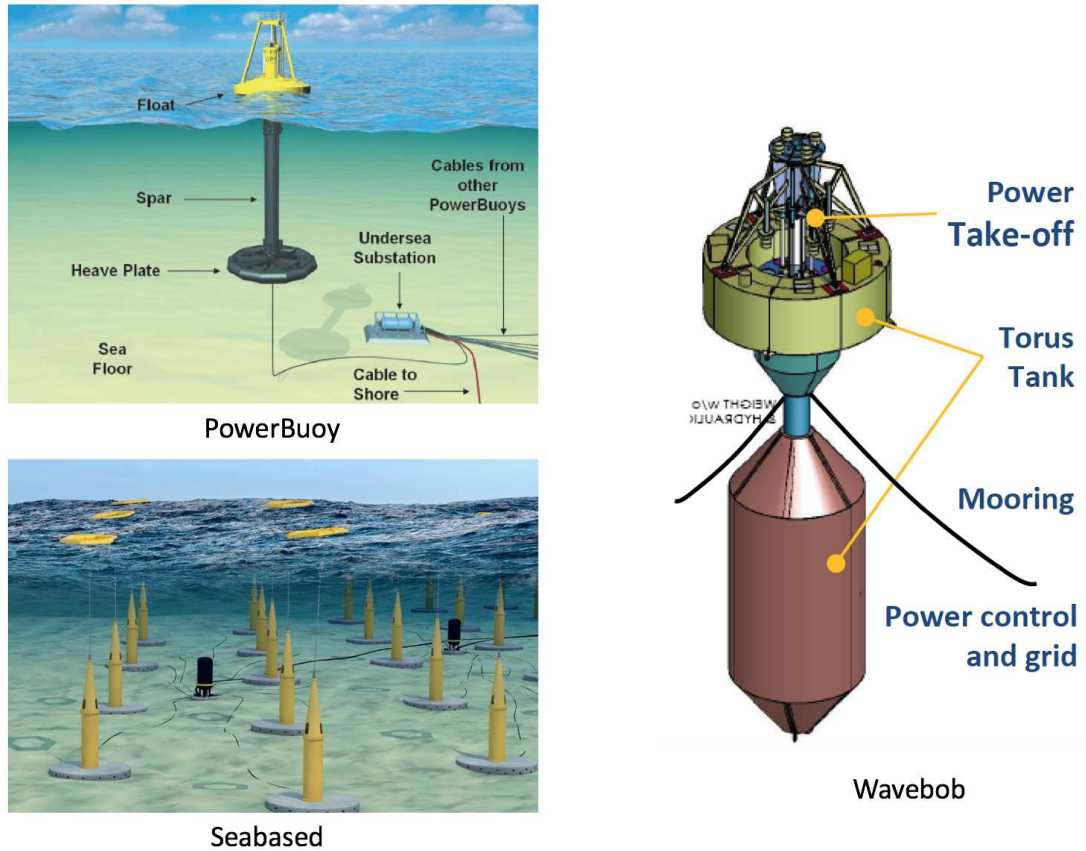


Figure 1.6: Point Absorbers

Among oscillating wave surge converters, examples are WaveRoller (AW-Energy) and Oyster (Renzi et al., 2014), as shown in Fig. 1.7. The lower parts of devices are anchored on the sea bed or fixed to a submerged floating reference frame; while the upper parts move back and forth due to wave surge to drive hydraulic piston pumps

to generate energy.

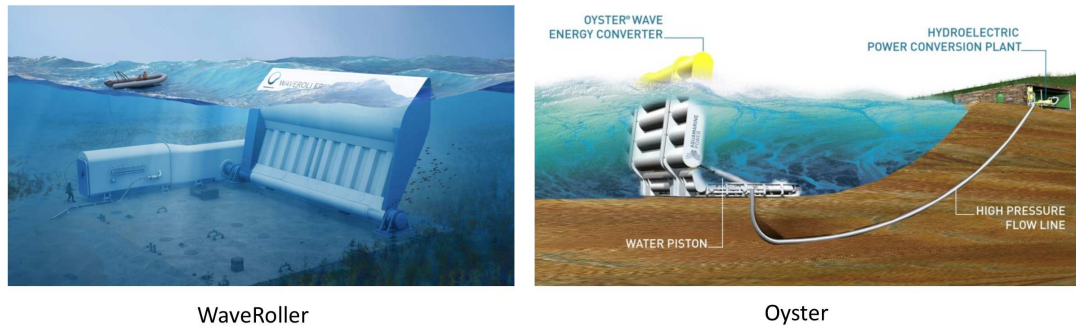


Figure 1.7: Oscillating Wave Surge Converters (AW-Energy and Renzi et al., 2014)

### 1.1.1.3 Overtopping Devices

Overtopping devices capture power as waves flow up a ramp and over the top into a storage reservoir and the water passes through turbines, as shown in Fig. 1.2. Typical examples include the fixed-type Seawave Slot-Cone Generator (SSG) (Margheritini et al., 2009) and floating-type Wave Dragon (Kofoed et al., 2006).

The SSG device is designed to be fixed offshore, as presented in Fig. 1.8, and it is equipped with three reservoirs with different heights to increase power generation efficiency.

As shown in Fig. 1.9, the Wave Dragon WEC has a curved ramp, a large floating reservoir, a platform with two reflectors for concentrating the power of incoming waves, and several low-head hydro turbines (Kofoed et al., 2006).



Figure 1.8: Seawave Slot-Cone Generator (Vicinanza et al., 2008)



Figure 1.9: Wave Dragon (Kofoed et al., 2006)

### **1.1.2 SeaWEED (Sea Wave Energy Extraction Device)**

SeaWEED is an attenuator-type WEC proposed by Grey Island Energy Inc. (GIE), which consists of four modules that are connected by rigid truss structures. The four-module array includes a non-energy producing nose module in the front, followed by two energy producing modules, and another non-energy producing module at the rear.

Initial conceptual studies have been carried out to evaluate the performance of the first generation device (see Fig. 1.10) by testing a 1:16 scale model in the wave basin of National Research Council Canada. The experimental and numerical results for the first generation model led to the second generation (see Fig. 1.11) with improvements in the hull geometry, a lower draft, and a different connection structure.

The device is considered as an improved attenuator in comparison with Pelamis. The use of the rigid truss structure would allow for a higher power output per unit mass, and also reduce the side loading due to tidal currents, local wind or bi-modal swells in comparison with other attenuator devices. Additionally, the trusses can be customized in length to archive high efficiency for a specified site. The design also attempted to address the wave topping and slamming issues encountered by devices such as Pelamis.

### **1.1.3 Constrained Dynamics**

SeaWEED undergoes constrained motions in waves due to the hinged joints. It is therefore essential to accurately predict the constrained motions. Many efforts have been made to solve the dynamics of multiple constrained bodies. Newman (1994)

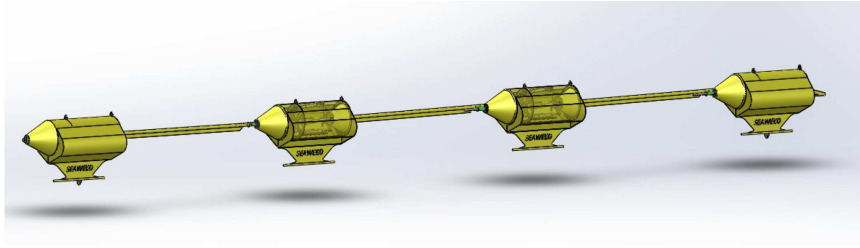


Figure 1.10: The First Generation of SeaWEED

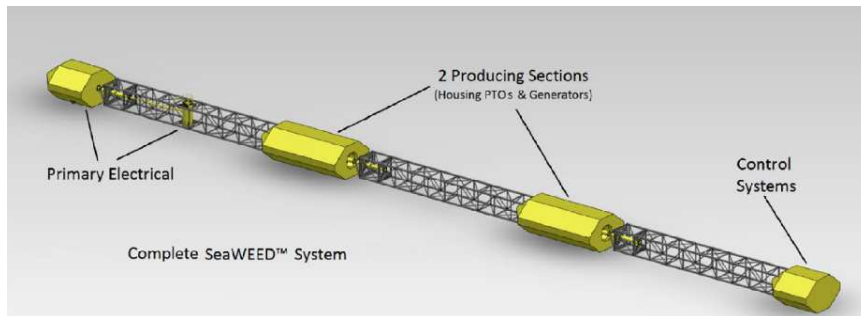


Figure 1.11: The Second Generation of SeaWEED

used arbitrary modal shape functions to describe the body deformation, and solved the motion of a hinged system by using the extended motion modes, i.e., additional vertical motion modes perpendicular to the undisturbed free surface were employed to describe motions of hinge joints. The mode expansion technique was adopted by Lee and Newman (2000) to assess the hydroelastic effects on large arrays of hinged structures. Newton-Euler equations of motion with eliminated constraint forces have been utilized to model a multi-body interconnected WEC system by Ó’Catháin et al. (2008) in time domain. The reduced-coordinate approach removes the redundant degrees of freedom due to constraints.

The Lagrange multiplier method, which has been extensively used in the robotics and gaming industries, is another one to solve constrained motions. Baraff (1996)

presented a Lagrange multiplier based method to simulate constraint motions in the time domain, where various constraints were described by constraint matrices and incorporated into the equations of motions. Constraint motions and forces were solved simultaneously. Catto (2009) used the sequential impulse method to solve multi-constraint motions, where velocities of bodies were first solved without considering the constraints, and the constraint forces were then computed based on the intermediate velocities and constraint matrices to satisfy the constraint conditions.

In ocean engineering field, Sun et al. (2011) applied the Lagrange multiplier technique in the frequency domain. Under linear assumption, a position constraint matrix was combined into equations of motion, and the constrained displacements and forces were obtained directly. The method was employed by Sun et al. (2012) for the dynamic analysis of an installation barge interacting with a substructure of large volume, and by Sun et al. (2016) to predict motions and power of a three-floater WEC. Similar to the method proposed by Baraff (1996), Feng and Bai (2017) investigated the hydrodynamic performance of two freely floating and interconnected barges in the time domain. In their work, the constraints were described by a constraint matrix which was incorporated into equations of motion, and the nonlinearity of the hydrodynamic forces was taken into account.

#### **1.1.4 Optimization of Simulation-based Design**

Simulation-based Design (SBD), or the computer experimental design, can deal with multi-factor and large-domain problems. Because of the deterministic nature of computer experiments, no replication, no randomization, and no blocking are re-

quired.

As for design optimization, the procedure typically starts with the determination of design responses, variables, associated domains and levels according to the problem of interest. A set of sampling points are then selected in the design domains. Based on the selected sample points, surrogate models can be constructed to describe the relationship between the design variables and the responses. After the surrogates are verified, the optimized responses, such as the maximum or the minimum values, can then be determined.

#### **1.1.4.1 Selecting Sampling Points**

Various sampling methods can be employed to select sampling points on the design domain, for example, the full and fractional factorial design method, the Latin Hypercubes sampling method (McKay et al., 2000) and the uniform design method (Fang et al., 2000).

A full factorial design investigates the effect of all the possible combinations of the factors and levels. This leads to a large number of simulations for problems with more factors and levels. Therefore, fractional factorial design is more practical since it requires less test runs.

In order to conduct the same test with less runs than the factorial designs, the concept of the space-filling design is proposed to distribute sample points uniformly in the experimental region (Joseph, 2016). The Latin Hypercube sampling method (LHS) was first proposed by McKay et al. (2000), which was developed based on the stratified sampling. The layered feature of the LHS method enables a large number of input variables and test runs. The method is easy to conduct, and has relatively

small variance (Fang et al., 2000). Moreover, the stratified manner gives the Latin Hypercube Design (LHD) a main advantage that if only one or a few input variables are dominating, the projections onto subspaces will distribute distinctly. However, the LHS method confronts several disadvantages, for example uniform distribution of sampling points in the sample space is not guaranteed. Thus, many efficient extended LHS methods have been proposed to improve the method, such as randomized orthogonal arrays LHD (Tang, 1993) (Owen, 1994), maximin LHD (Morris et al., 1995), orthogonal LHD (Ye, 1998), uniform LHD (Jin et al., 2003), generalized LHD (Dette et al., 2010), and maximum projection LHD (Joseph, 2016).

Another widely utilized sampling method is the Uniform Design (UD) method, which was proposed by Fang et al. (2000). Unlike the randomly uniform feature in the LHS methods, UD is deterministically uniform. The sampling of UD is based on the Good Lattice Point method. For each  $n$ -test-run design with  $s$  factors and  $n$  levels, there is a unique UD table,  $U_n(n^m)$ , to determine the sample points, where  $m$  is the largest factor number that the design table can deal with ( $s \leq m$ ). The uniformity of the UD sampling points is measured by the discrepancy of the sampling points.

To date, many other space-filling design sampling methods have been proposed, such as integrated mean squared error design by Sacks et al. (1989), nested and sliced space-filling design by Qian et al. (2009), fast flexible filling design by Lekivetz et al. (2015), and bridge design by Jones et al. (2015).

#### 1.1.4.2 Constructing and Exploiting a Surrogate

Based on the selected sample points, surrogate models can be constructed to describe the relationship between the design variables and the responses. Several surrogate modeling methods have been proposed. Examples include the Response Surface method (Box et al., 1951), the Kriging method (Sacks et al., 1989) and the Neural Network Model method (Grossberg, 1988). After the surrogates are verified, the optimized responses, such as the maximum or the minimum values, can then be determined. For unimodal-function surrogate models, a local searcher can be applied. On the other hand, for multimodal-function surrogate models, a global searcher can be utilized.

Response Surface Methodology (RSM) was proposed by Box and Wilson (1951), which is based on the polynomial model. RSM is generally utilized to analyze the influence of single or multiple input variables to one or several output variables. This method is a sequential procedure that utilizes small steps to find the optimum responses. The basic search procedure of RSM is a local search procedure by using the steepest ascent and steepest descent methods. However, the number of the required sampling data may increase dramatically as the number of the input variables increase. To overcome the drawbacks, Derringer et al. (1980) purposed a desirability optimization method which combines the desirability function with RSM to optimize single and multiple responses.

The Kriging method, also called the Gaussian process regression method is also widely used in simulation-based experiments and spatial analysis. Comparing to the traditional polynomial model that uses local searchers, the Kriging model is more

suitable for searching in a larger domain utilizing global searchers. The method was first purposed by Krige (1951) and was formally developed by Matheron to conduct spatial analysis (1963). This method utilizes an exact Gaussian process interpolation technique to predict the output variables by calculating the weighted value around the point. In 1989, the Kriging modeling was first introduced to the modeling and optimization in computer experiments (Sacks et al.).

Recently, many new methods are developed based on the Kriging method. For example, the Least Improvement Function method, developed by Sun et al. (2017), applied to structural reliability analysis, and the blind Kriging, developed by Joseph et al. (2008), which is based on a Bayesian variable selection technique, and has a robust performance when dealing with the mis-specification problem (Joseph et al., 2008).

The Neural Network model is generated by adjusting the connection weights between components based on a network function (Grossberg, 1988). The Multilayer Neural Network model (Kůrková, 1992) and the Radial Basis Function Network model (Chen et al., 1991) are the most widely utilized in Neural Network models. Other types of models include the Multivariate Adaptive Regression Splines (Friedman, 1991), the Least Interpolating Polynomials (De Boor et al., 1990), the Inductive Learning (Langley et al., 1995), the Support Vector Regression (Clarke et al., 2005), and the Multi-point Approximation (Toropov et al., 1993).

The local models are usually utilized to search the optimized responses in small experimental domain to fit unimodal functions. Examples are the Newton method (Fischer, 1992) which is an iterative method to find the stationary points of the surrogate function by computing the first and second derivatives, Quasi-Newton method

(Dennis et al., 1977) which is a modification of Newton method by avoiding computing the Hessian matrix in higher dimensions, simplex algorithm (Dantzig, 2016) for linear optimization, Nelder-Mead method (Olsson et al., 1975) for non-linear optimization, and pattern search (derivative-free search) (Hooke et al., 1961) which can be used to search in noncontinuous and non-differentiable spaces.

As for the global searchers, various methods are proposed to search the optima of a non-linear and complicated surrogate. The genetic algorithm was proposed by Holland (1992), which is based on Darwin's theory of evolution. It is a population-based model that utilizes selection and recombination operators to generate accurate solutions in searching the optima (Whitley, 1994). Similar to genetic algorithm, the particle swarm optimization (Eberhart et al., 1995) also starts with a population of random solutions (particles), and the particles flow through the search domain with randomized velocities, which are determined by their own best position and the overall best position of the entire swarm. The velocities of each particle are kept computed and tuned in each time step until the optimal solution is searched.

#### **1.1.4.3 Wave Energy Converter Optimization**

In terms of WEC optimization, the primary objective is to maximize average power extraction for intended operation sites (Khaleghi et al., 2015, Goggins et al., 2014 and Babarit et al., 2005). Basically, geometrical parameters and PTO systems need to be optimized, and several constraints should be set, such as slamming due to large response, the limitation of the WEC motions, and the capacity of the WEC devices (Goggins et al., 2014).

Kofoed et al. (2006) optimized the overall structural geometry, turbines and

reservoir of the Wave Dragon to maximize power production. Babarit et al. (2005) conducted optimization studies on body shape and mechanical features of an oscillating water column WEC, SEAREV, where several constraints were considered, such as static stability, realistic inner pendulum density, and draft of the device.

More recently, Goggins et al. (2014) optimized the geometric shape and the structural radius of an oscillating-body type WEC related to the dynamic heave velocity response of the device. Dai et al. (2017) assessed the performance of an oscillating-body type WEC and optimized the geometry and mechanical parameters of the device. Primary optimization of SeaWEED was conducted by Li et al. (2016), where hinged motions were computed using WAMIT based on the mode expansion method (Newman, 1994). However, since the hinged motions of SeaWEED were described by the vertical movement of joints, it is difficult to incorporate PTO damping into the simulations with WAMIT.

## 1.2 Overview

In this thesis, a hinged-type wave energy converter, SeaWEED, is introduced. Potential-flow based time- and frequency-domain programs with the Lagrange multiplier approach have been developed to simulate the dynamics of constrained multiple bodies, and the numerical results have been validated using model test data. Optimization studies have been further conducted utilizing the frequency-domain program by considering various parameters, including damping coefficients of the PTO systems, lengths of truss structures and the draft of the device.

Chapter 2 describes the design of SeaWEED and model tests. Model tests on the

first generation device (1:16 scale) are then briefly introduced. Following, model tests on the second generation device (1:35 scale) are described in detail, including test preparation, instrument calibration, measurement, data-processing, etc.

Chapter 3 derives the mathematical formulations for the constrained multi-body hydrodynamic interactions in the time domain. The Lagrange multiplier approach is utilized to model the constrained dynamics. Nonlinear Froude-Krylov forces are calculated over the instantaneous wetted surfaces of the bodies. The numerical method is validated using the test data.

Chapter 4 presents the numerical method for solving the constrained multi-body hydrodynamic interactions in the frequency domain. The numerical results are compared against the experimental data.

Chapter 5 elaborates the optimization studies of SeaWEED. Based on the uniform design method for the selection of sample points and the response surface method for surrogate modeling, optimization studies were carried out by considering a variety of parameters, including damping coefficients at the two PTOs, truss lengths, and draft of the device, as independent variables. An optimum combination of these parameters was determined for an intended operation site.

Chapter 6 concludes the current work and brings forward the future work.

# Chapter 2

## Introduction and Model Tests of SeaWEED

### 2.1 Introduction of SeaWEED

SeaWEED consists of floating sections linked by trusses or rods and universal joints. The device has semi-submerged floats on the surface of water and inherently faces into the direction of waves. The wave-induced motions of the floats can be converted to electricity through the hydraulic power-take-off (PTO) systems. Floats are connected by trusses which can be customized in length to archive high efficiency for a specified site. The device is considered as an improved attenuator in comparison with Pelamis (Pizer et al., 2000). The design also attempted to address the wave topping and slamming issues encountered by devices such as Pelamis. A complete device has two PTOs and each PTO is located in the back end of a producing module. Each PTO consists of four double acting hydraulic rams to capture energy from pitch

motions. The use of the rigid truss structure would allow for a higher power output per unit mass, and also reduce the side loading due to tidal currents, local wind or bi-modal swells in comparison with other attenuator devices.

The design of SeaWEED would permit heave, pitch, roll and yaw motions. The electrical power will be only converted from the pitch motion. Inside each module, there is a removable pin. When the pin is removed, each module is allowed to roll independently, which would reduce stress on the entire system thus the risk of failure. Located in each module, surrounding the mechanical space are positive air-pressure ballast tanks. In the occurrence of extreme sea conditions that could damage the system, air valves on these ballast tanks would open and release air, allowing the tanks to be filled with sea water. Once the sea conditions are improved, the tanks can be re-pressurized with air and the water will be discharged. The system can then return to the normal operating condition.

Furthermore, the device can be customized to operate in various locations by changing its truss lengths and draft. It can utilize on-board electrical generator and standard subsea electrical cables to generate and transmit the energy to shore. In term of applications, an offshore farm of SeaWEED WECs can be utilized to provide electricity to coastal communities and by oil and gas companies to power subsea infrastructure.

The proposed SeaWEED PTOs, currently based on the use of a conventional hydraulic system, with the utilization of a linear generator being an alternative possibility, are entirely housed inside the two energy producing modules for maximum protection. The PTO systems, utilizing a water tight multi-axis joint in the stern of each module, are driven by movements between interconnected modules, i.e., the

motion between the interconnected modules drives a swashplate located internally (Fig. 2.1) to tilt in various planes and thus to actuate the hydraulic rams. This PTO design is intended not only to protect all PTO components from the harsh marine environment but also to protect the environment from contamination by possible hydraulic leaks. As shown in Fig. 2.1, each PTO system consists of four hydraulic power capture rams and two horizontal struts. The horizontal struts are primarily for the control of yaw motions but not for energy capturing.

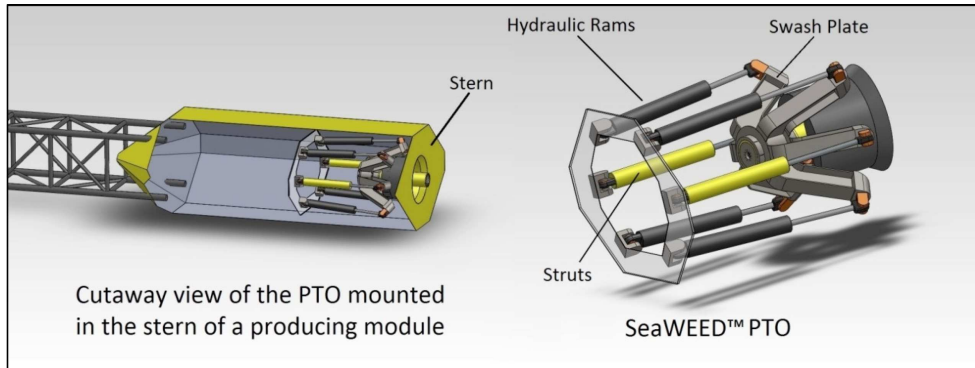


Figure 2.1: SeaWEED PTO System

As for the operational limits, they include both the maximum sea state that a device is capable of producing electricity in and its method and ability to survive severe sea conditions. The present design considers methods of decreasing end-stop issues, through increased flexibility and system damping to increase the operational limits of the system. This is due in part to being an attenuator but more importantly is related to how each module in the system connects and flexes. Based on the PTO design, each section can articulate up to 30 degrees from the neutral axis in any direction before the end-stop becomes an issue. The proposed PTO design aims to

enable the device to arch over entire wavelengths in high sea states. As indicated above, the purpose of the ballast systems is to allow the SeaWEED to semi-submerge when it is in severe sea conditions. The internal tanks are shown in the illustration and highlighted in green (Fig. 2.2).

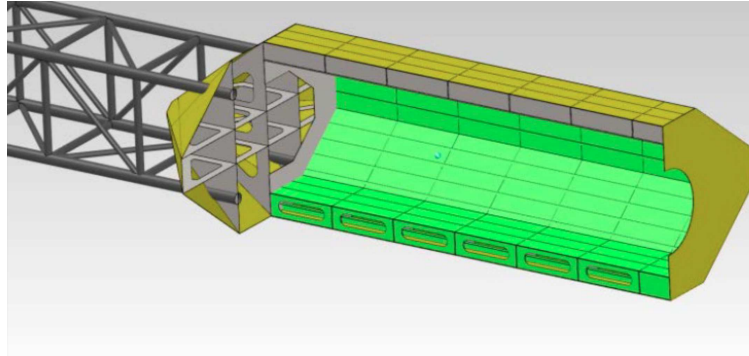


Figure 2.2: SeaWEED Ballast Tank

## 2.2 Model Tests on the First Generation of SeaWEED

Model tests (scale 1 : 16) of the first generation SeaWEED were conducted by Grey Island Energy Inc. (GIE) at the ocean engineering basin of National Research Council-Institute of Ocean Technology (NRC-IOT) in St. John's, NL, Canada. The basin (see Fig. 2.3) is 75 m long, 32 m wide and 3.2 m deep. Fig. 2.4 shows the SeaWEED model in the basin.

As shown in Fig. 2.5, the first generation SeaWEED system consists of four equal-length modules with cambered surfaces connected by three tie-rods with stiffeners.

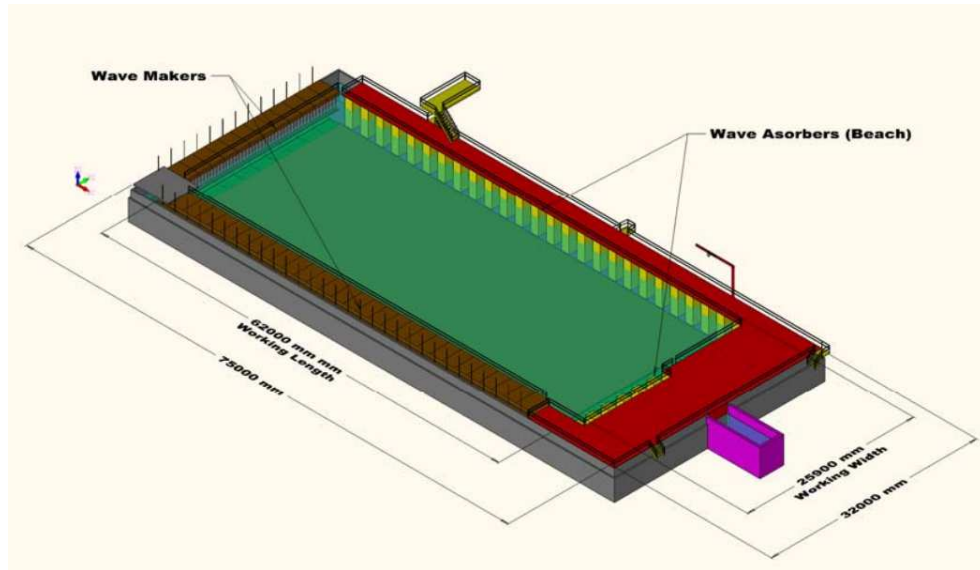


Figure 2.3: General Arrangement of the Basin (NRC)



Figure 2.4: SeaWEED Model in the NRC-IOT Basin

Table 2.1: Particulars of SeaWEED (first generation)

Parameter	Full Scale	1:16 Scale
Total Length, $L(m)$	145.000	9.063
Length of Module, $L_m(m)$	16.000	1.000
Length of Tie-rod, $L_t(m)$	27.000	1.688
Width, $B(m)$	8.800	0.550
Height, $H(m)$	6.880	0.430
Planned Draft, $T_{plan}(m)$ ,	2.500	0.156
Test Draft, $T_{test}(m)$ ,	4.480	0.280

The principle dimensions of the first generation SeaWEED and the 1 : 16 model are defined in Fig. 2.5 and Table 2.1. During the tests, the relative pitch angles at PTO-1 were measured. Two hydraulic PTO systems were built to simulate the power capturing procedure of SeaWEED, and the hydraulic damping coefficients were obtained from the flow meter and pressure sensor installed in PTO-1.

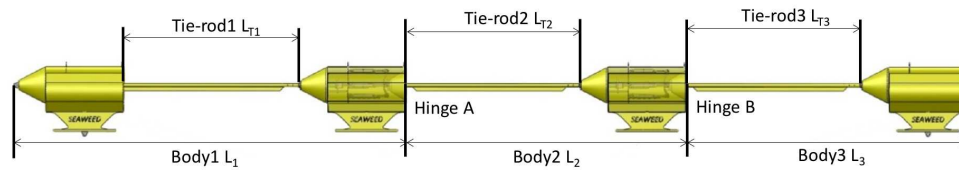


Figure 2.5: Body and Tie-rod Length Definition

In the model tests, regular wave periods were 6 s, 8 s, 10 s, and 12 s (full scale).

## 2.3 Model Tests on the Second Generation of SeaWEED

The experimental and numerical studies of the first generation model led to the second generation with improvements in the hull geometry, a lower draft and a different connection structure, which is shown in Fig. 2.7. Model tests on the second generation of SeaWEED were conducted at the towing tank of Memorial University (MUN). The towing tank is 58.0 m in length, 4.6 m in width, and 1.8m in depth, as shown in Fig. 2.6. Fig. 2.7 presents the SeaWEED model in the towing tank. The 1:16 model tests for the first generation of SeaWEED was done by Grey Island Energy Inc in a large wave tank, and for the second generation of SeaWEED, the model test scale, 1 : 35, was then determined according to the dimension of the towing tank at MUN. The principle dimensions of SeaWEED and the 1 : 35 model are listed in Table 2.2.



Figure 2.6: Towing Tank of MUN

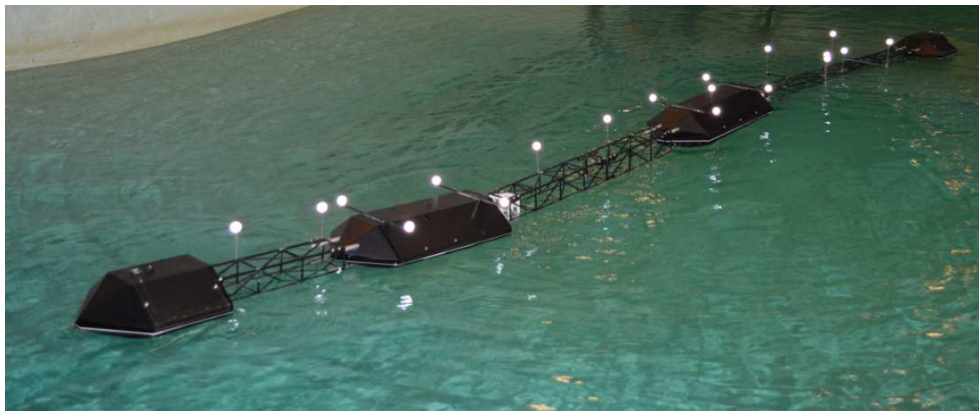


Figure 2.7: SeaWEED Model in the Towing Tank

Table 2.2: Particulars of SeaWEED (second generation)

Parameter	Full Scale	1:35 Scale
Length of Nose Module, $L_n(m)$	9.000	0.257
Length of Tail Module, $L_t(m)$	9.000	0.257
Length of Producing Module, $L_p(m)$	16.000	0.457
Width, $B(m)$	8.000	0.229
Height, $H(m)$	5.000	0.143
Draft, $T(m)$ ,	2.50	0.0714

### 2.3.1 Test Matrix

In the model tests, the wave periods were varied from 5.5 s to 10.0 s (full scale), and the wave steepness was set as 1/50. The definition of the body length is shown in Fig. 2.8. The combinations of truss lengths are presented Table 2.3, and the draft was 2.5 m in full scale. The test matrix is presented in Table 2.4. The corresponding PTO damping settings are given in Table 2.5. Several repeated tests were carried out at a few wave frequencies around the region with maximum responses. Good repeatability was achieved in tests.

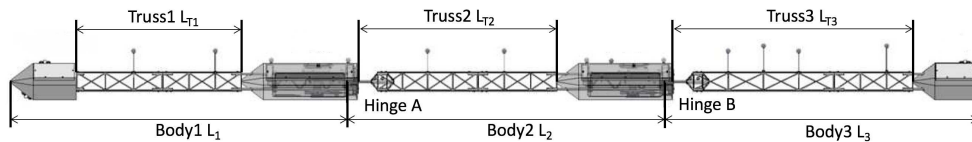


Figure 2.8: Body and Truss Length Definition

Table 2.3: Truss length combinations

Case	Full Scale				1:35 Scale			
	$L_1(m)$	$L_2(m)$	$L_3(m)$	$L_{total}(m)$	$L_1(m)$	$L_2(m)$	$L_3(m)$	$L_{total}(m)$
<i>T1</i>	46.912	43.912	43.912	134.736	1.340	1.255	1.255	3.850
<i>T2</i>	41.252	43.912	49.962	135.126	1.179	1.255	1.427	3.861
<i>T3</i>	41.252	43.912	56.402	141.566	1.179	1.255	1.611	4.045
<i>T4</i>	41.252	43.912	63.233	148.397	1.179	1.255	1.807	4.240

Table 2.5: Damping cases

Case No.	Spring Compression (mm)	
	PTO-1	PTO-2
D0	-	-
D1	3.0	2.3
D2	4.3	4.0
D3	4.3	-
D4	-	4.0
D5	6.0	5.0

Table 2.4: Test matrix

No.	$T(s)$		No. of Conducted Tests								
	Full	Model	$T1$	$T2$	$T3$	$T4$	$T1$	$T1$	$T1$	$T1$	$T1$
	Scale	Scale	$D0$	$D0$	$D0$	$D0$	$D1$	$D2$	$D3$	$D4$	$D5$
1	5.50	0.93	1	1	1	1	0	0	0	0	0
2	6.00	1.01	1	1	1	3	0	0	0	0	0
3	6.50	1.10	1	1	1	3	0	0	0	0	0
4	7.00	1.18	3	1	3	1	0	0	0	0	0
5	7.50	1.27	3	3	3	3	3	3	3	3	3
6	8.00	1.35	3	3	3	3	2	3	1	2	3
7	8.50	1.44	3	3	3	1	1	1	3	3	1
8	9.00	1.52	3	1	1	3	1	1	3	3	1
9	10.00	1.69	1	3	1	1	1	1	1	1	1

$T1 - T4$ : Body length combinations;  $D0 - D5$ : PTO Damping cases

### 2.3.2 Test Set-up

The test set-up is given in Fig. 2.9. The model was constrained by four soft mooring lines from drift motions. Four AWP-24 resistive wave probes were used to measure the wave elevations. Motions of the model were measured by a Qualisys motion capture system. Fig. 2.7 shows the scaled model with tracking markers distributed on its floats and trusses.

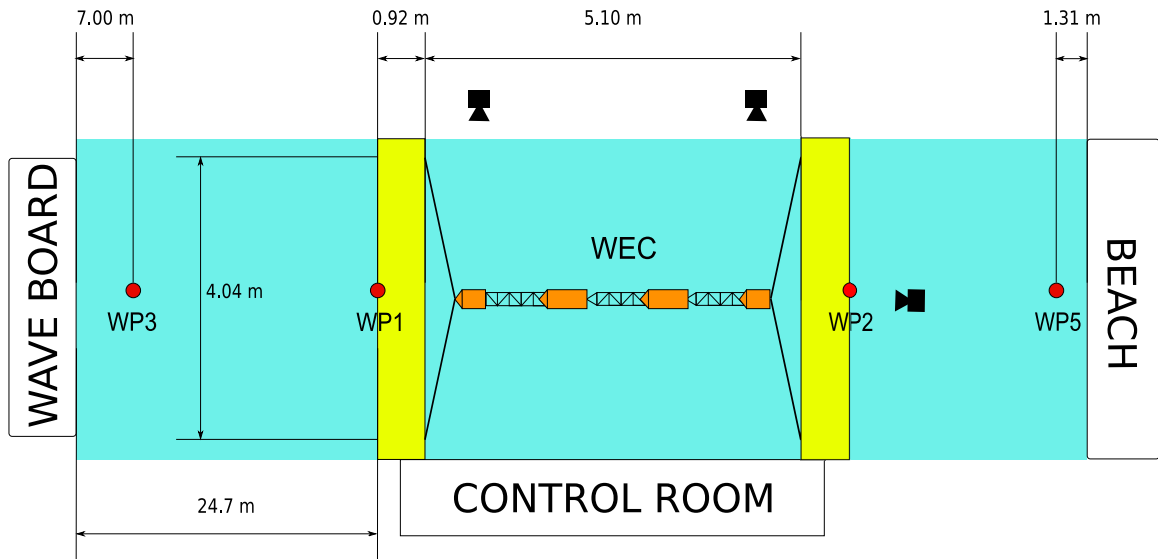


Figure 2.9: Test Set-up

The PTO systems were mimicked by friction dampers. As shown in Fig. 2.10, the angular hinge motions of the model were transferred to the linear motion of the sliding bar of the damper by the swash plate. Honeywell Model 31 load cells and the Contelec linear position sensors were used to measure the friction forces and the sliding motions, respectively.

As shown in Fig. 2.11, the damper is consisted of a steel frame, an aluminum

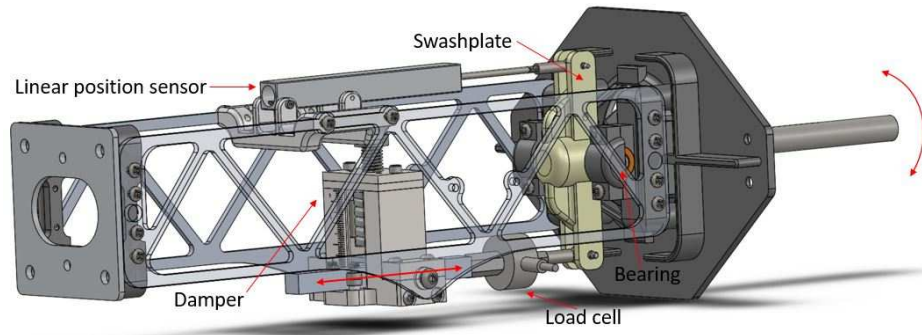


Figure 2.10: Friction Damper

sliding bar, a spring, and two Teflon bars. The aluminum bar is guided by four low-friction bearings. The upper Teflon bar is pressed by the spring, which can be adjusted using the screw on top of the frame to change the friction forces. To quantify the adjustments, marks were also machined to indicate the spring displacement. It is noted that friction dampers with aluminum-leather and aluminum-steel contacts were also tested. However, the former suffered from inconsistent frictions due to the change of humidity, and the latter failed to provide smooth frictions since the contact surfaces were not perfectly even. The damper with the Teflon-aluminum contact showed good repeatability. Two identical dampers were manufactured to mimic the two PTO systems.

### 2.3.3 Pre-tests

Before the model tests, the instruments including wave probes, load cells and displacement sensors were calibrated. The Qualisys system was calibrated according to the calibration quality indicator in the Qualisys Track Manager software. For each damping set-up, the friction dampers were calibrated before being installed on the

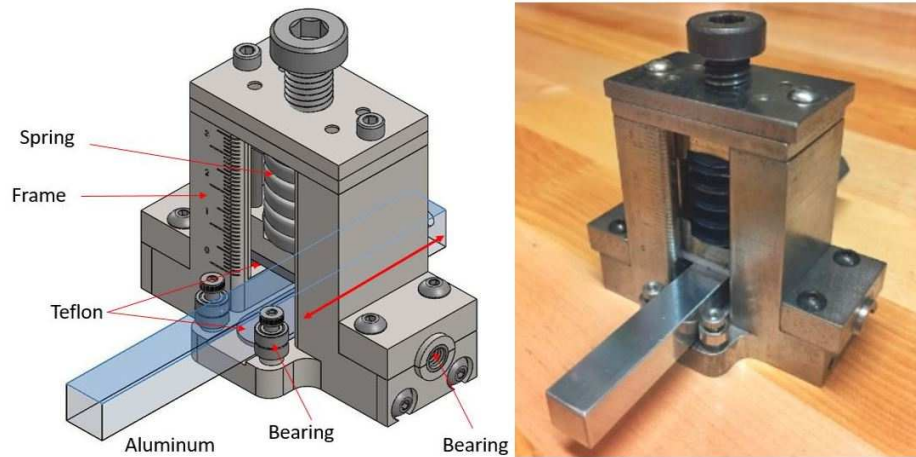


Figure 2.11: Friction Damper

model.

### 2.3.3.1 Wave Probe Calibration

Static calibrations were performed on the AWP-24 wave probes. The voltages were measured when the wave probes were submerged in five different depths, as shown in Fig. 2.12. For each wave probe, the calibration was repeated for three times. An example of the calibration results for WP3 is presented in Fig. 2.13.

### 2.3.3.2 Load Cell Calibration

Two Honeywell Model-31 load cells (see Fig. 2.14) were used to measure the forces in the PTO system. Three static calibrations were repeated for each load cell. In each calibration, six load steps were used in compressing and expansion directions, and each step was kept stable for 30 seconds. The calibration results for the load cell in PTO-2 are presented in Fig. 2.15.



Figure 2.12: Wave Probe Calibration

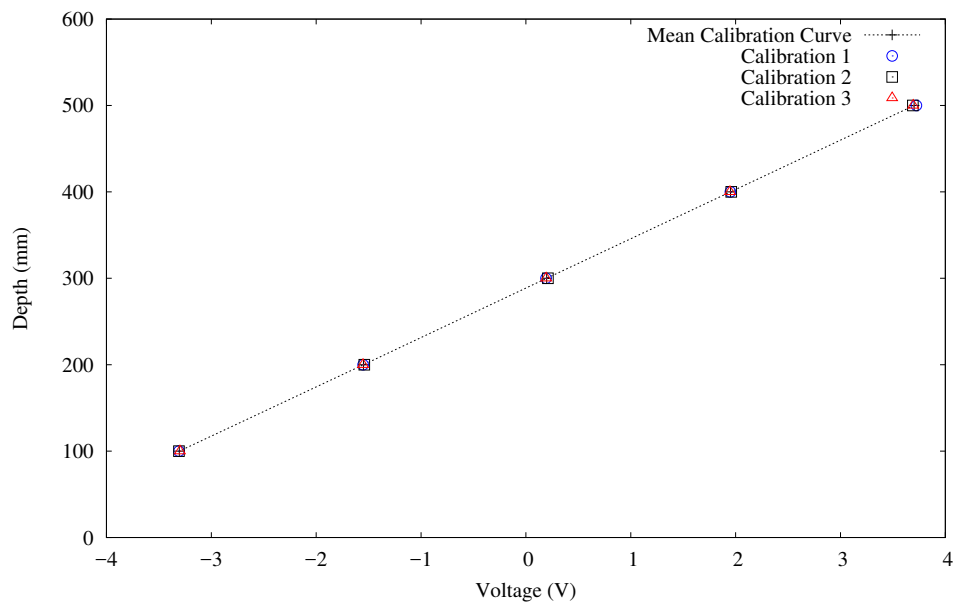


Figure 2.13: Wave Probe Calibration Results (WP3)



Figure 2.14: Honeywell Model-31 Load Cell

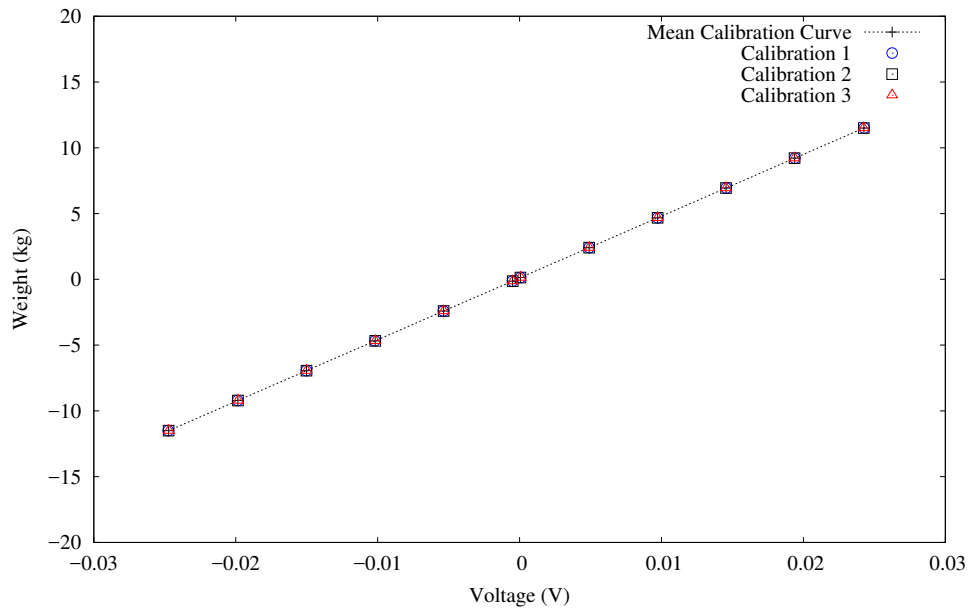


Figure 2.15: Load Cell Calibration Results (PTO-2)

### 2.3.3.3 Displacement Sensor Calibration

Two Contelec linear position sensors with ranges of 50 mm and 75 mm were used to measure the damper sliding bar movements. The sensors were calibrated by recording the output voltage when different displacements were applied. Each displacement sensor was calibrated for three time. Fig. 2.16 shows the calibration results of the displacement sensor in PTO-2.

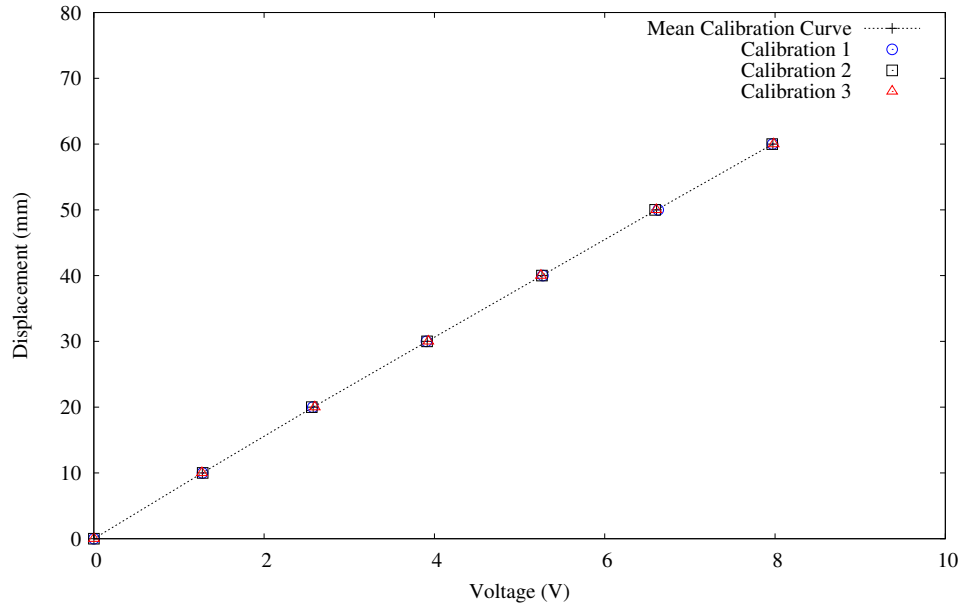


Figure 2.16: Displacement Sensor Calibration Results (PTO-2)

### 2.3.3.4 Damper Calibration

As shown in Fig. 2.17, a calibration frame was designed and built to calibrate the dampers before the model tests. The motor was turned to a fixed revolving speed by a controller. The speed was recorded by an RPM sensor. A 1:20 gearbox converted

the speed to the disk system speed, and a slider-crank mechanism transformed the rotational motion to the translational motion of the sliding bar. The amplitude of the bar movement was controlled by changing the rotating diameter of the stick connecting to the disk. The displacements and the friction forces were measured by a displacement sensor paralleled to the bar and a load cell on the bar.

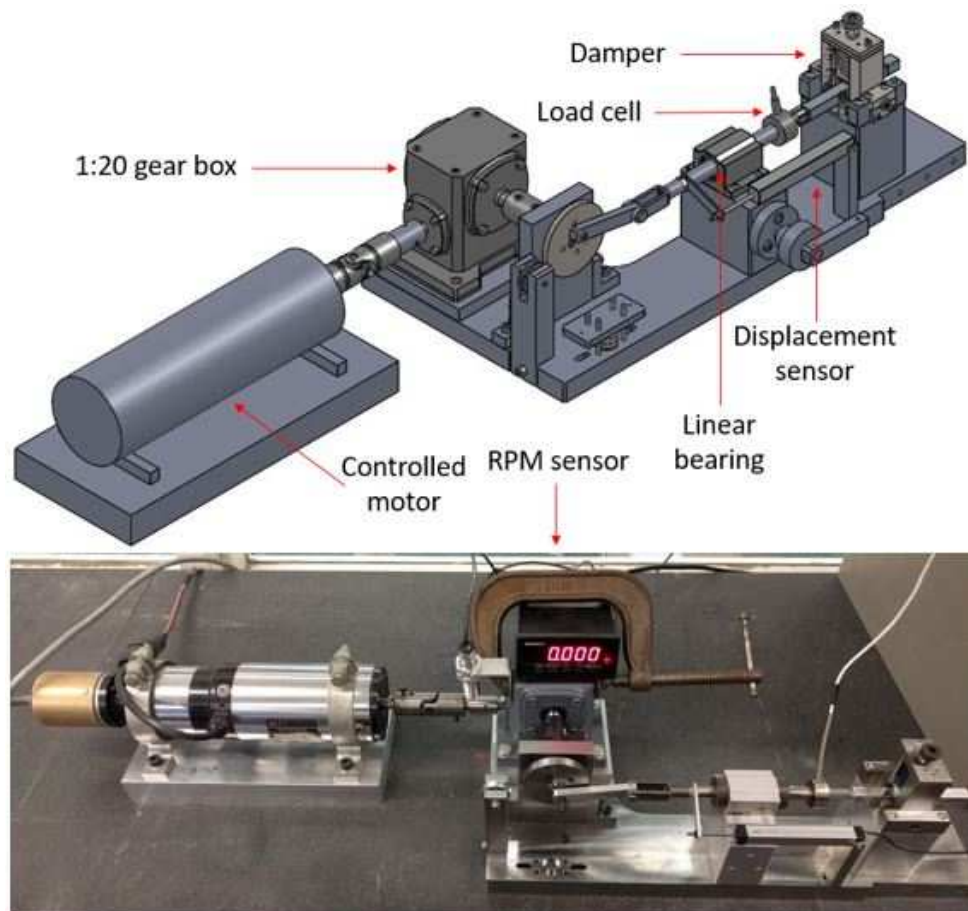


Figure 2.17: Damper Calibration Apparatus

Three damper set-ups were conducted, and the springs of two dampers were adjusted to a certain compression to achieve the target damping forces. The damping

coefficients from the calibration and the tests of two damping systems are presented with respect to the velocity amplitude of the sliding motion in Fig. 2.18, Fig. 2.19, and Fig. 2.20.

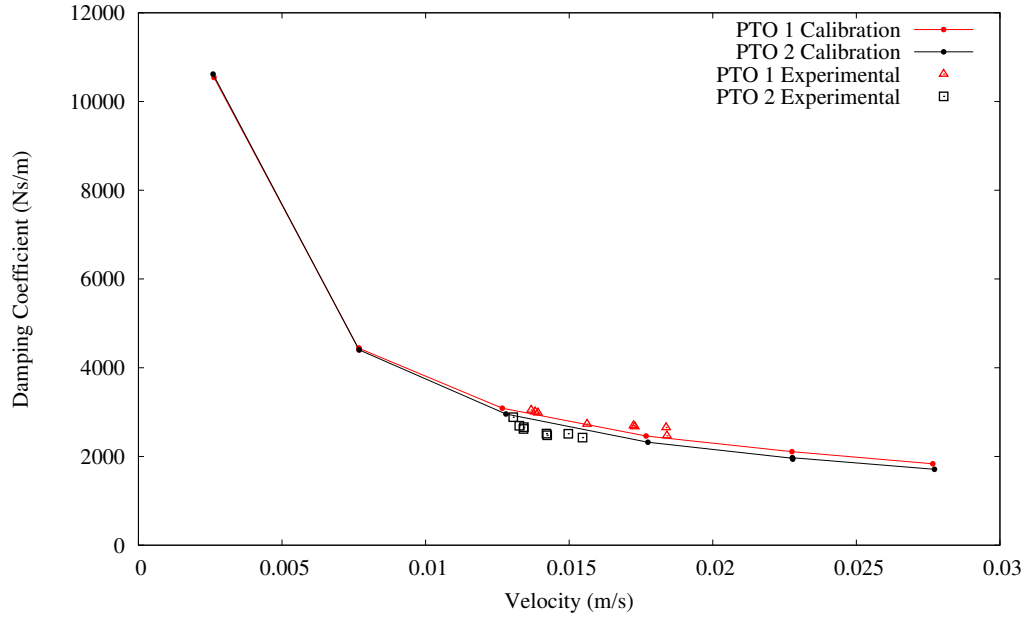


Figure 2.18: Damper Calibration Results (D1)

### 2.3.3.5 Synchronization of Measurements

During tests, the measurements of wave amplitudes and friction forces and displacements of the dampers are recorded by the LabView system, and the motions of SeaWEED are measured by the Qualisys system. These measurements need to be synchronized. An electrical synchronization signal was generated and recorded in the data collection by the two systems, i.e., the LabView system and the Qualisys system.

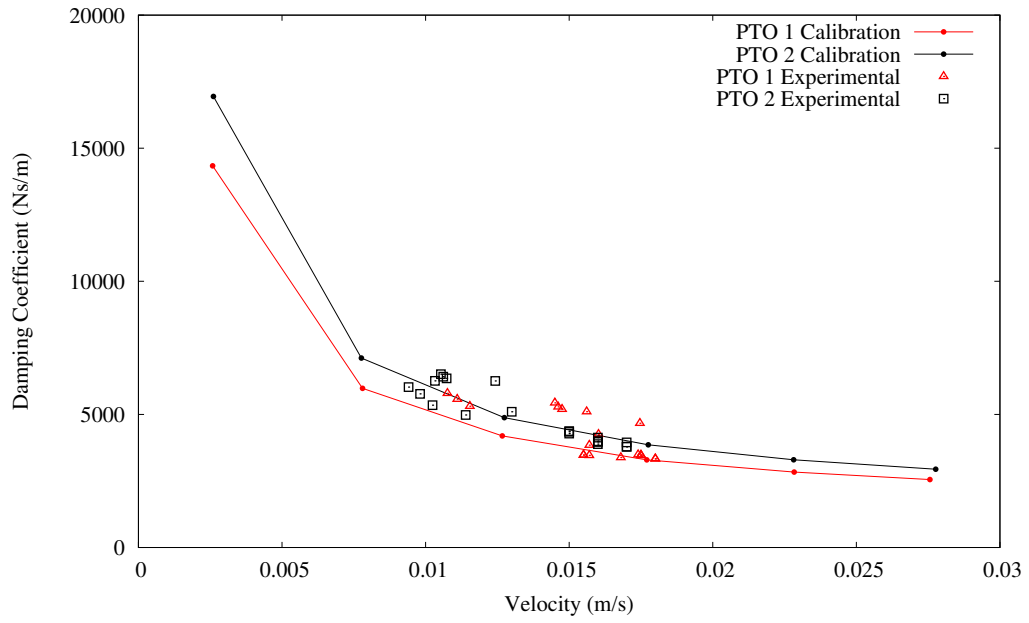


Figure 2.19: Damper Calibration Results (D2, D3 and D4)

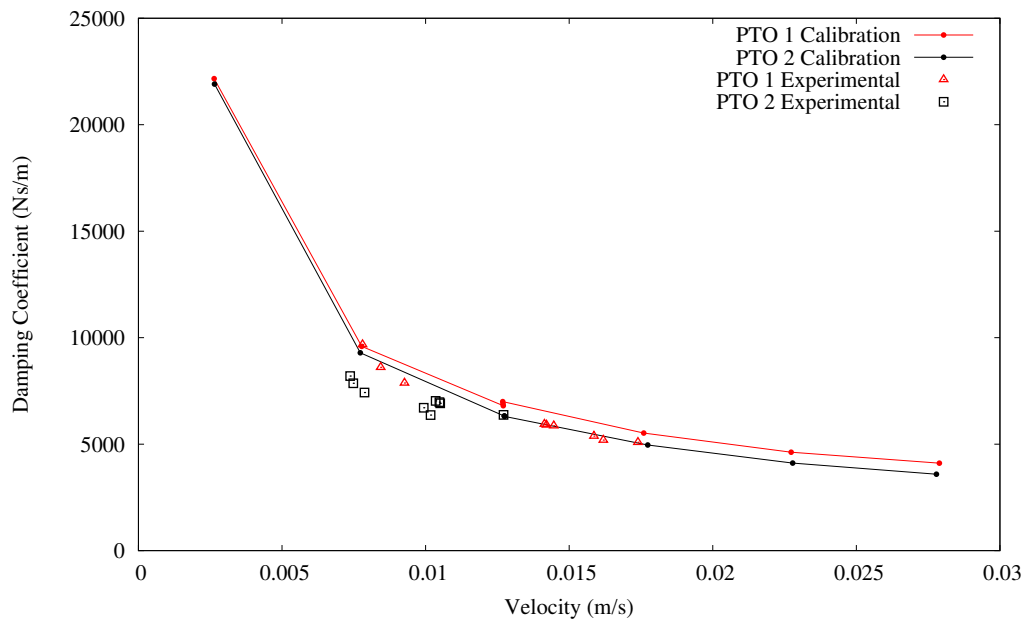


Figure 2.20: Damper Calibration Results (D5)

The Qualisys system can receive a square wave voltage signal as a trigger via the Oqus sync unit of the Qualisys system. The triggering signal was generated by the National Instruments NI-9264 module installed on the data acquisition system. The motion measurements were then recorded by the Qualisys system after a preset delay (20 ms in the present tests). In the present model tests, a square wave signal with an amplitude of 5 V and a duration of 50 ms was generated as shown in Fig. 2.21. Based on the triggering signal, the delay between the two measurement systems can be precisely determined, and a re-alignment can be performed on all the measurements.

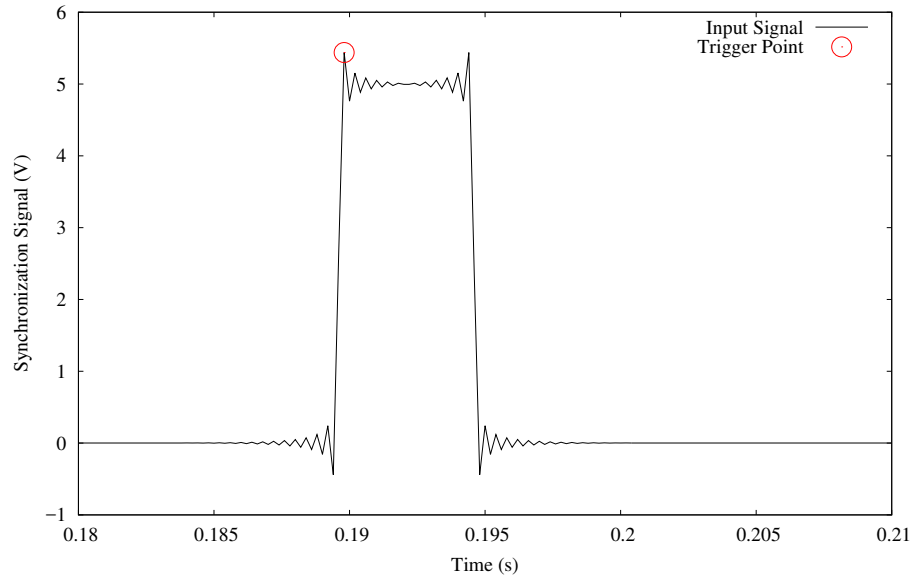


Figure 2.21: Synchronization Input by Module NI9264

### 2.3.4 Experimental Data-processing

As shown Fig. 2.22, the experimental relative pitch angles,  $\theta_1$  and  $\theta_2$ , at the joints of two PTO systems, *PTO* – 1 and *PTO* – 2, were captured and measured

by a Qualisys motion capture system. FFT analysis was conducted to obtain the amplitudes of angular motions.

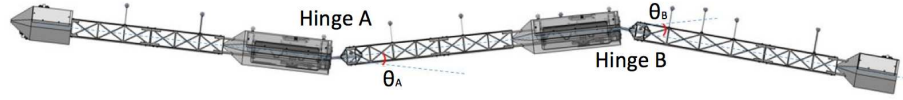


Figure 2.22: Relative Pitch Angles

When the PTO systems were activated, the damping forces and the displacements of the sliding bars were measured. The velocities of the bars were obtained from time series of their displacements. The moving average method was applied to remove unrealistic oscillations in the time series of force and velocity. Fig. 2.23 presents a segment of time series of force and velocity for PTO-1. The corresponding wave period was 1.35 s in model scale.

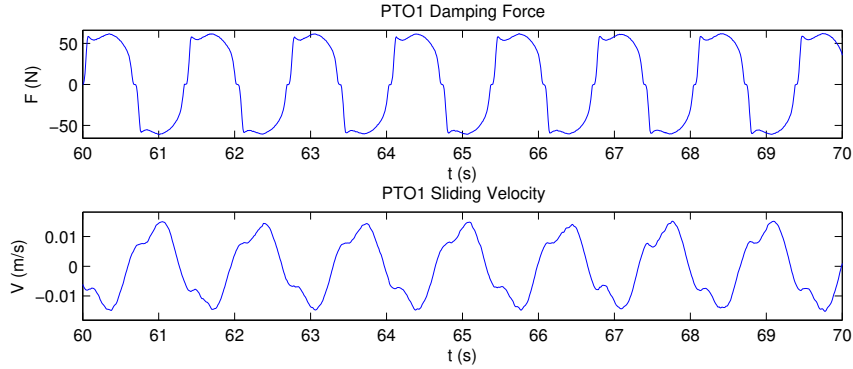


Figure 2.23: Damping Force and Sliding Velocity

The average power absorption of the  $i$ th PTO, denoted as  $P_i$ , is

$$P_i = \frac{\int_0^T F_i(t)v_i(t)dt}{T} \quad (2.1)$$

where  $F_i(t)$  is the damping force,  $v_i(t)$  is the sliding velocity, and  $T$  is the time length.

Then the equivalent damping coefficient,  $d_i$ , was obtained as

$$d_i = \frac{\int_0^T F_i(t)v_i(t)dt}{\int_0^T v_i^2(t)dt} \quad (2.2)$$

Introducing the total power of the incident wave per unit crest length across the device,

$$E = \frac{\rho g^2 A^2}{4\omega} \quad (2.3)$$

the power capture width for the SeaWEED is given as

$$C_{width} = \frac{\sum_{i=1}^2 P_i}{E} \quad (2.4)$$

where  $A$  is the wave amplitude and  $\omega$  is the wave frequency.

In order to map the model test results to the full scale device, the similitude theory is applied. Two main similarity parameters are involved, namely, the Strouhal number,  $S = \frac{L}{UT}$ , and the Froude number,  $Fr = \frac{U}{\sqrt{gL}}$ , where  $L$  is the length of the device,  $U$  is the wave speed,  $T$  is the wave period and  $g$  is the gravitational acceleration. Denote a quantity of interest, such as relative pitch angle, damping coefficient and capture width, as  $Q$ , the relationship between the model scale value and the full scale one can be expressed by  $Q_{full} = Q_{model} * \lambda^n$ , where  $\lambda$  is the scale and  $n$  is the scaling factor derived based on the similarity parameters. The scaling of the quantities involved in the present study are listed in Table 2.6.

Table 2.6: Scaling of quantities

Quantity, $Q$	Unit	Scaling factor, $n$
Device dimensions (length, breadth and draft), $L$ , $B$ and $T$	( $m$ )	1.0
Wave period, $T$	( $s$ )	0.5
Damping coefficient, $d$	( $Nms$ )	4.5
Velocity, $U$	( $m/s$ )	0.5
Relative pitch angle, $\theta$	–	0.0
Capture width, $C_w$	( $m$ )	1.0
Absorbed power, $P_s$	( $kW$ )	3.5

# Chapter 3

## Time-domain Simulation of SeaWEED

The three bodies of SeaWEED articulated by hinge joints are subjected to constrained motions. To simulate the dynamics of SeaWEED, a potential-flow based time-domain program is developed. This chapter presents the mathematical formulations of the time-domain method where the constraints are modeled using the Lagrange multiplier approach (Baraff,1996), the Froude-Krylov forces are calculated over the instantaneous wetted surfaces of the bodies and the wave pressure on the body surfaces is computed applying the Wheeler Stretching method (Wheeler et al., 1969). The numerical method is validated using the model test data, and good agreement is achieved.

## 3.1 Mathematical Formulation

### 3.1.1 Coordinate System Definition

As shown in Fig. 3.1, an earth-fixed Cartesian coordinate system,  $OXYZ$ , is employed with the  $OXY$  plane coinciding with the undisturbed free surface and the  $OZ$  axis pointing vertically upward. In three body-fixed coordinate systems,  $o_i x_i y_i z_i$ ,  $i = 1, 2, 3$ ,  $o_i$  is at the point of intersection of calm water surface, the longitudinal plane of symmetry, and the vertical plane passing through the centre of gravity (CG) of the  $i^{th}$  body; the  $o_i z_i$  axis points upward; the  $o_i x_i y_i$  plane coincides with the undisturbed free surface when the body is at rest; and the  $o_i x_i$  axis points from the tail module to the nose module.

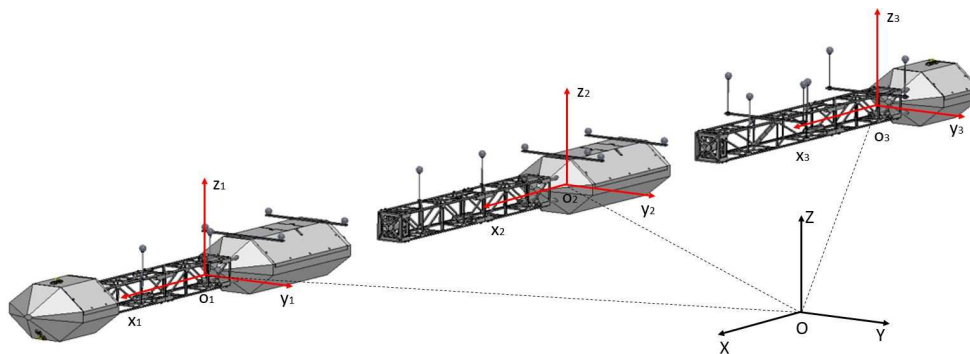


Figure 3.1: Coordinate Systems

### 3.1.2 Equations of Motion

According to the work of Danmeier (1999) and Qiu and Peng (2013), equations of motion for the SeaWEED system can be developed as follows.

Denoting a column vector by braces  $\{\}$ , translational displacements of the  $i$ th body in the  $OXYZ$  system are represented by  $\mathbf{X}_i = \{X_{i,1}, X_{i,2}, X_{i,3}\}$  and the Eulerian angles are given by  $\mathbf{X}_{R_i} = \{X_{i,4}, X_{i,5}, X_{i,6}\}$ . The angular velocity in  $o_i x_i y_i z_i$  is denoted by  $\boldsymbol{\omega}_i$ . The time rate change of the Eulerian angles is related to the angular velocity by

$$\dot{\mathbf{X}}_{R_i} = \mathbf{T}_i \boldsymbol{\omega}_i = \begin{bmatrix} 1 & s_1 t_2 & c_1 t_2 \\ 0 & c_1 & -s_1 \\ 0 & s_1/c_2 & c_1/c_2 \end{bmatrix} \boldsymbol{\omega}_i \quad (3.1)$$

where  $c_k = \cos(X_{i,3+k})$ ,  $s_k = \sin(X_{i,3+k})$  and  $t_k = \tan(X_{i,3+k})$  for  $k=1,2$  and  $3$ .

Equations of motion for the  $i$ th body are then given as

$$\begin{bmatrix} \mathbf{m}_i & -m_i \mathbf{x}_{cgi} \mathbf{D}_i^T \\ m_i \mathbf{x}_{cgi} \mathbf{D}_i & \mathbf{I}_{oi} \end{bmatrix} \begin{Bmatrix} \ddot{\mathbf{X}}_i \\ \dot{\boldsymbol{\omega}}_i \end{Bmatrix} = \begin{Bmatrix} \mathbf{F}_i \\ \mathbf{M}_{oi} \end{Bmatrix} \quad (3.2)$$

where  $\mathbf{m}_i$  is the  $3 \times 3$  matrix with the body mass,  $m_i$ , along its diagonal and zero everywhere else,  $\mathbf{I}_{oi}$  is the mass moment of inertia matrix with respect to the origin of the  $i$ th body,  $\mathbf{x}_{cgi}$  is the centre of gravity of  $i$ th body,  $\mathbf{F}_i$  are the external forces acting on the body in  $OXYZ$ ,  $\mathbf{M}_{oi}$  are the moment about the origin of the body-fixed coordinate system, and  $\mathbf{D}_i$  is the rotational transformation matrix between the earth-fixed and body-fixed coordinate systems as follows:

$$\mathbf{D}_i = \begin{bmatrix} c_2 c_3 & c_2 s_3 & -s_2 \\ s_1 s_2 c_3 - c_1 s_3 & s_1 s_2 s_3 + c_1 c_3 & s_1 c_2 \\ c_1 s_2 c_3 + s_1 s_3 & c_1 s_2 s_3 - s_1 c_3 & c_1 c_2 \end{bmatrix} \quad (3.3)$$

Equation 3.2 can also be written in a concise form as below:

$$\mathbf{M}_i \dot{\mathbf{v}}_i = \mathbf{F}_i^E \quad (3.4)$$

where  $\mathbf{F}_i^E$  is the vector including resultant forces and moments on the  $i$ th body, and

$$\mathbf{v}_i = \{\dot{X}_{i1}, \dot{X}_{i2}, \dot{X}_{i3}, \omega_{i1}, \omega_{i2}, \omega_{i3}\}, \quad i = 1, 2, 3 \quad (3.5)$$

The total force acting on the  $i$ th body can be written as

$$\mathbf{F}_i^E = \mathbf{F}_i^{FK} + \mathbf{F}_i^{RS} + \mathbf{F}_i^R + \mathbf{F}_i^D + \mathbf{F}_i^{PTO} + \mathbf{F}_i^C \quad (3.6)$$

where  $\mathbf{F}_i^{FK}$  are the Froude-Krylov forces;  $\mathbf{F}_i^{RS}$  are the restoring forces;  $\mathbf{F}_i^R$  and  $\mathbf{F}_i^D$  are the forces due to radiated and diffracted waves, respectively;  $\mathbf{F}_i^{PTO}$  are the damping forces from the PTO system; and  $\mathbf{F}_i^C$  are the constraint forces due to hinge joints.

The nonlinear Froude-Krylov forces are calculated according to instantaneous wetted surface applying the Wheeler Stretching Approach (Wheeler et al., 1969). The linear diffraction forces are obtained from the frequency domain solution using WAMIT. The linear radiation forces on the  $i$ th body are calculated using the impulse function method and the added mass and damping matrices from WAMIT, i.e.,

$$\mathbf{F}_i^R = -\mathbf{A}(\infty)_{ij} \ddot{\mathbf{x}}_j(t) - \int_{-\infty}^t \mathbf{K}_{ij}(t - \tau) \dot{\mathbf{x}}_j(\tau) dt \quad (3.7)$$

where  $\mathbf{A}(\infty)_{ij}$  is the added mass matrix ( $6 \times 6$ ) at the infinite frequency of the  $i$ th body due to the  $j$ th body,  $i = 1, 2, 3$  and  $j = 1, 2, 3$  for SeaWEED,  $\dot{\mathbf{x}}_j(\tau)$  and  $\ddot{\mathbf{x}}_j(t)$  are the velocities and accelerations of the  $j$ th body, respectively,  $\mathbf{K}_{ij}(t - \tau)$  is the impulse function of the  $i$ th body due to the  $j$ th body, which is also a  $6 \times 6$  matrix. The response function can be obtained from the damping matrix,  $\mathbf{B}_{ij}(\omega)$ , which is a function of wave frequency  $\omega$  and was calculated from WAMIT in this work, i.e.,

$$\mathbf{K}_{ij}(\tau) = \frac{2}{\pi} \int_0^\infty \mathbf{B}_{ij}(\omega) \cos \omega \tau d\omega \quad (3.8)$$

Denoting the damping coefficients of PTO-1 and PTO-2 as  $d_1$  and  $d_1$ , respectively, the damping moments can be computed as

$$\begin{aligned} M_1^{PTO1} &= -d_1\dot{\theta}_1, & M_2^{PTO1} &= d_1\dot{\theta}_1 \\ M_2^{PTO2} &= -d_2\dot{\theta}_2, & M_3^{PTO2} &= d_2\dot{\theta}_2 \end{aligned} \quad (3.9)$$

where  $M_i^{PTOk}$  is the moment acting on the  $i$ th body due to PTO- $k$ , and  $\dot{\theta}_1 = \dot{\beta}_1 - \dot{\beta}_2$  and  $\dot{\theta}_2 = \dot{\beta}_2 - \dot{\beta}_3$  are the relative pitch velocities of PTO-1 and PTO-2, respectively, as depicted in Fig. 3.2.

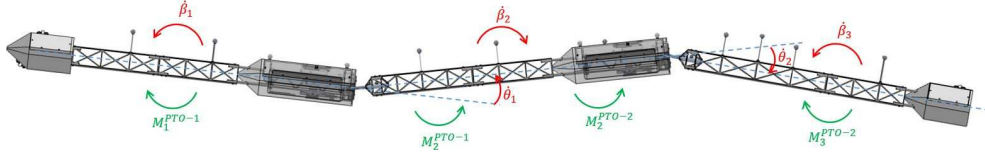


Figure 3.2: Damping Moments

### 3.1.3 Computation of Constraint Forces

The computation of the constraint forces,  $\mathbf{F}^C$ , is discussed in this sub-section. SeaWEED has two hinge connectors,  $A$  and  $B$ , for the 1st and 2nd bodies and for the 2nd and 3rd bodies, respectively, as shown in Fig. 3.2. Denoting the position of hinge  $A$  on Body 1 as  $\mathbf{H}_{A1}$  and on Body 2 as  $\mathbf{H}_{A2}$  in  $OXYZ$ , the following constraint condition should be satisfied,

$$\mathbf{H}_{A1} = \mathbf{H}_{A2} \quad (3.10)$$

The same condition can be applied to the hinge point,  $B$ . Introducing the relative

position vector,  $\mathbf{C}$ , the constraint conditions can be rewritten as

$$\mathbf{C} = \begin{bmatrix} \mathbf{H}_{A1} - \mathbf{H}_{A2} \\ \mathbf{H}_{B2} - \mathbf{H}_{B3} \end{bmatrix} = \mathbf{0} \quad (3.11)$$

The time derivatives of the constraint conditions,  $\dot{\mathbf{C}} = 0$ , i.e., the conditions for relative velocities, are given as

$$\dot{\mathbf{C}} = \begin{bmatrix} \dot{\mathbf{H}}_{A1} - \dot{\mathbf{H}}_{A2} \\ \dot{\mathbf{H}}_{B2} - \dot{\mathbf{H}}_{B3} \end{bmatrix} = \mathbf{0} \quad (3.12)$$

where  $\dot{\mathbf{H}}_{Ai} = \dot{\mathbf{X}}_i + \boldsymbol{\omega}_i \times \mathbf{r}_{Ai}$ ,  $i = 1, 2$ , and  $\dot{\mathbf{H}}_{Bi} = \dot{\mathbf{X}}_i + \boldsymbol{\omega}_i \times \mathbf{r}_{Bi}$ ,  $i = 2, 3$  are the position vectors of the hinge points, A and B, respectively, in the body-fixed coordinate systems,  $o_i x_i y_i z_i$ , with respect to the center of gravity of each body.

Equation 3.12 can also be rewritten as

$$\mathbf{J}\mathbf{V} = \mathbf{0} \quad (3.13)$$

where  $\mathbf{J}$  is the Jacobian matrix ( $6 \times 18$ ),

$$\mathbf{V} = \{\mathbf{v}_1, \mathbf{v}_2, \mathbf{v}_3\}^T \quad (3.14)$$

Furthermore, the acceleration constraint are given as

$$\ddot{\mathbf{C}} = \begin{bmatrix} \ddot{\mathbf{H}}_{A1} - \ddot{\mathbf{H}}_{A2} \\ \ddot{\mathbf{H}}_{B2} - \ddot{\mathbf{H}}_{B3} \end{bmatrix} = \mathbf{0} \quad (3.15)$$

where  $\ddot{\mathbf{H}}_{Ai} = \ddot{\mathbf{X}}_i + \dot{\boldsymbol{\omega}}_i \times \mathbf{r}_{Ai} + \boldsymbol{\omega}_i \times (\boldsymbol{\omega}_i \times \mathbf{r}_{Ai})$ ,  $i = 1, 2$ , and  $\ddot{\mathbf{H}}_{Bi} = \ddot{\mathbf{X}}_i + \dot{\boldsymbol{\omega}}_i \times \mathbf{r}_{Bi} + \boldsymbol{\omega}_i \times (\boldsymbol{\omega}_i \times \mathbf{r}_{Bi})$ ,  $i = 2, 3$ , and  $\ddot{\mathbf{X}}_i$  and  $\dot{\boldsymbol{\omega}}_i$  are the translational and angular accelerations of the  $i$ th body, respectively.

Equation 3.15 can be rewritten as

$$J\dot{V} + \mathbf{k} = \mathbf{0} \quad (3.16)$$

where  $\mathbf{k}$  is given as

$$\mathbf{k} = \begin{bmatrix} \boldsymbol{\omega}_1 \times (\boldsymbol{\omega}_1 \times \mathbf{r}_{A1}) - \boldsymbol{\omega}_2 \times (\boldsymbol{\omega}_2 \times \mathbf{r}_{A2}) \\ \boldsymbol{\omega}_2 \times (\boldsymbol{\omega}_2 \times \mathbf{r}_{B2}) - \boldsymbol{\omega}_3 \times (\boldsymbol{\omega}_3 \times \mathbf{r}_{B3}) \end{bmatrix} \quad (3.17)$$

Since the constraint forces are internal forces and do not change the energy of the system (Witkin, 1997), it implies the constraint forces can be expressed as

$$\mathbf{F}^C = \mathbf{J}^T \boldsymbol{\lambda} \quad (3.18)$$

where  $\boldsymbol{\lambda}$  is the Lagrange multiplier.

Combining Eqs. 3.2, 3.16 and 3.18, a system of equations can be obtained as

$$\begin{bmatrix} \mathbf{M} & -\mathbf{J}^T \\ \mathbf{J} & \mathbf{0} \end{bmatrix} \begin{bmatrix} \dot{V} \\ \boldsymbol{\lambda} \end{bmatrix} = \begin{bmatrix} \mathbf{F}^{E-C} \\ -\mathbf{k} \end{bmatrix} \quad (3.19)$$

where  $\mathbf{M}$  is a  $18 \times 18$  matrix consisting of mass matrices of three bodies, as defined in Eq. 3.4, i.e.,

$$\mathbf{M} = \begin{bmatrix} \mathbf{M}_1 & & \\ & \mathbf{M}_2 & \\ & & \mathbf{M}_3 \end{bmatrix} \quad (3.20)$$

and  $\mathbf{F}^{E-C}$  is the external force acted on the three bodies excluding the constraint forces.

Accelerations and the Lagrange multipliers (hence the constraint forces) can be solved by solving Eq. 3.19.

### 3.1.4 Computation of Nonlinear Froude-Krylov Forces

To better resolve the nonlinearities associated with the changing underwater hull shape, the instantaneous wetted surfaces under the wave profile are considered, as shown in Fig. 3.3, and the pressure on the body surfaces is computed applying the Wheeler Stretching Approach (Wheeler et al., 1969).

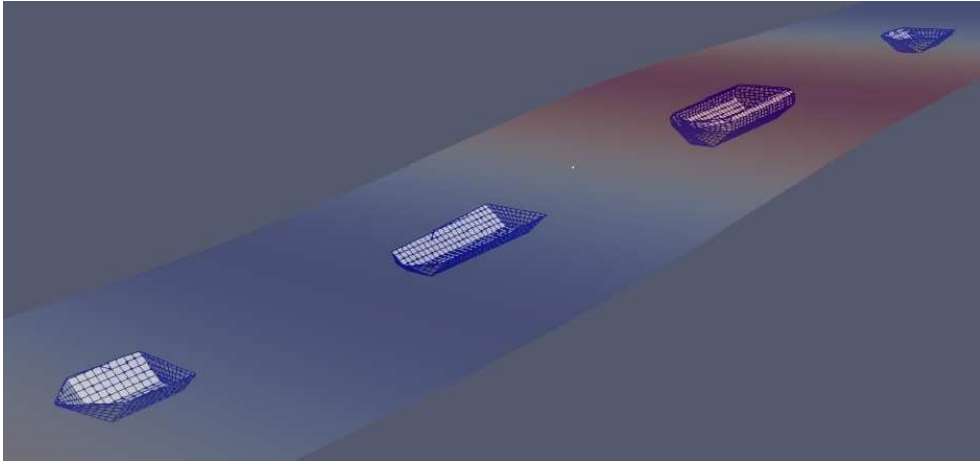


Figure 3.3: SeaWEED Wetted Surfaces under Waves

Under linear wave theory, the wave potential can be written as

$$\phi_0(x, y, z, t) = \frac{ig\eta_0}{\omega_0} \frac{\cosh[k(z+h)]}{\cosh kh} e^{i\omega t - ik(x \cos \beta + y \sin \beta)} \quad (3.21)$$

where  $\eta_0$  is wave amplitude,  $\omega_0$  is wave frequency,  $h$  is water depth,  $\beta$  is wave heading direction (180 degrees for head waves) and  $g$  is the gravity acceleration.

For infinite water depth, Eq. 3.21 becomes

$$\phi_0(x, y, z, t) = \frac{ig\eta_0}{\omega_0} e^{kz} e^{i\omega t - ik(x \cos \beta + y \sin \beta)} \quad (3.22)$$

The wave elevation can be expressed using the wave potential

$$\eta(t) = -\frac{1}{g} \frac{\partial \phi_0}{\partial t} \quad (z = 0) \quad (3.23)$$

As the wave potential is defined under the undisturbed free surface, the Wheeler stretching method, proposed by Wheeler (1969), is used to compute the pressure on the instantaneous wetted surfaces. In the stretching method, the wave velocity distribution from sea bed to the mean water level,  $\eta = 0$ , is stretched to the instantaneous wave surface,  $\eta(t)$ . As shown in Fig. 3.4, the red dashed lines represent the incident wave velocity profile under the undisturbed free surface, and the red solid lines represent the stretched velocity profile applying the Wheeler stretching method.

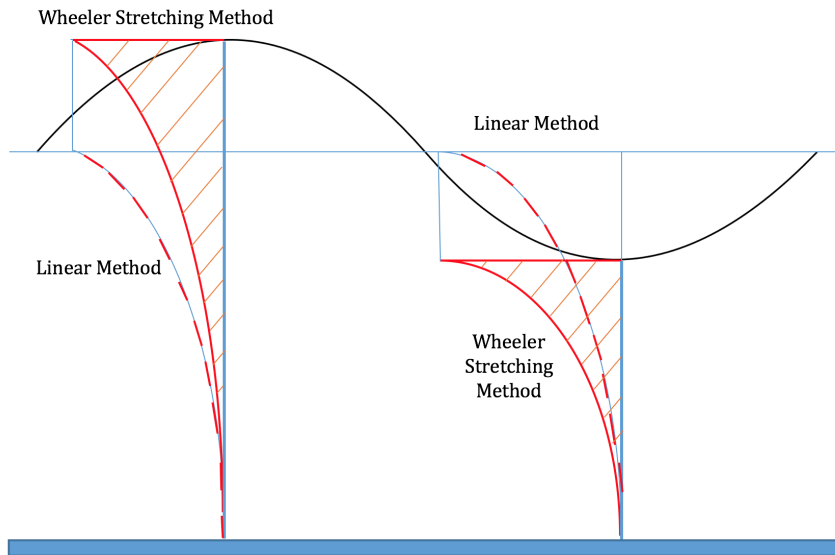


Figure 3.4: Illustration of Wheeler Stretching Theory

The incident wave pressure,  $p(x, y, z, t)$ , at point,  $Q(x, y, z)$ , and time,  $t$ , under the calm waterline can be expressed

$$p(x, y, z, t) = -\rho \frac{\partial \phi_0(x, y, z, t)}{\partial t} \quad (3.24)$$

In the Wheeler stretching approach, the velocities at the mean water level are applied to the true surface and the distribution from the sea bed to the wave surface is stretched accordingly. Introducing the scaled vertical coordinate,  $z'$

$$z' = [z - \eta(t)] \frac{d}{d + \eta(t)} \quad (3.25)$$

where  $z$  is the vertical coordinate of a point of interest,  $\eta(t)$  is wave elevation,  $d$  is water depth. For infinite water depth, the scaled coordinate  $z'$  can be expressed as

$$z' = z - \eta(t) \quad (3.26)$$

Substituting the vertical coordinate  $z$  by the scaled vertical coordinate  $z'$ , the dynamic pressure at the any point on the submerged surfaces can be computed. In the end, the Froude-Krylov forces on the  $i$ th body can be calculated as

$$\mathbf{F}_i^{FK} = \int_{S_{wet}} p(x, y, z - \eta(t), t) \mathbf{n} ds \quad (3.27)$$

### 3.1.5 Convergence Studies

#### 3.1.5.1 Convergence Studies on Mesh

Convergence studies on the computational mesh were conducted in the first place. As presented in Fig. 3.5, the added mass in the heave direction of Body 1 caused by the heave motion of Body 2 were computed by WAMIT using different numbers of panels. It can be seen from the results that a total of 2064 panels is sufficient to represent the three bodies.

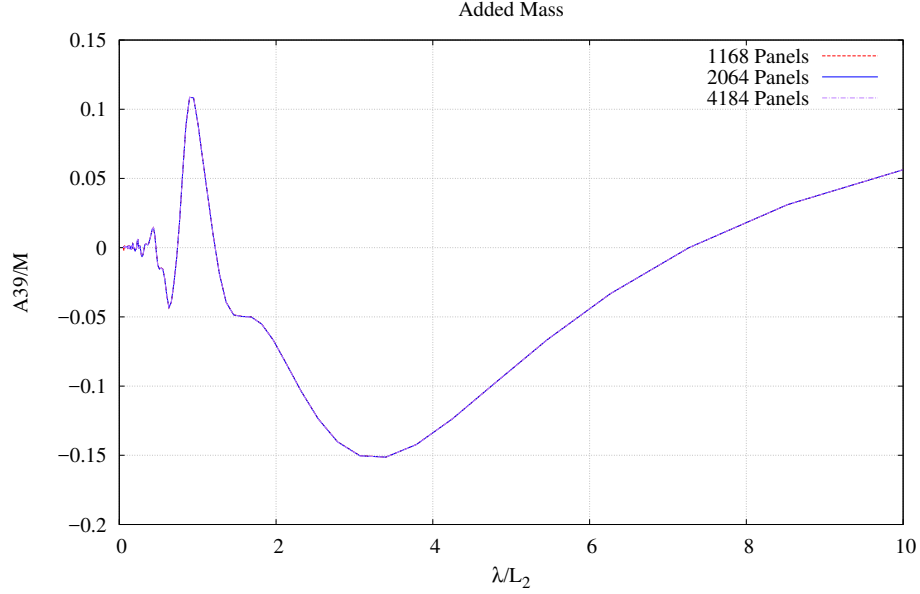


Figure 3.5: Convergence Study on the Mesh Size

### 3.1.5.2 Convergence Studies on Time Step

In the simulations, the two-step Adams-Bashforth method was employed for time marching. Sensitivity studies on the time step were carried out. Predicted motions of PTO-1 in regular waves with a period of 1.69 s (model scale) for the case of T1-D0 using time steps, 0.005 s, 0.0075 s and 0.01 s, are presented in Fig. 3.6

Slight drift can be observed in the results after a long-time simulation, resulting the violation of constraint condition for displacement. This was further investigated by checking the relative displacements between  $X_{A1}$  and  $X_{A2}$ , which should be zero in theory:

$$E_{Ax} = \left| \frac{X_{A1} - X_{A2}}{X_A} \right| \times 100\% \quad (3.28)$$

where  $X_{A1}$  and  $X_{A2}$  are the horizontal motions of the hinge joint,  $A$ , calculated based on the motions of Bodies 1 and 2, respectively, and  $X_A$  is the horizontal displace-

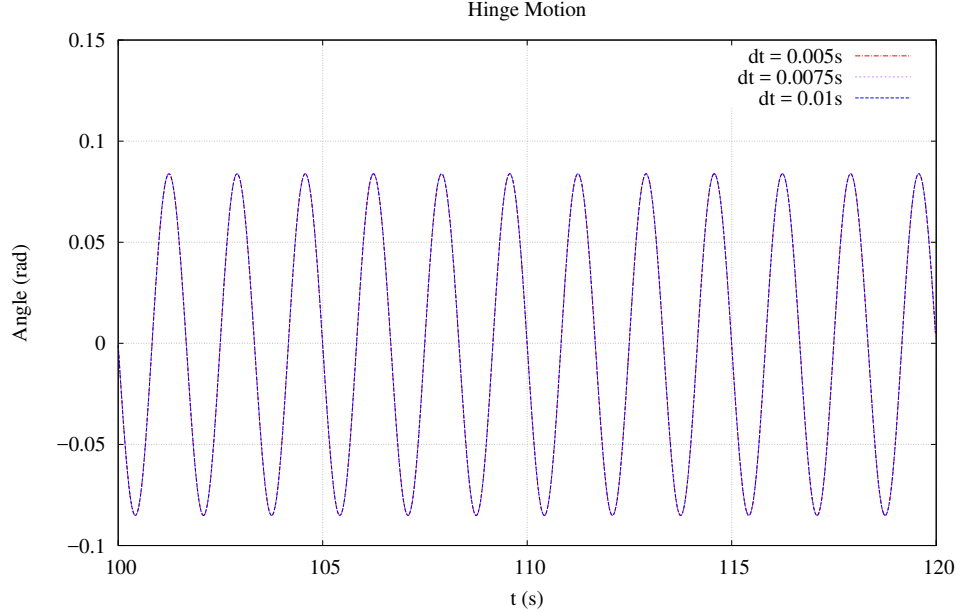


Figure 3.6: Time Histories of Simulated Hinge Motions

ment amplitude of the hinge joint  $A$ . As shown in Fig. 3.7, the error was reduced significantly when a smaller time step was used.

In the following simulations, the time step was set as 0.0075 second. After a 120-second simulation (model scale), the accumulated error is below 0.05%, which is acceptable and does not cause any noticeable change in the relative pitch motions.

## 3.2 Validation Studies

The numerical method is validated using the model tests data on the second generation SeaWEED, as detailed in Chapter 2. The results applying nonlinear and linear Froude-Krylov forces are compared with the experimental results for both free hinge cases and damped cases. In the following, cases are defined by the combination of body-length and damper set-up, as detailed in Table 2.3 and Table 2.5. For example,

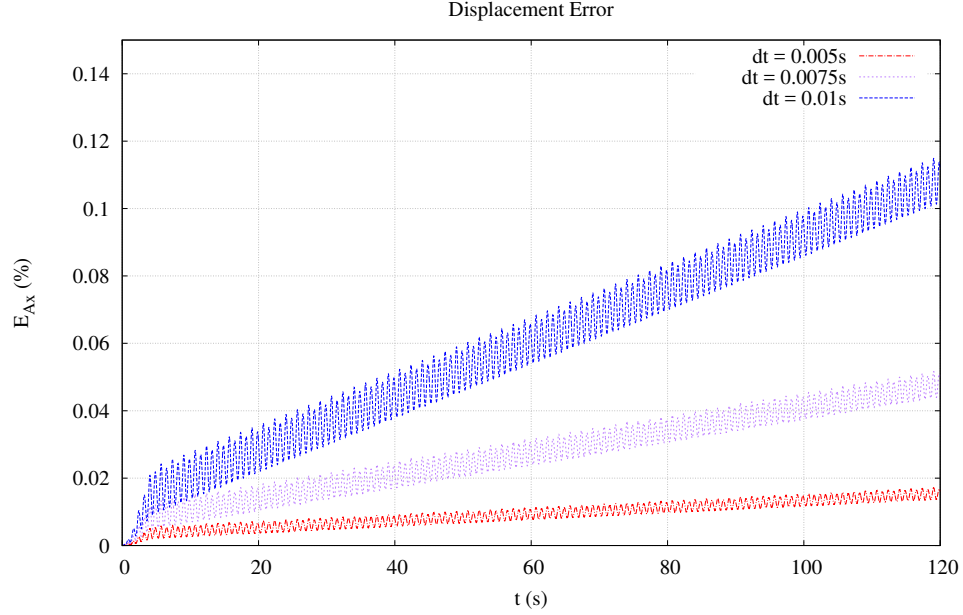


Figure 3.7: Time Histories of Relative Displacement Error

T1-D2 denotes a case with body length, T1, and damper set-up, D2.

### 3.2.1 Free Hinge Conditions

Validation studies were first carried out for the SeaWEED without PTOs. The computed relative pitch motions at the two PTOs with nonlinear and linear F-K forces were compared with the experimental data for various combinations of truss lengths as listed in Table 2.3.

Figs. 3.8 and 3.9 present the comparisons of the non-dimensional relative pitch angles at PTO-1 and PTO-2 for Case T1-D0 (see Table 2.3) in terms of the wave length to body length ratio, i.e.,  $\frac{\lambda}{L_2}$ , where  $\lambda$  is the wave length and  $L_2$  is the length of Body 2, which is constant in all the combinations of truss lengths. The relative pitch angle,  $\theta$ , is non-dimensionalized as  $\frac{\theta}{k\eta_0}$ , where  $k$  is the wave number and  $\eta_0$  is

the amplitude of incident waves. The numerical results for Case 2 are presented in Figs. 3.10 and 3.11.

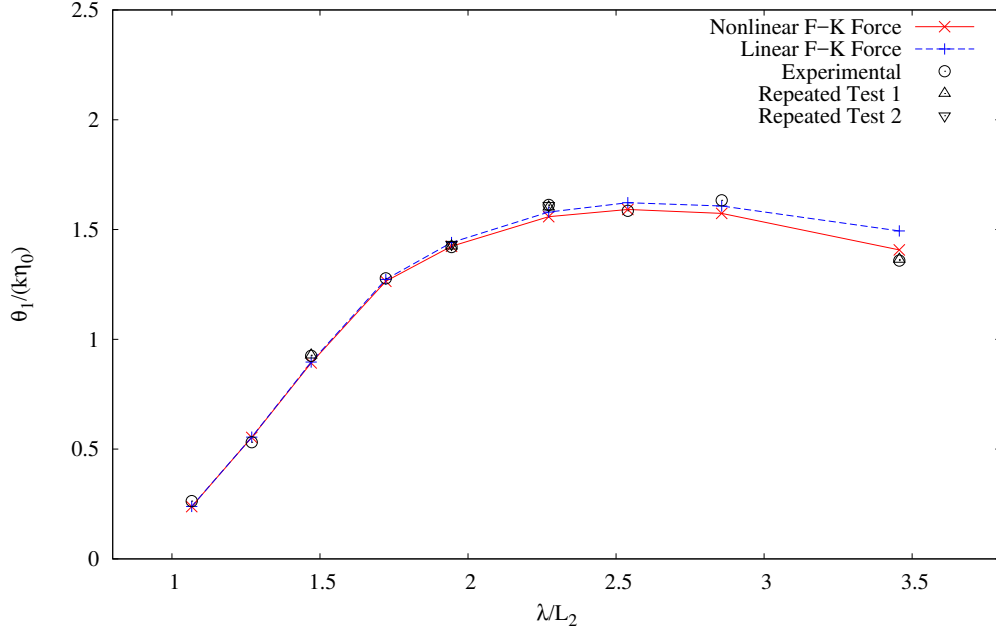


Figure 3.8: Non-dimensional Relative Pitch Angles at PTO-1 (Case T1-D0)

As shown in Table 2.3, the lengths of Body 3 for Case T3-D0 and T4-D0 are greater than that for Case T2-D0 while the lengths of Body 1 and Body 2 remain constant. The corresponding relative pitch motions at the joints are presented in Figs. 3.13, 3.13, 3.14 and 3.15.

As shown in these comparisons, the numerical results agree very well with the experimental data for the cases without PTOs. In addition, for longer wave cases, better agreement is achieved when considering the nonlinear F-K forces.

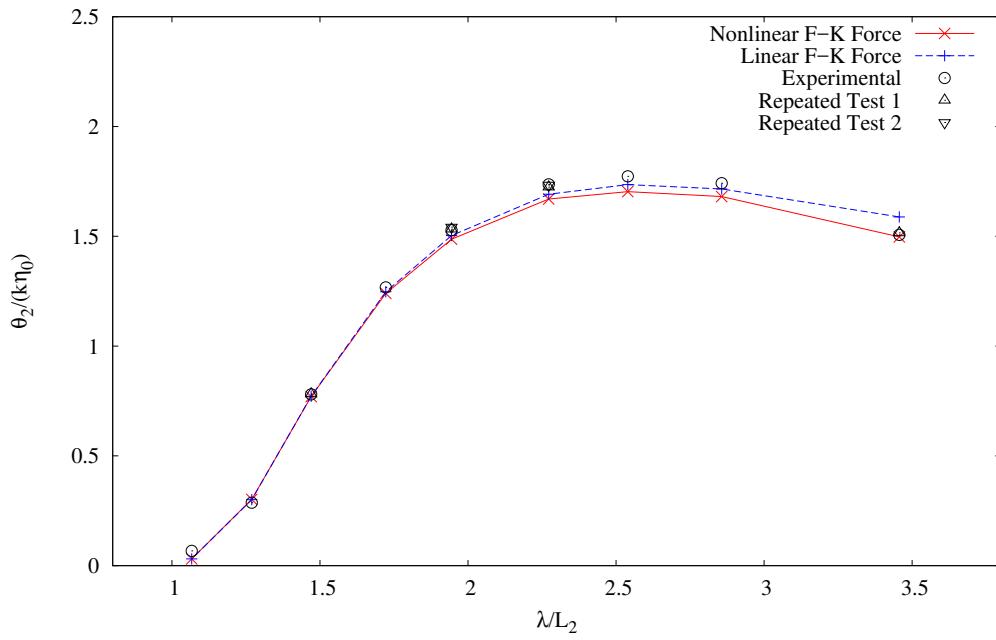


Figure 3.9: Non-dimensional Relative Pitch Angles at PTO-2 (Case T1-D0)

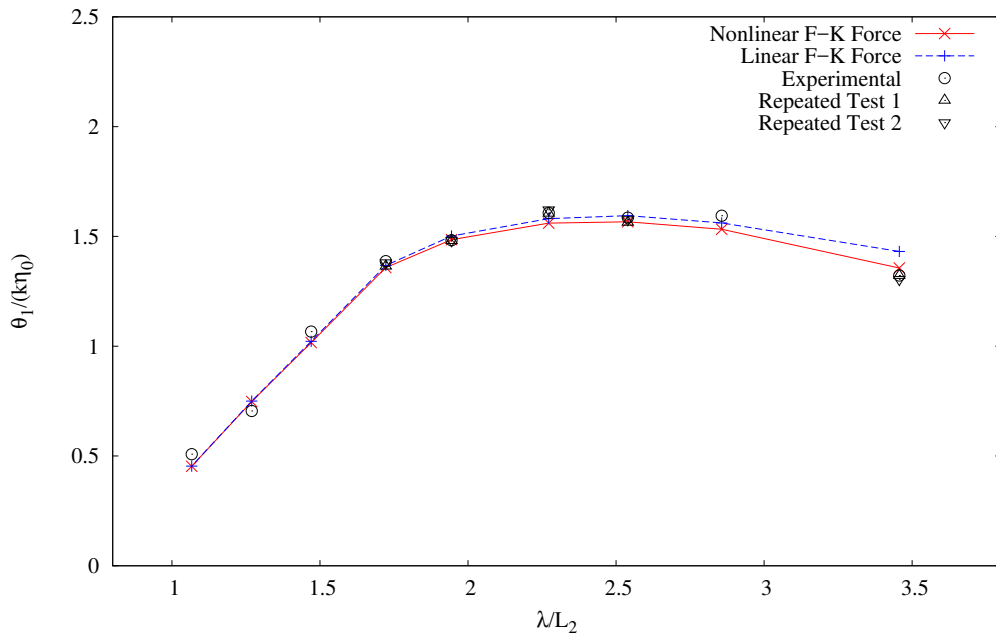


Figure 3.10: Non-dimensional Relative Pitch Angles at PTO-1 (Case T2-D0)

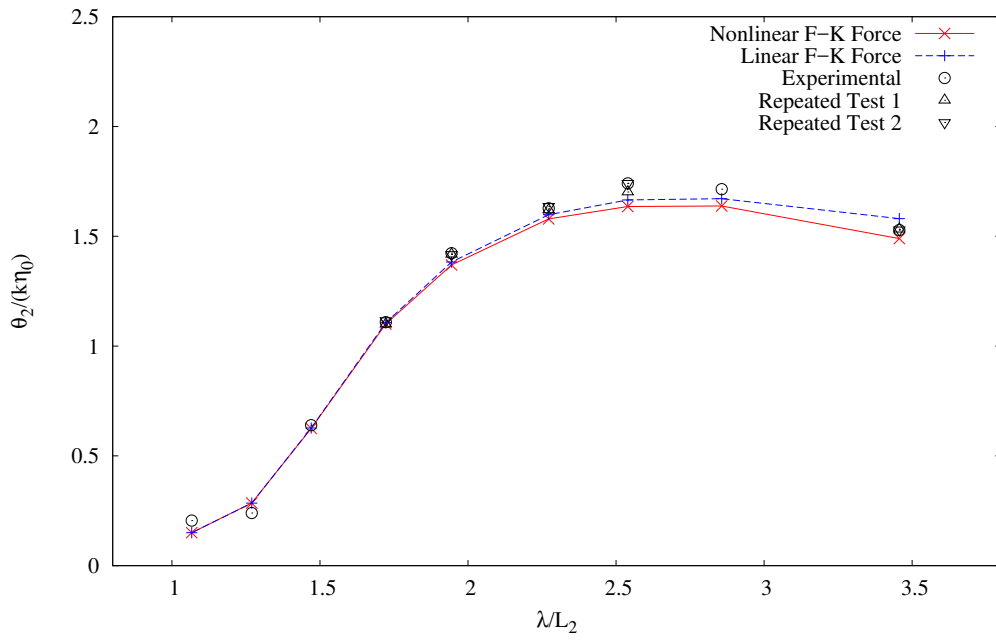


Figure 3.11: Non-dimensional Relative Pitch Angles at PTO-2 (Case T2-D0)

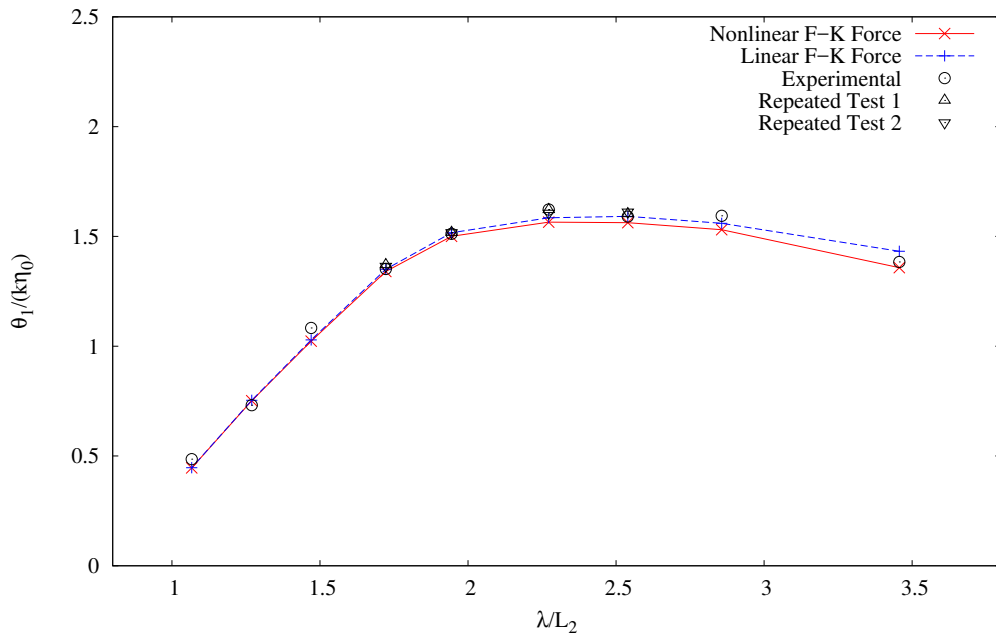


Figure 3.12: Non-dimensional Relative Pitch Angles at PTO-1 (Case T3-D0)

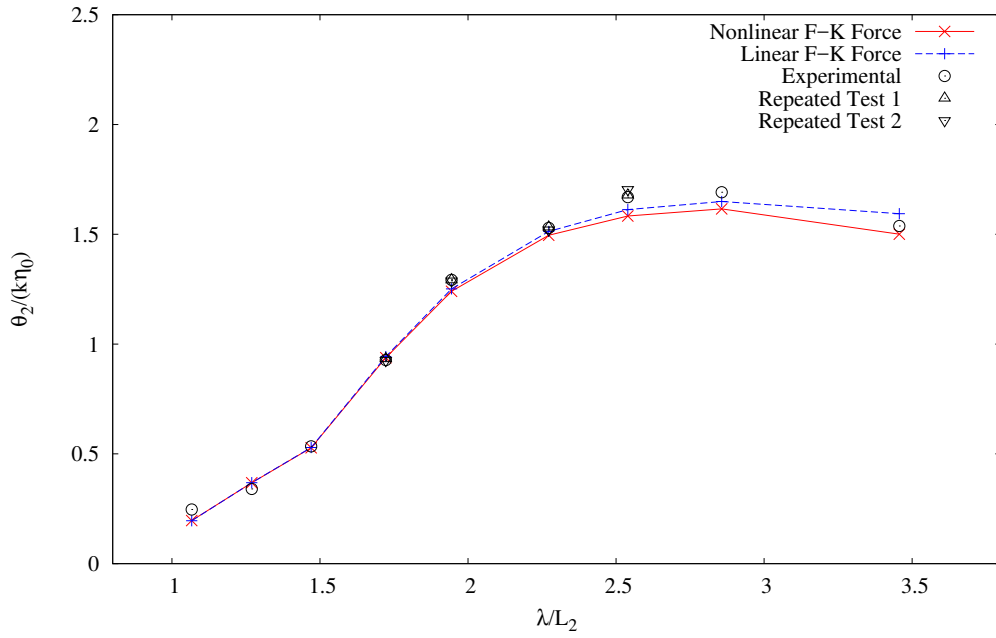


Figure 3.13: Non-dimensional Relative Pitch Angles at PTO-2 (Case T3-D0)

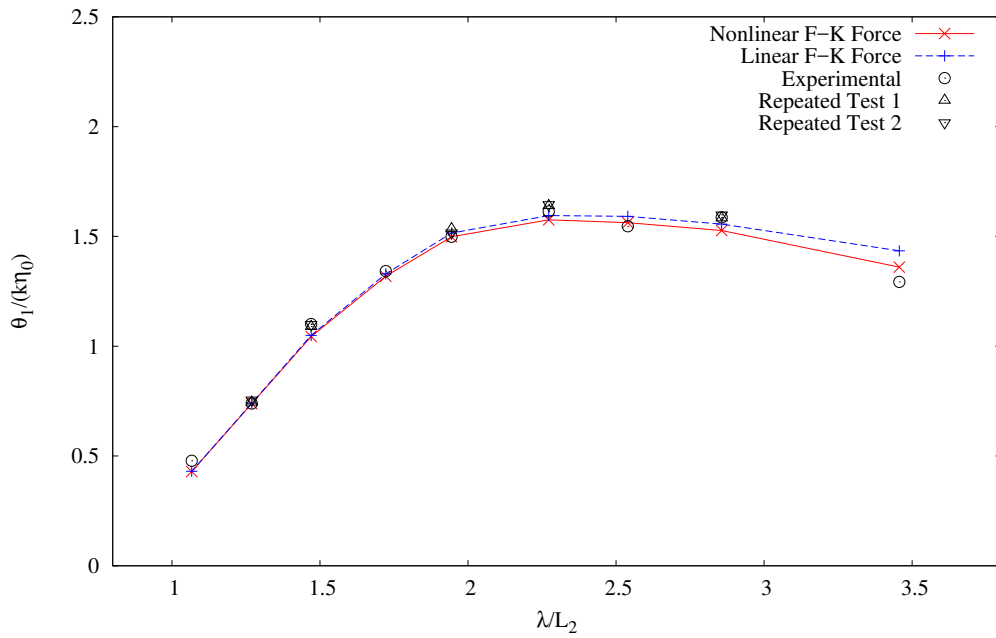


Figure 3.14: Non-dimensional Relative Pitch Angles at PTO-1 (Case T4-D0)

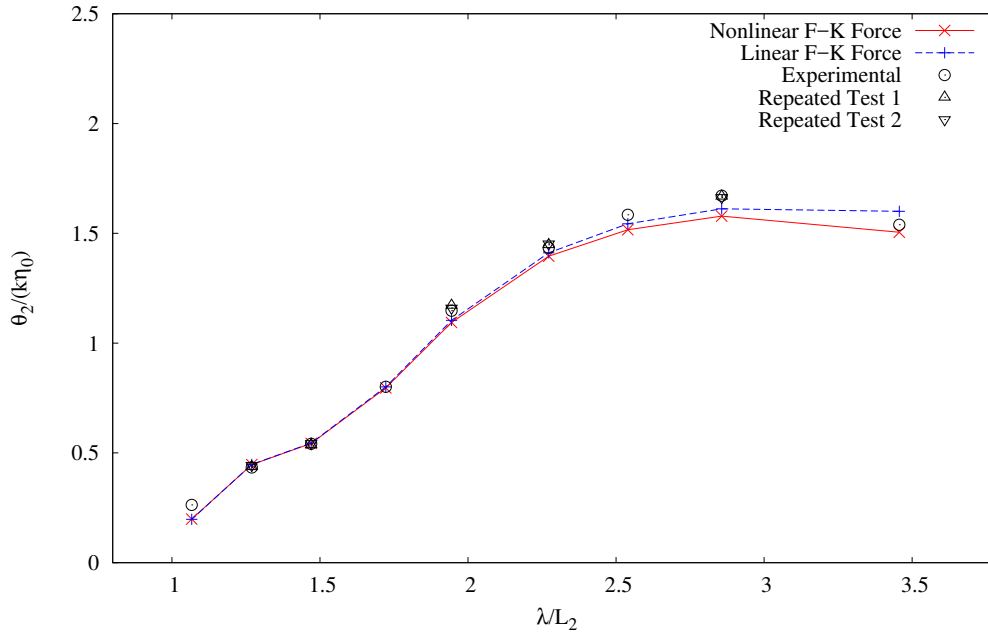


Figure 3.15: Non-dimensional Relative Pitch Angles at PTO-2 (Case T4-D0)

### 3.2.2 Damped Conditions

Experimental tests were carried out with three damper set-ups as shown in Table 2.5, i.e., with PTOs. In each set-up, the spring was adjusted to provide desired damping force. Figs. 2.18, 2.19 and 2.20 present the damping coefficients of the two dampers obtained from calibrations and measurements during tests for the three set-ups.

Using the equivalent damping coefficients obtained from the measurements during tests as input, numerical simulations were carried out to predict relative motions at the joints of PTOs. Figs. 3.16 and 3.17 present the non-dimensional pitch angles and Figs. 3.18 and 3.19 show the corresponding capture widths by PTO-1 and PTO-2 for the damping Case T1-D1. It can be seen that the power absorbed by the two PTOs

is similar.

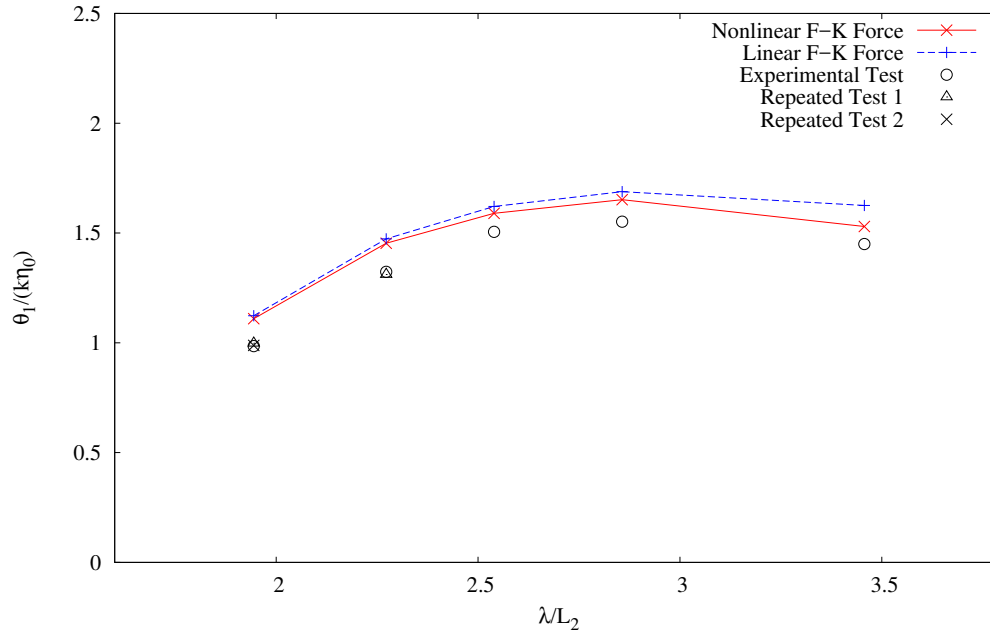


Figure 3.16: Non-dimensional Relative Pitch Angles at PTO-1 (Case T1-D1)

For the damping Case T1-D2, Figs. 3.20, 3.21, 3.22 and 3.23 show the non-dimensional hinge angular motions and the capture widths by PTO-1 and PTO-2. Due to the increased resistance from the damper, the response of PTO-2 was decreased in comparison with that in Case T1-D1.

Further, additional two sets of tests were carried out by activating PTO-1 and PTO-2 independently using the same damping in Case T1-D2 to validate the present method. Figs. 3.24, 3.25 and 3.26 present the non-dimensional hinge motions and the capture widths of PTO-1 and PTO-2 with only PTO-1 activated. Compared to the case where both dampers were activated, the disengagement of the damper PTO-2 led to an increase of the hinge motions at PTO-2.

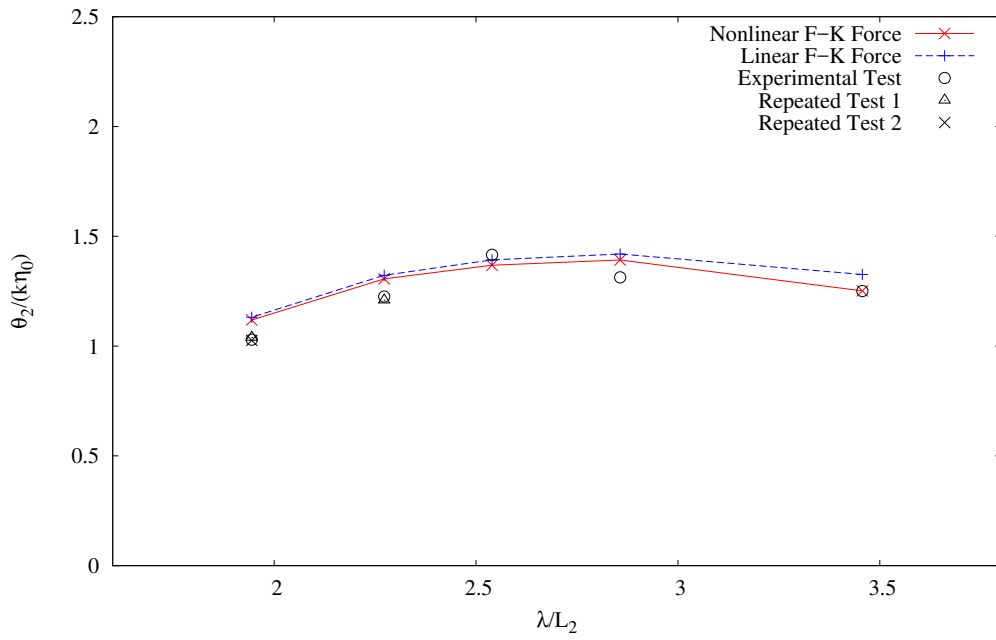


Figure 3.17: Non-dimensional Relative Pitch Angles at PTO-2 (Case T1-D1)

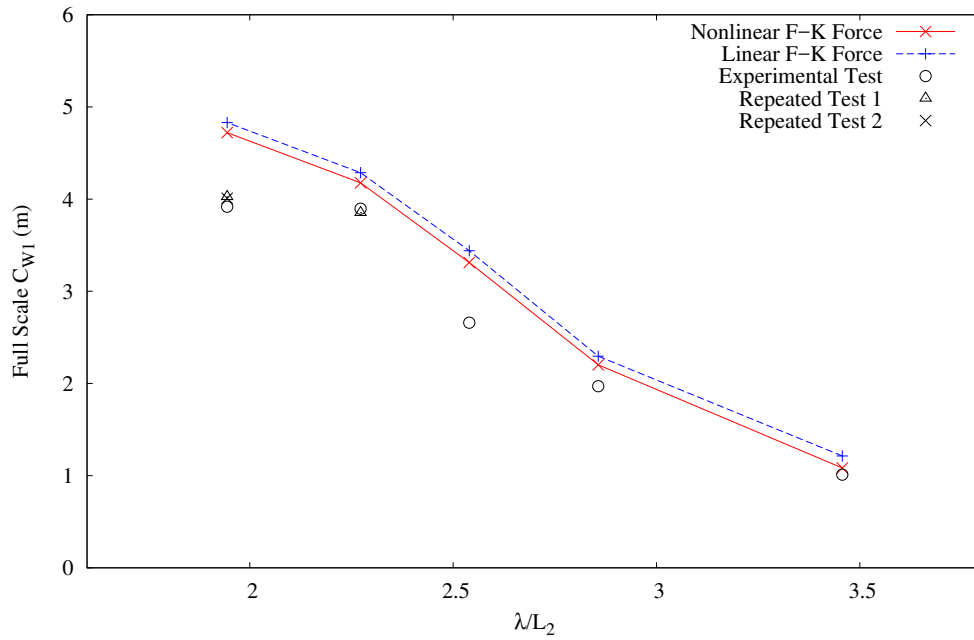


Figure 3.18: Full-scale Capture Width at PTO-1 (Case T1-D1)

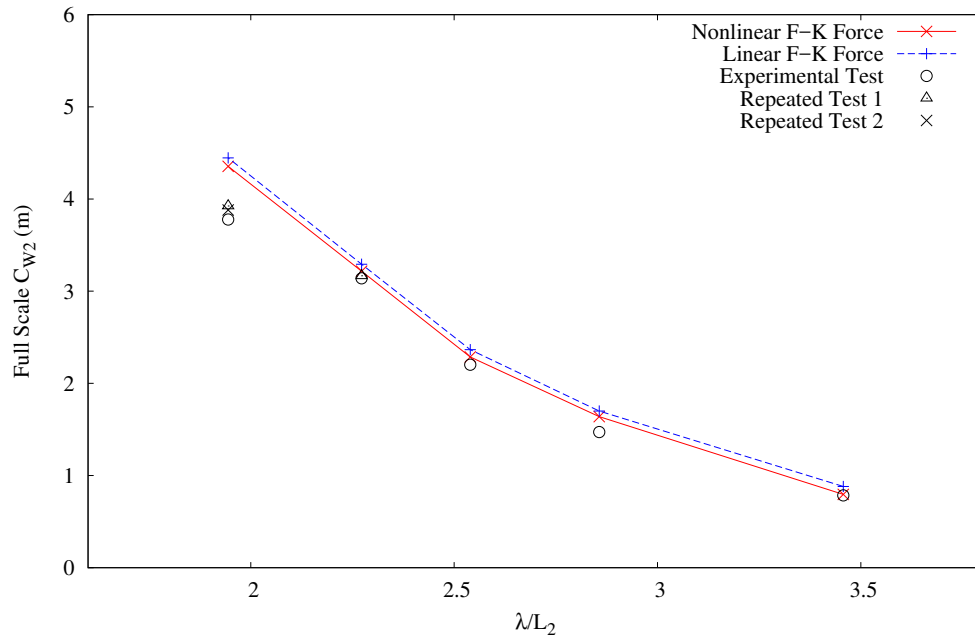


Figure 3.19: Full-scale Capture Width at PTO-2 (Case T1-D1)

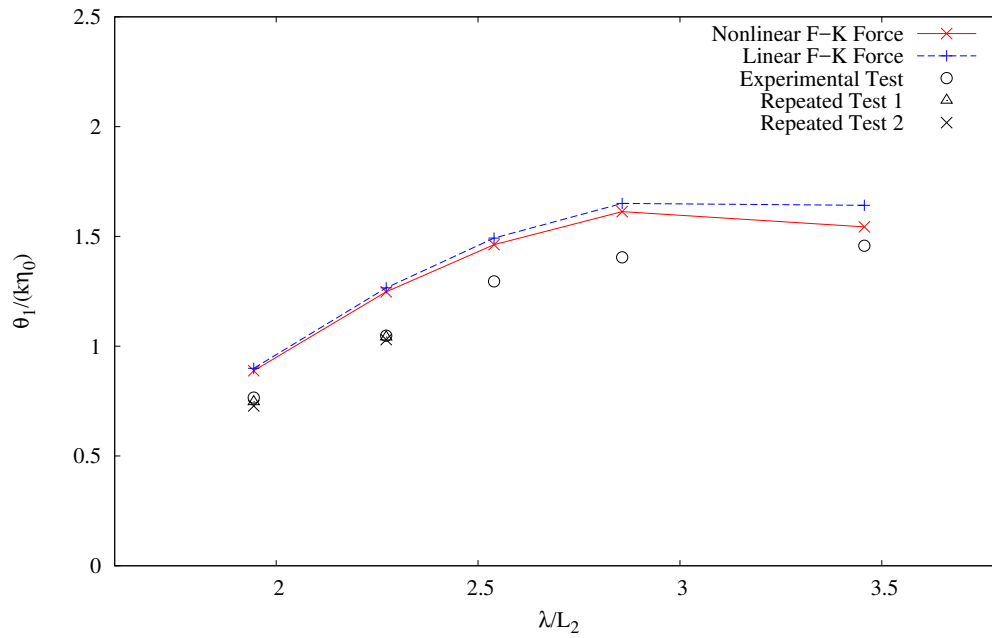


Figure 3.20: Non-dimensional Relative Pitch Angles at PTO-1 (Case T1-D2)

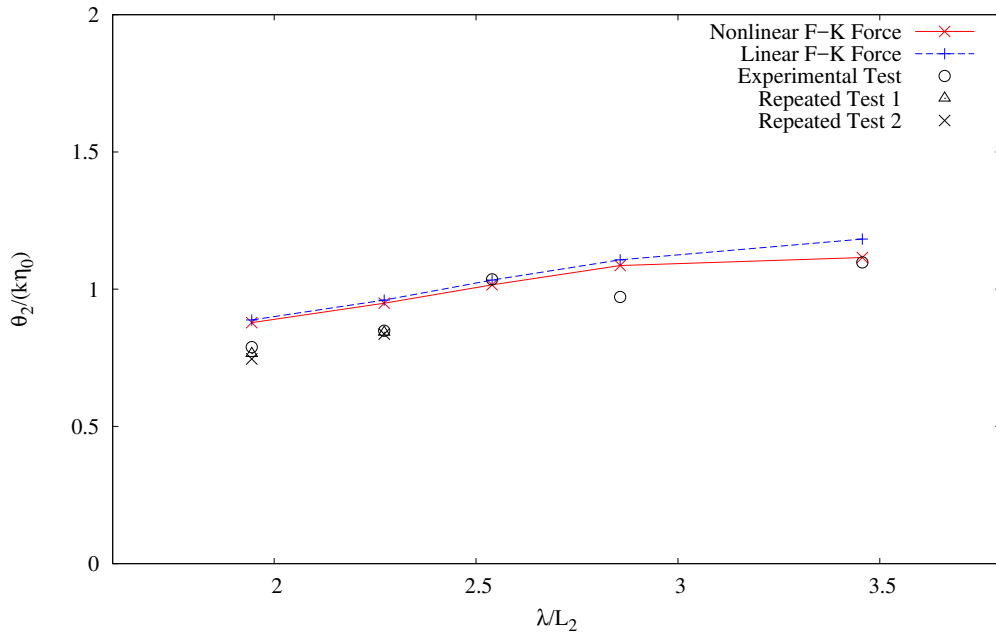


Figure 3.21: Non-dimensional Relative Pitch Angles at PTO-2 (Case T1-D2)

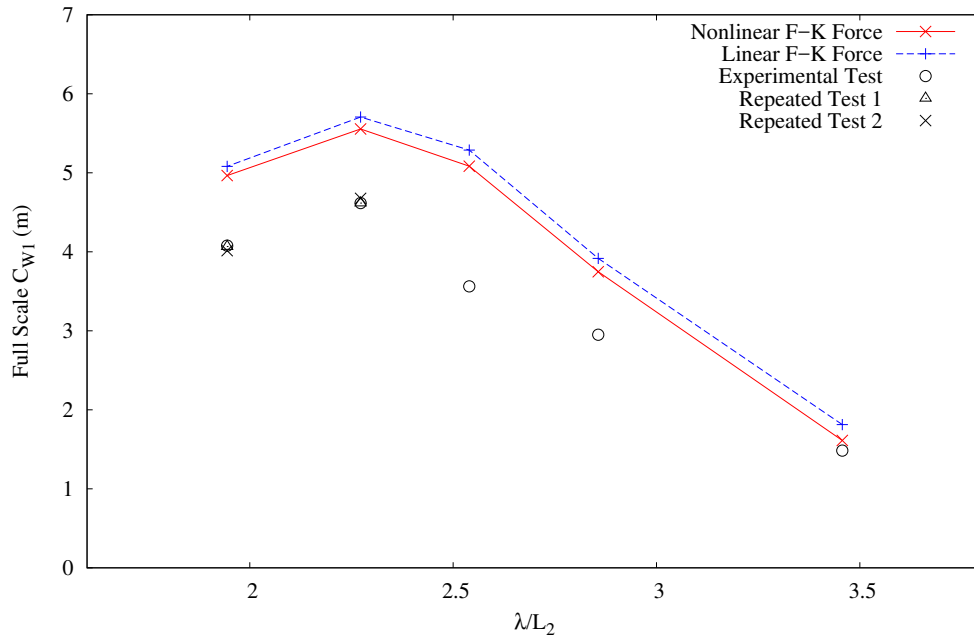


Figure 3.22: Full-scale Capture Width at PTO-1 (Case T1-D2)

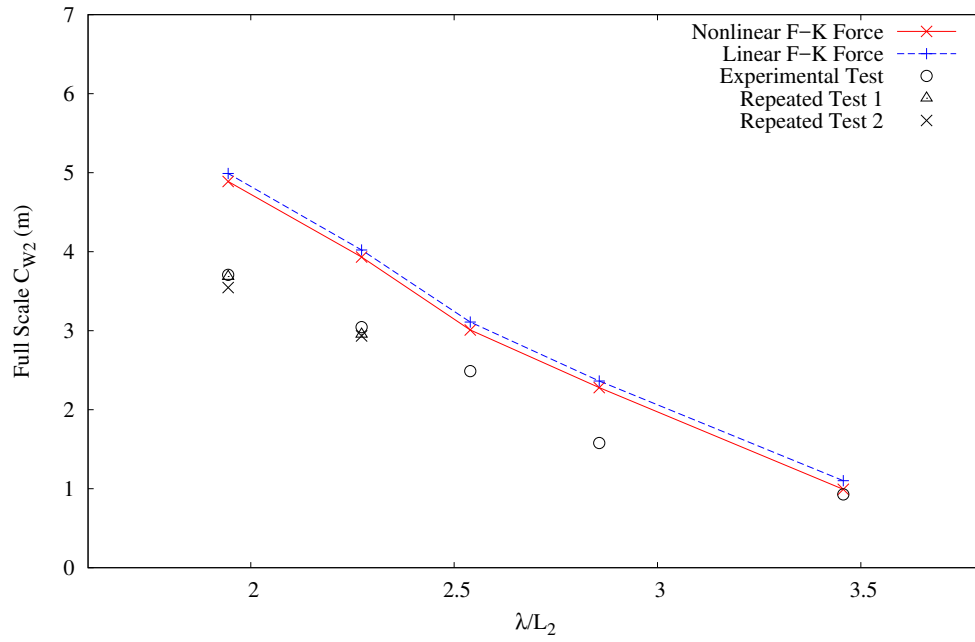


Figure 3.23: Full-scale Capture Width at PTO-2 (Case T1-D2)

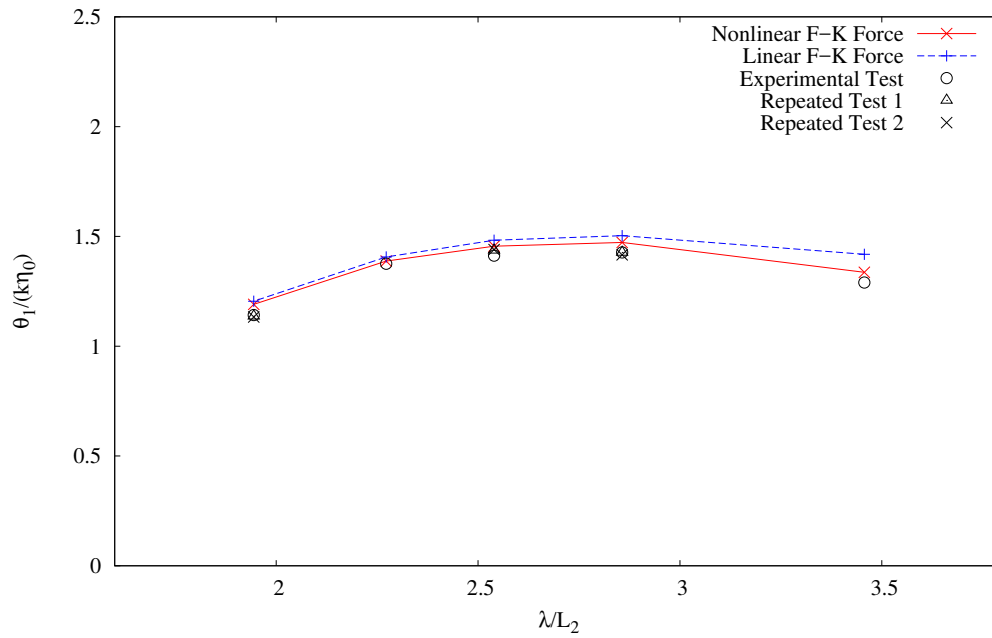


Figure 3.24: Non-dimensional Relative Pitch Angles at PTO-1 (Case T1-D3)

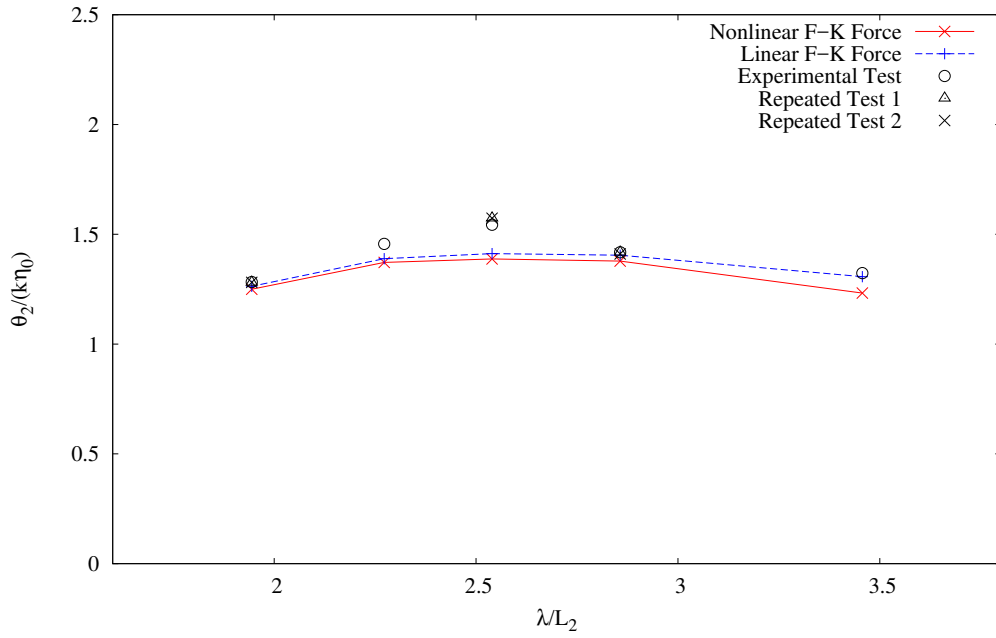


Figure 3.25: Non-dimensional Relative Pitch Angles at PTO-2 (Case T1-D3)

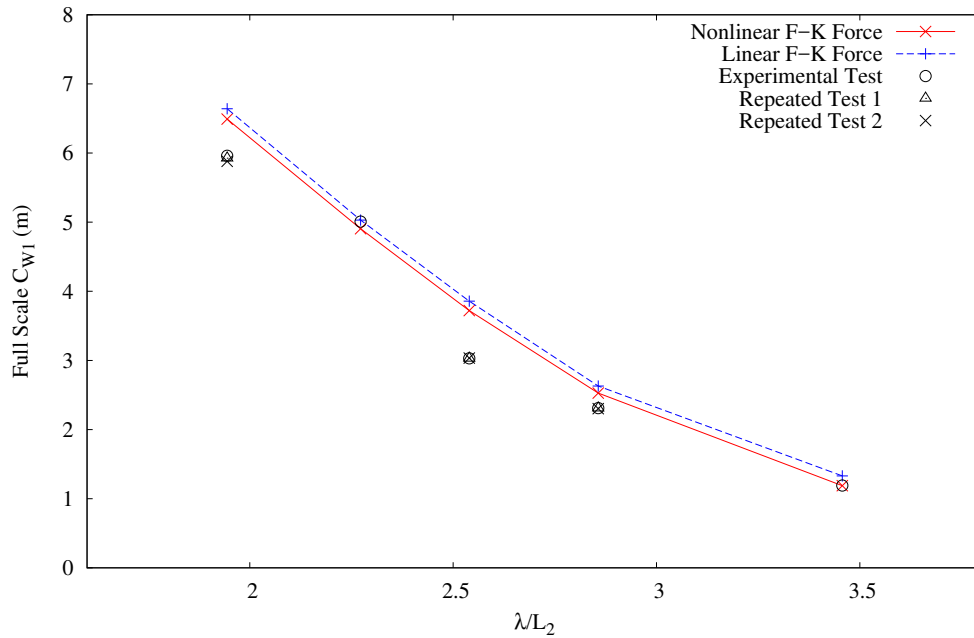


Figure 3.26: Full-scale Capture Width at PTO-1 (Case T1-D3)

Figs. 3.27, 3.28 and 3.29 present the non-dimensional hinge angles and the capture widths of PTO-1 and PTO-2 with only PTO-2 activated. In this case, both the relative pitch motions of PTO-1 and PTO-2 are larger in comparison with those for Case T1-D2.

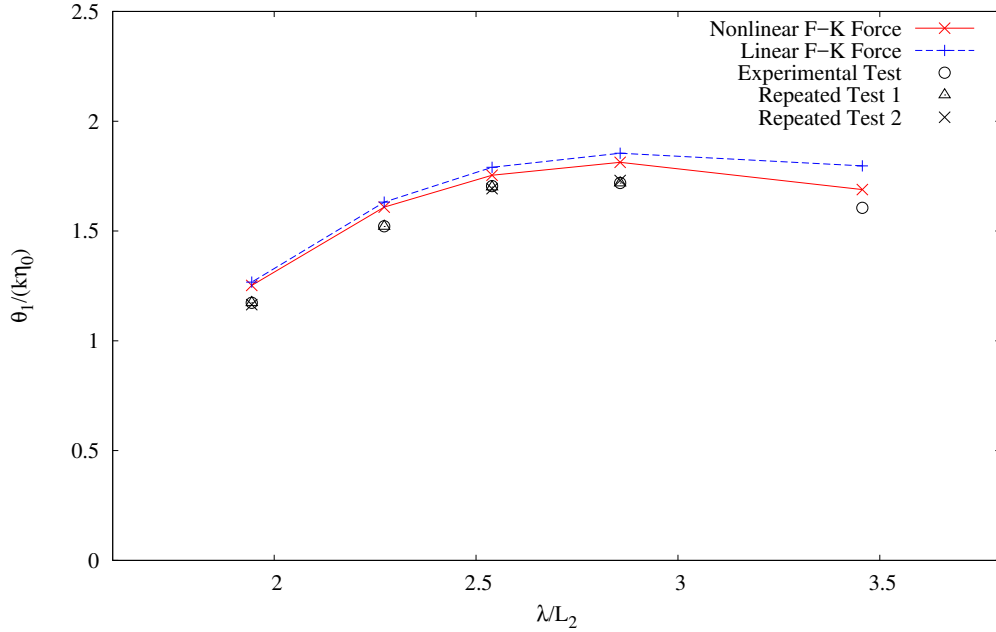


Figure 3.27: Non-dimensional Relative Pitch Angles at PTO-1 (Case T1-D4)

Further increasing the damping, the overall captured power widths in Case T1-D5 are less than that in Case T1-D2, as shown in Figs. 3.32 and 3.33. The corresponding non-dimensional angular motions are presented in Figs. 3.30 and 3.31.

As a summary, it can be seen that good repeatability was achieved from the model tests. Relative pitch angles and capture widths were slightly over predicted by the present numerical model for damping cases. This could be due to various reasons, such as the energy loss in the measuring system due to the frictions between the connectors

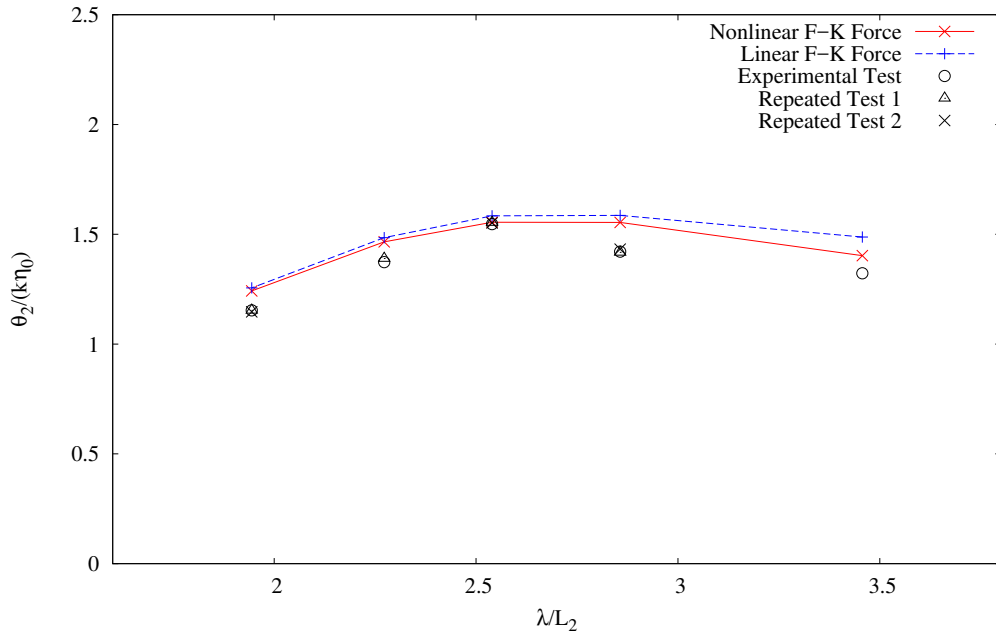


Figure 3.28: Non-dimensional Relative Pitch Angles at PTO-2 (Case T1-D4)

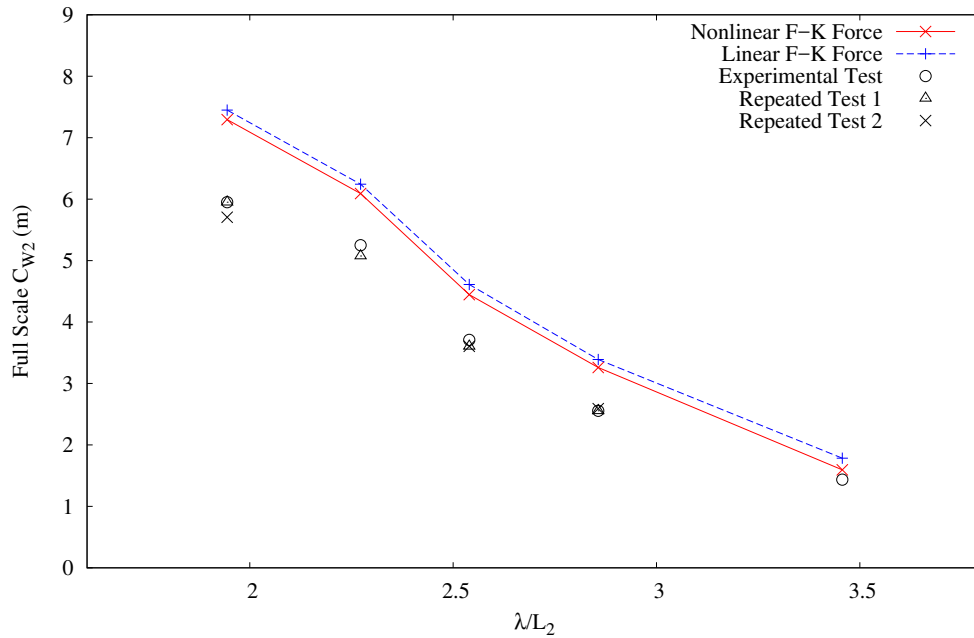


Figure 3.29: Full-scale Capture Width at PTO-2 (Case T1-D4)

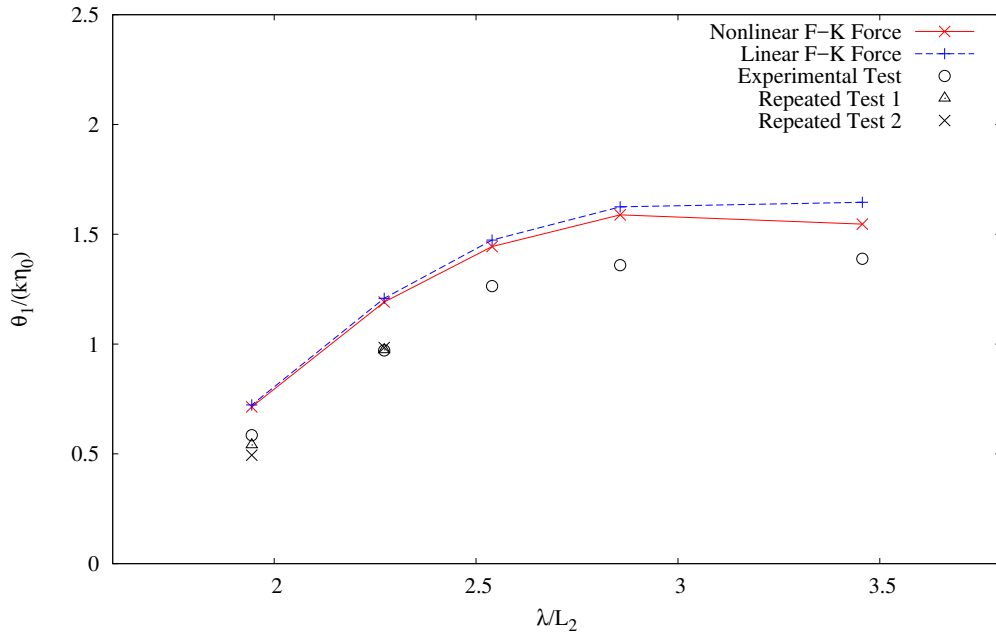


Figure 3.30: Non-dimensional Relative Pitch Angles at PTO-1 (Case T1-D5)

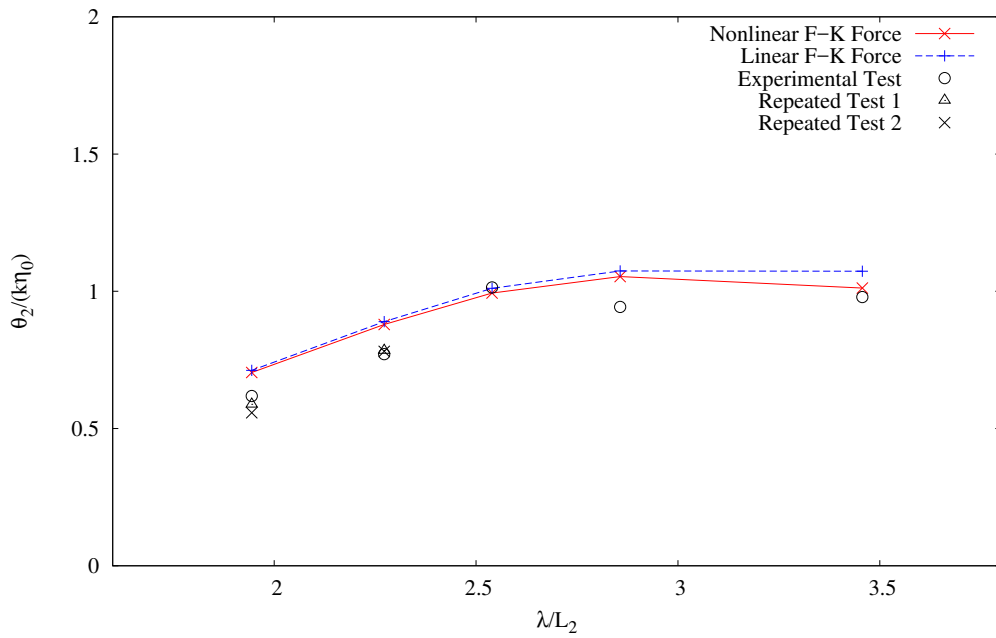


Figure 3.31: Non-dimensional Relative Pitch Angles at PTO-2 (Case T1-D5)

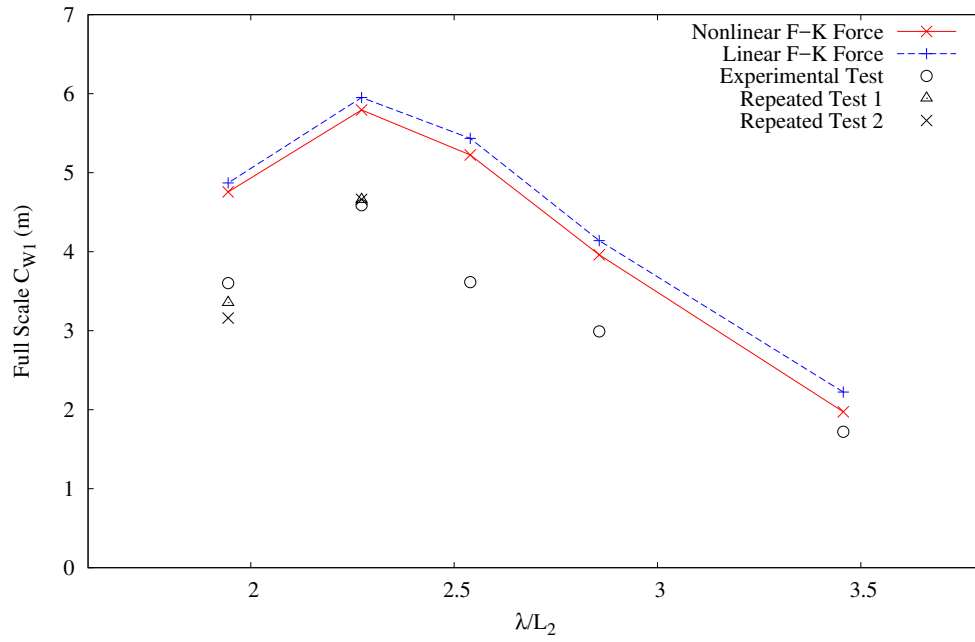


Figure 3.32: Full-scale Capture Width at PTO-1 (Case T1-D5)

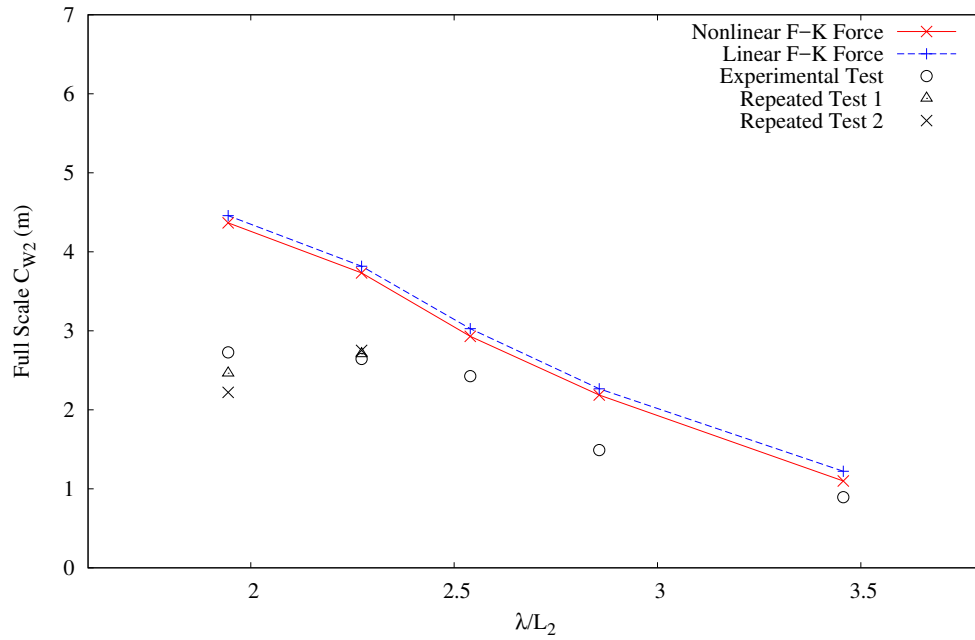


Figure 3.33: Full-scale Capture Width at PTO-2 (Case T1-D5)

and possible misalignment of the apparatus. Similar to the free-hinge cases, better predictions were achieved by using the nonlinear F-K forces for low-frequency-wave cases. The overall agreement between the experimental and computational results is satisfactory.

# Chapter 4

## Frequency-domain Simulation of SeaWEED

As shown in the previous chapter, the time-domain program can well predict the hinged motions and captured power of SeaWEED. However, to optimize the power output of SeaWEED for a target operation site, a more efficiency computer program is needed. Based on the methodologies used in the time-domain analysis and linearization of the wave forces and body motions, a frequency-domain program is developed. This chapter presents the mathematical formulations of the frequency-domain potential-flow program and validations using the experimental data.

### 4.1 Mathematical Formulation

The definition of the coordinate systems follows that in Chapter 3.

### 4.1.1 Equations of Motion and Constraint Matrix

Equations of motion of the three bodies can be expressed as

$$\sum_{k=1}^{18} [-\omega^2(\Delta_{jk} + A_{jk}) + i\omega B_{jk} + C_{jk}] \bar{\eta}_k = F_j^E, \quad j = 1, \dots, 18 \quad (4.1)$$

where  $\omega$  is the frequency of incident wave,  $\bar{\eta}_k$  is the complex amplitude of motion in mode  $k$ ,  $\Delta_{jk}$  are the masses or moments of inertia,  $A_{jk}$  and  $B_{jk}$  are the added mass and damping coefficients,  $C_{jk}$  are the hydrostatic restoring force coefficients, respectively.

The total exciting forces,  $F_j^E$ , include the Froude-Krylov forces,  $F_j^{FK}$ , forces due to diffracted waves,  $F_j^D$ , damping forces from the PTO systems,  $F_j^{PTO}$ , and constraint forces due to hinge joints,  $F_j^C$

$$F_j^E = F_j^{FK} + F_j^D + F_j^{PTO} + F_j^C, \quad j = 1, \dots, 18 \quad (4.2)$$

In the SeaWEED system, the PTO is due to the relative pitch motions at the hinge joints A and B, as shown in Fig. 4.1. The damping forces are computed as

$$F_j^{PTO} = \sum_{k=1}^{18} (-i\omega B_{jk}^{PTO} \bar{\eta}_k), \quad j = 1, \dots, 18 \quad (4.3)$$

where  $B_{jk}^{PTO}$  are the damping coefficients due to the PTO systems with

$$\begin{aligned} B_{5,5}^{PTO} &= -d_1 ; & B_{5,11}^{PTO} &= +d_1 \\ B_{11,5}^{PTO} &= +d_1 ; & B_{11,11}^{PTO} &= -d_1 - d_2 \\ B_{11,17}^{PTO} &= +d_2 ; & B_{17,11}^{PTO} &= +d_2 \\ B_{17,17}^{PTO} &= -d_2 \end{aligned} \quad (4.4)$$

where  $d_1$  and  $d_2$  are the damping coefficients at PTO-1 and PTO-2, respectively, and the rest terms of  $B_{jk}^{PTO}$  are zero.



Figure 4.1: Relative Pitch Angles

Denote the positions of hinge joint A on Body 1 and Body 2 as  $\mathbf{H}_{A1}$  and  $\mathbf{H}_{A2}$ , and those of hinge joint B on Body 2 and Body 3 as  $\mathbf{H}_{B2}$  and  $\mathbf{H}_{B3}$ , in the earth-fixed coordinate system,  $OXYZ$ , respectively, the following condition should be satisfied

$$\begin{bmatrix} \mathbf{H}_{1A} - \mathbf{H}_{2A} \\ \mathbf{H}_{2B} - \mathbf{H}_{3B} \end{bmatrix} = \mathbf{0} \quad (4.5)$$

The position of a hinge joint in the global coordinate system can be expressed using the motions of a rigid body and the relative position of the hinge joint in the body-fixed frame. Under the assumption that the motions are linear, Eq. (4.5) can be rewritten as

$$\begin{bmatrix} \bar{\eta}_i + \epsilon_{ijk} \bar{\eta}_{j+3} r_k^{A1} - \bar{\eta}_{i+6} - \epsilon_{ijk} \bar{\eta}_{j+9} r_k^{A2} \\ \bar{\eta}_{i+6} + \epsilon_{ijk} \bar{\eta}_{j+9} r_k^{B2} - \bar{\eta}_{i+12} - \epsilon_{ijk} \bar{\eta}_{j+15} r_k^{B3} \end{bmatrix} = \mathbf{0}, \quad i, j, k = 1 - 3 \quad (4.6)$$

where  $\epsilon_{ijk}$  is the Levi-Civita symbol,  $\mathbf{r}^{Am}$ ,  $m = 1, 2$  and  $\mathbf{r}^{Bm}$ ,  $m = 2, 3$ , are the position vectors of the hinge joints, A and B, respectively, in the body fixed coordinate system,  $o_m x_m y_m z_m$ , with respect to the origin  $o_m$ . Further, Eq. (4.6) can be expressed as

$$\sum_{k=1}^{18} J_{jk} \bar{\eta}_k = 0, \quad j = 1 - 6 \quad (4.7)$$

where  $J_{jk}$  are elements of the Jacobian matrix  $\mathbf{J}$  in size of  $6 \times 18$  in this work. The

elements in  $\mathbf{J}$  are detailed as

$$\begin{aligned}
J_{1,1} &= 1 ; & J_{1,5} &= r_3^{A1} ; & J_{1,7} &= -1 ; & J_{1,11} &= -r_3^{A2} \\
J_{2,2} &= 1 ; & J_{2,6} &= r_1^{A1} ; & J_{2,8} &= -1 ; & J_{2,12} &= -r_1^{A2} \\
J_{3,3} &= 1 ; & J_{3,5} &= r_1^{A1} ; & J_{3,9} &= -1 ; & J_{3,11} &= -r_1^{A2} \\
J_{4,7} &= 1 ; & J_{4,11} &= r_3^{B2} ; & J_{4,13} &= -1 ; & J_{4,17} &= -r_3^{B3} \\
J_{5,8} &= 1 ; & J_{5,12} &= r_1^{B2} ; & J_{5,14} &= -1 ; & J_{5,18} &= -r_1^{B3} \\
J_{6,9} &= 1 ; & J_{6,11} &= r_1^{B2} ; & J_{6,15} &= -1 ; & J_{6,17} &= -r_1^{B3}
\end{aligned} \tag{4.8}$$

where the rest are zero.

As the constraint forces do not change the energy of the whole system (Witkin, 1997), they can be expressed as

$$F_j^C = \sum_{k=1}^6 J_{jk}^T \lambda_k, \quad j = 1, \dots, 18 \tag{4.9}$$

where  $T$  denotes transpose and  $\lambda_k$  are the Lagrange multipliers.

Combining Eqs. (4.1), (4.7) and (4.9), and expressing them in a matrix form, a system of equations can be obtained

$$\begin{bmatrix} [-\omega^2(\mathbf{\Delta} + \mathbf{A}) + i\omega(\mathbf{B} + \mathbf{B}^{PTO}) + \mathbf{C}] & \mathbf{J}^T \\ & \mathbf{0} \end{bmatrix} \begin{bmatrix} \bar{\boldsymbol{\eta}} \\ \boldsymbol{\lambda} \end{bmatrix} = \begin{bmatrix} \mathbf{F}^{FK} + \mathbf{F}^D \\ \mathbf{0} \end{bmatrix} \tag{4.10}$$

#### 4.1.2 Power Absorption in Regular and Irregular Waves

The complex constraint motion amplitudes and the Lagrange multipliers (hence the constraint forces) can be obtained simultaneously by solving Eq. 4.10, and the average power absorbed by PTO-1,  $P_1^N$ , and PTO-2,  $P_2^N$  in a regular wave can be

calculated as

$$P_1^N = \frac{1}{2}\omega^2\eta_0^2d_1 |\bar{\eta}_5 - \bar{\eta}_{11}|^2 \quad (4.11)$$

$$P_2^N = \frac{1}{2}\omega^2\eta_0^2d_2 |\bar{\eta}_{11} - \bar{\eta}_{17}|^2 \quad (4.12)$$

where  $\eta_0$  is the amplitude of incident wave.

Introducing the wave power per unit crest length

$$P_W = \frac{\rho g^2 \eta_0^2}{4\omega} \quad (4.13)$$

the power capture width,  $C_i$ , by PTO-i is given by

$$C_i = \frac{P_i^N}{P_W}, \quad i = 1, 2 \quad (4.14)$$

In irregular waves, under a certain sea state,  $(H_s, T_p)$ , the average wave power,  $P_W^I(H_s, T_p)$ , can be expressed as

$$P_W^I(H_s, T_p) = \int_0^\infty \frac{\rho g^2}{2\omega} S(H_s, T_p, \omega) d\omega \quad (4.15)$$

where  $S(H_s, T_p, \omega)$  is the wave spectrum.

For an intended operation site, the annual average wave power,  $P_W^A$ , is the summation of the average wave power of every single sea state weighted by its probability of occurrence,  $\mu(H_s, T_p)$ ,

$$P_W^A = \sum_{H_s} \sum_{T_p} \mu(H_s, T_p) P_W^I(H_s, T_p) \quad (4.16)$$

Note that the summations are over the ranges of  $H_s$  and  $T_p$ . The average power captured by SeaWEED under a certainty sea state,  $(H_s, T_p)$ ,  $P_S^I(H_s, T_p)$ , can be computed as

$$\begin{aligned} P_S^I(H_s, T_p) &= \int_0^\infty [\omega^2 d_1 S(H_s, T_p, \omega) |\bar{\eta}_5 - \bar{\eta}_{11}|^2 \\ &+ \omega^2 d_2 S(H_s, T_p, \omega) |\bar{\eta}_{11} - \bar{\eta}_{17}|^2] d\omega \end{aligned} \quad (4.17)$$

and the annual power absorption,  $P_S^A$ , can be obtained applying Eq. (4.16) as

$$P_S^A = \sum_{H_s} \sum_{T_p} \mu(H_s, T_p) P_S^I(H_s, T_p) \quad (4.18)$$

The annual capture width,  $C^A$ , can finally be calculated as

$$C^A = \frac{P_S^A}{P_W^A} \quad (4.19)$$

## 4.2 Validation Studies

### 4.2.1 First Generation SeaWEED Simulation

In the model test of the first generation SeaWEED, the relative pitch motions and captured power at PTO-1 were measured (Lundrigan, 2013). Figure 4.2 presents the comparisons of the non-dimensional relative pitch angles at PTO-1 for free-hinged conditions. The  $x$ -axis shows the wave length to body length ratio, i.e.,  $\lambda/L_2$ , where  $\lambda$  is the wave length and  $L_2$  is the length of Body 2. The relative pitch angle,  $\theta$ , is non-dimensionalized as  $\frac{\theta}{k\eta_0}$ , where  $k$  is the wave number and  $\eta_0$  is the amplitude of incident waves.

Using the damping coefficients obtained from the model tests (Lundrigan, 2013), simulations with the PTO systems activated were also conducted. Figs. 4.3 and 4.4 present the non-dimensional relative pitch angles and corresponding capture widths at PTO-1.

As can be seen from the plots, the general trend of the numerical and experimental results is the same. However, due to lack of model test details and repeated tests data, the numerical method is validated using the test data for the second generation SeaWEED conducted at the towing tank of MUN, as detailed in Chapter 2.

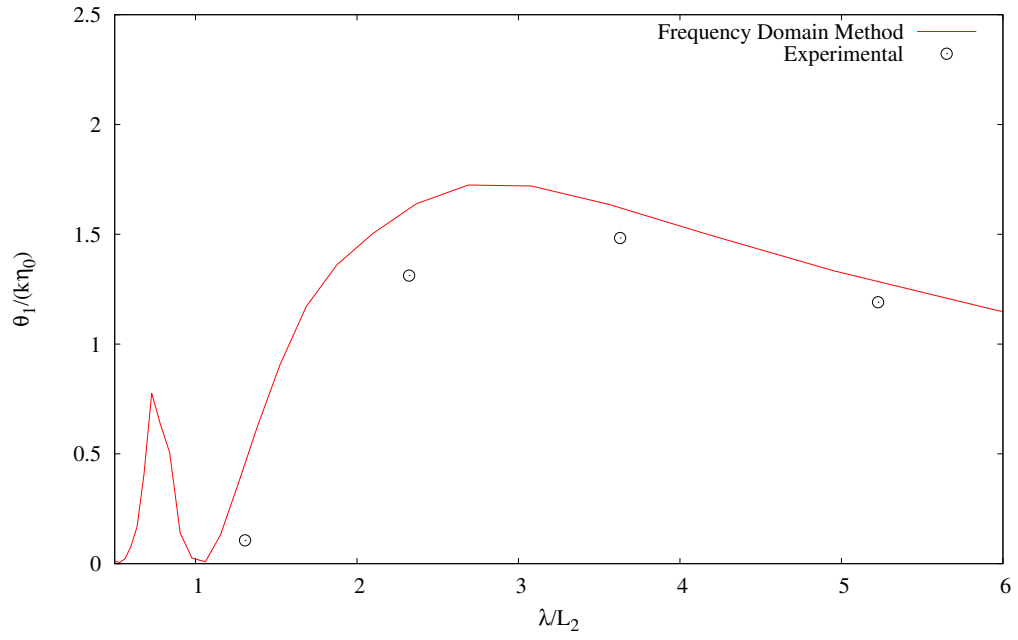


Figure 4.2: Non-dimensional Relative Pitch Angles at PTO-1

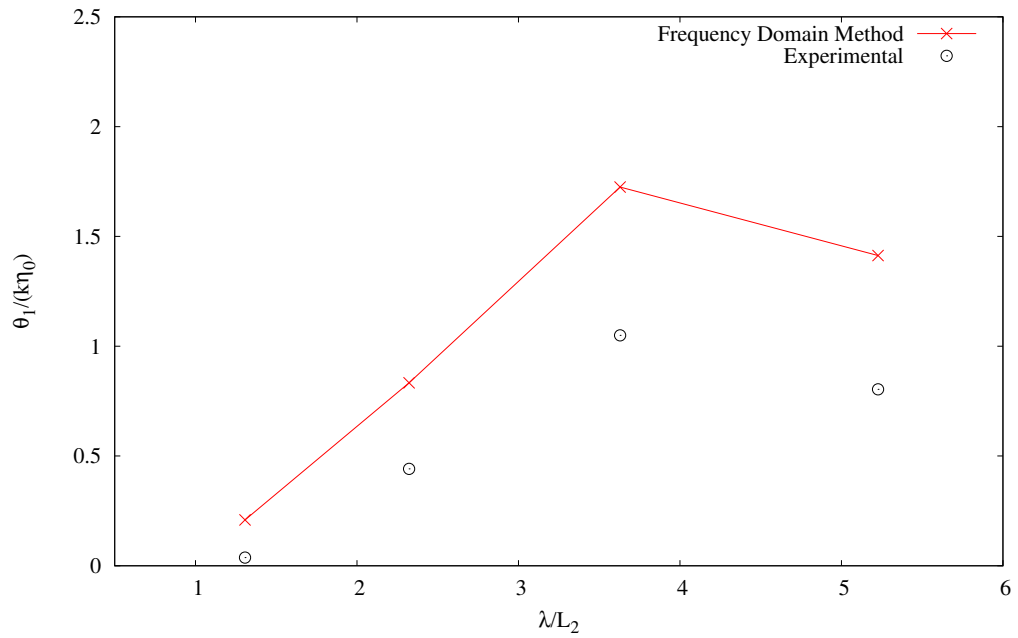


Figure 4.3: Non-dimensional Relative Pitch Angles at PTO-1

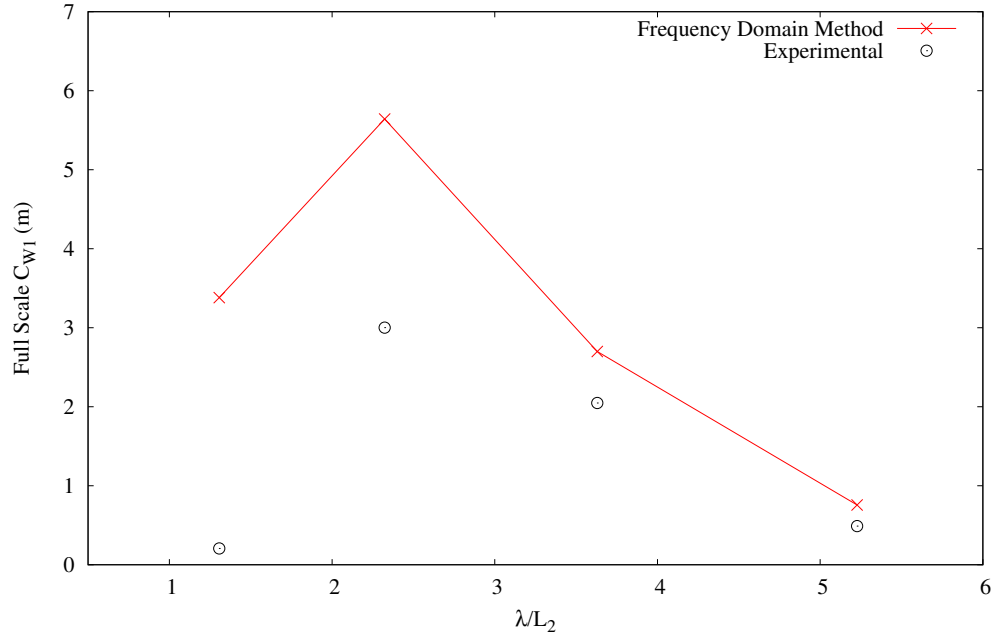


Figure 4.4: Full-scale Capture Width at PTO-1

#### 4.2.2 Second Generation SeaWEED Simulation

The numerical method is validated using the experimental results from the model tests on the second generation SeaWEED for both free hinge cases and damped cases. In addition, the numerical results are compared to those simulated using the time-domain program using linear Froude-Krylov forces. In the following, cases are defined by the combination of body-length and damper set-up, as detailed in Table 2.3 and Table 2.5. For example, T1-D2 denotes a case with body length, T1, and damper set-up, D2.

### 4.2.2.1 Free-hinged Conditions

Figs. 4.5 and 4.6 present the comparisons of the non-dimensional relative pitch angles at PTO-1 and PTO-2 for Case T1-D0 (see Table 2.4) in terms of the wave length to body length ratio, i.e.,  $\lambda/L_2$ , where  $\lambda$  is the wave length and  $L_2$  is the length of Body 2, which is constant in all the combinations of truss lengths (see Table 2.3). The relative pitch angle,  $\theta$ , is non-dimensionalized as  $\frac{\theta}{k\eta_0}$ , where  $k$  is the wave number and  $\eta_0$  is the amplitude of incident waves.

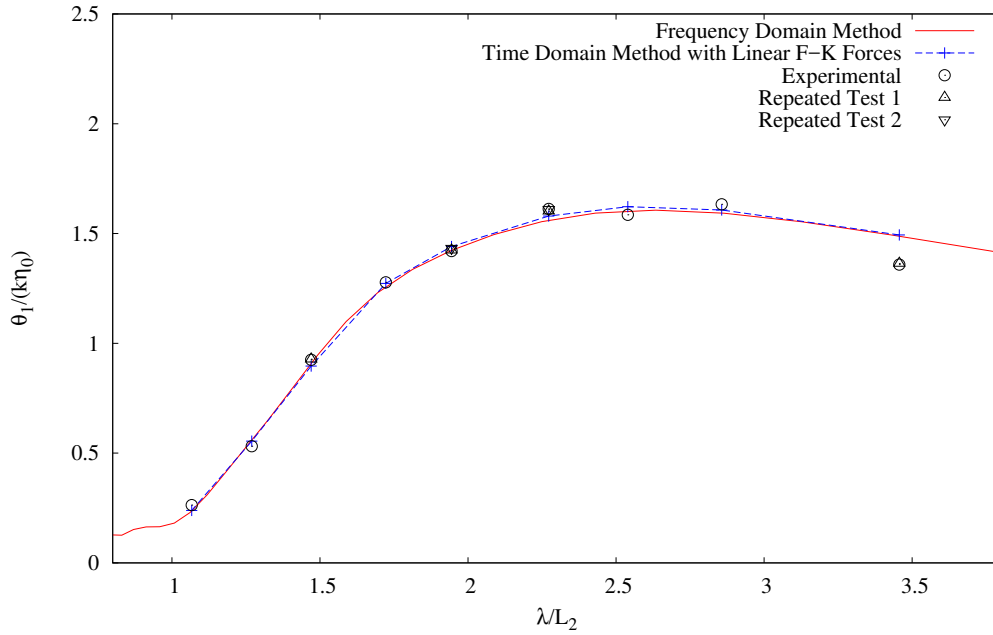


Figure 4.5: Non-dimensional Relative Pitch Angles at PTO-1 (Case T1-D0)

The results for Cases T2-D0, T3-D0 and T4-D0 are presented in Figs. 4.7, 4.8, 4.9, 4.10, 4.11 and 4.12.

As linear F-K forces are used in the time-domain simulations, the frequency-

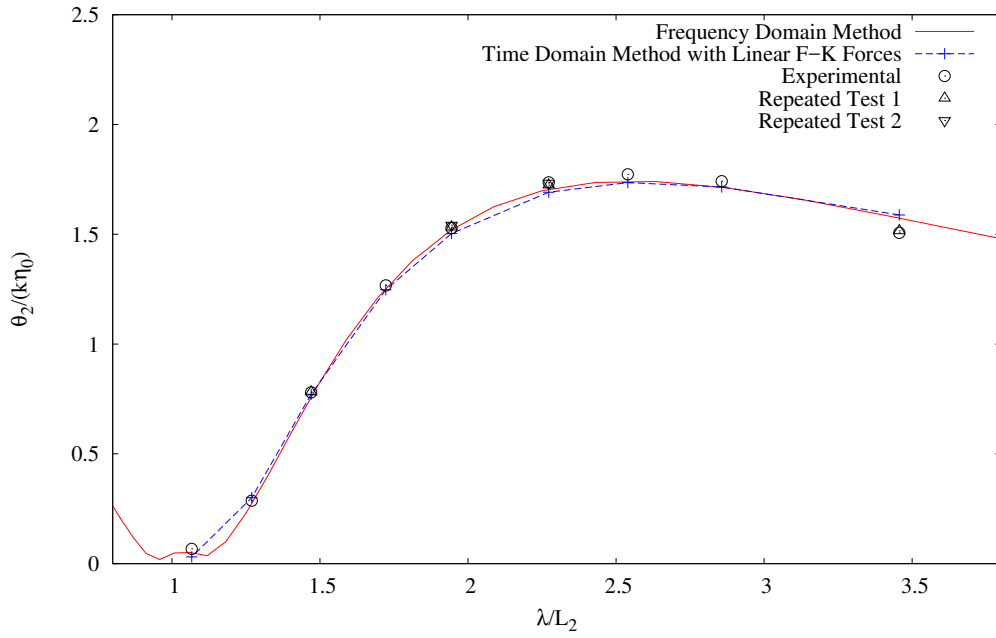


Figure 4.6: Non-dimensional Relative Pitch Angles at PTO-2 (Case T1-D0)

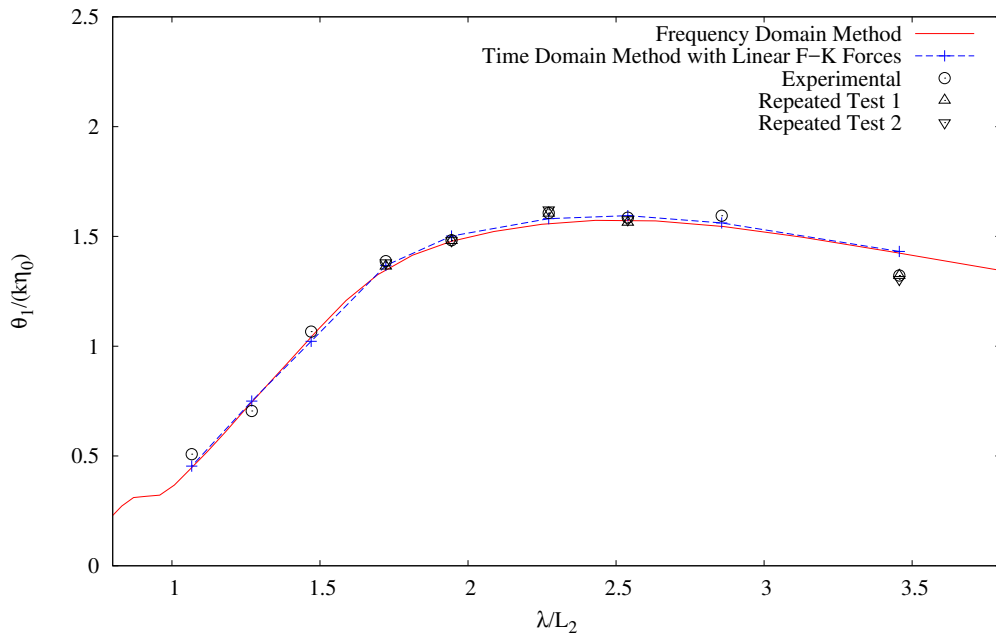


Figure 4.7: Non-dimensional Relative Pitch Angles at PTO-1 (Case T2-D0)

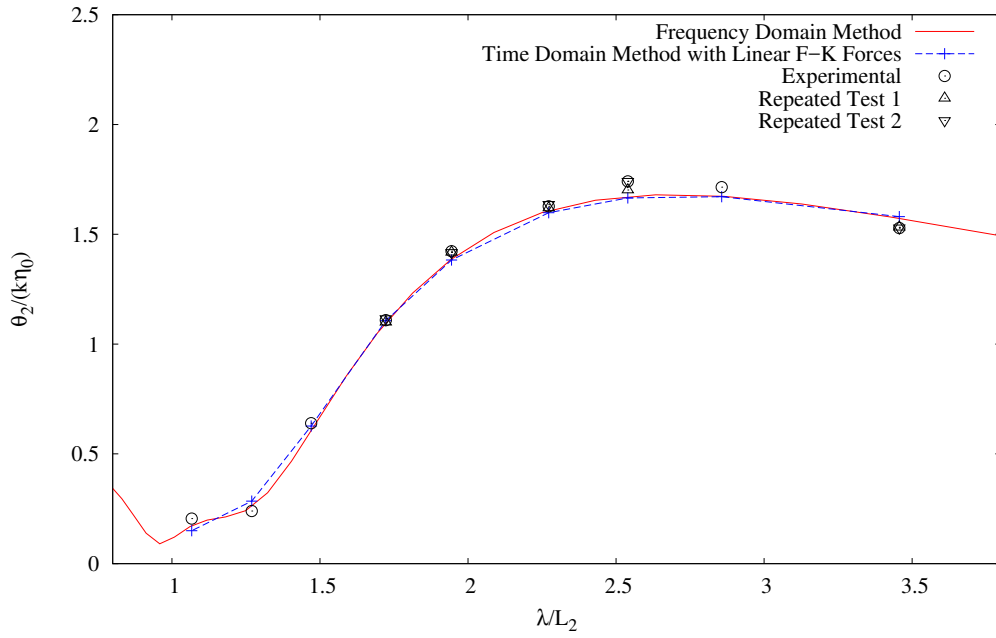


Figure 4.8: Non-dimensional Relative Pitch Angles at PTO-2 (Case T2-D0)

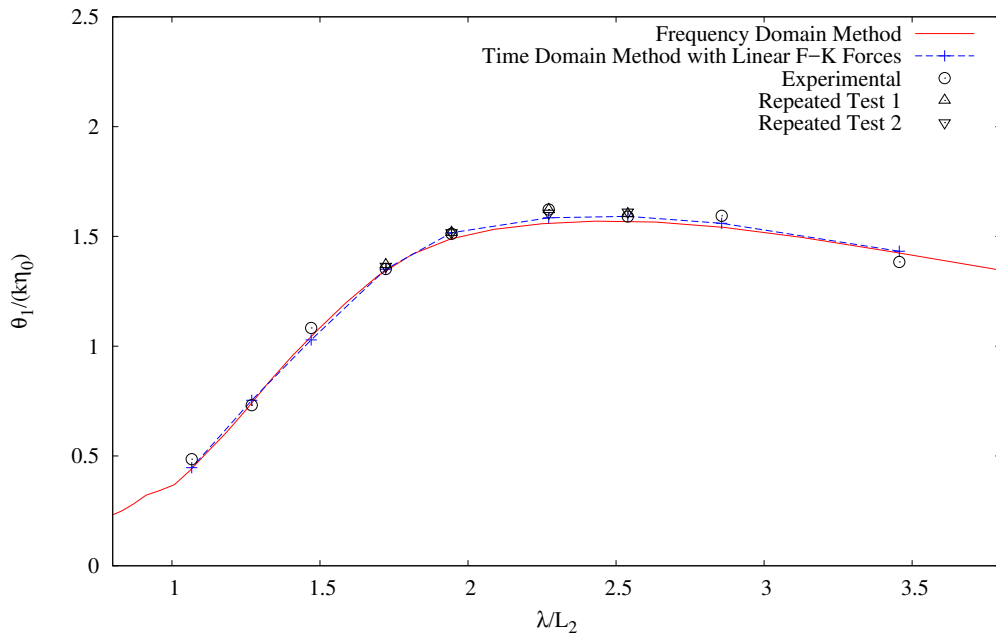


Figure 4.9: Non-dimensional Relative Pitch Angles at PTO-1 (Case T3-D0)

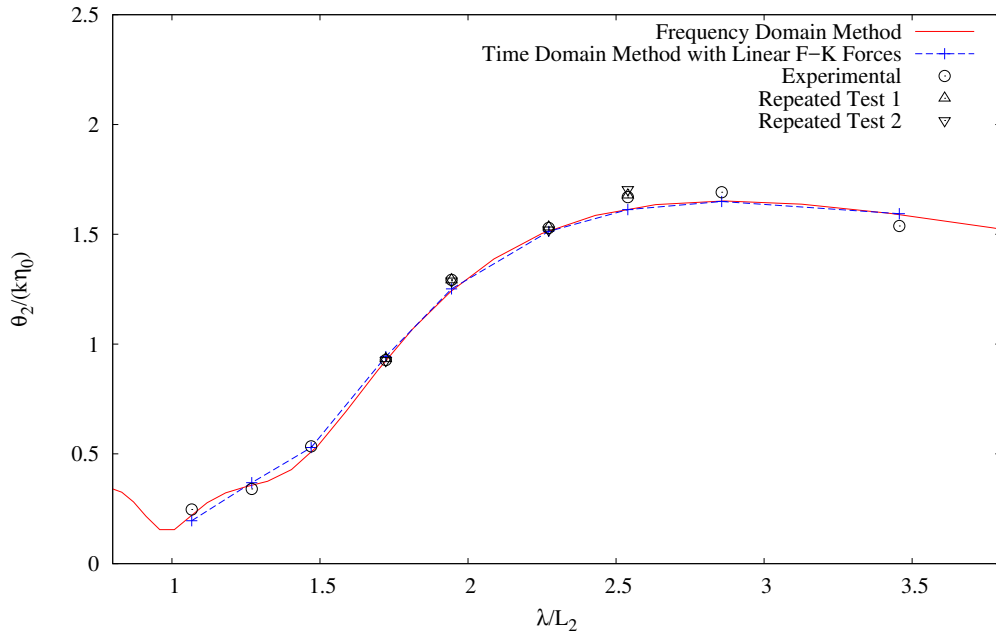


Figure 4.10: Non-dimensional Relative Pitch Angles at PTO-2 (Case T3-D0)

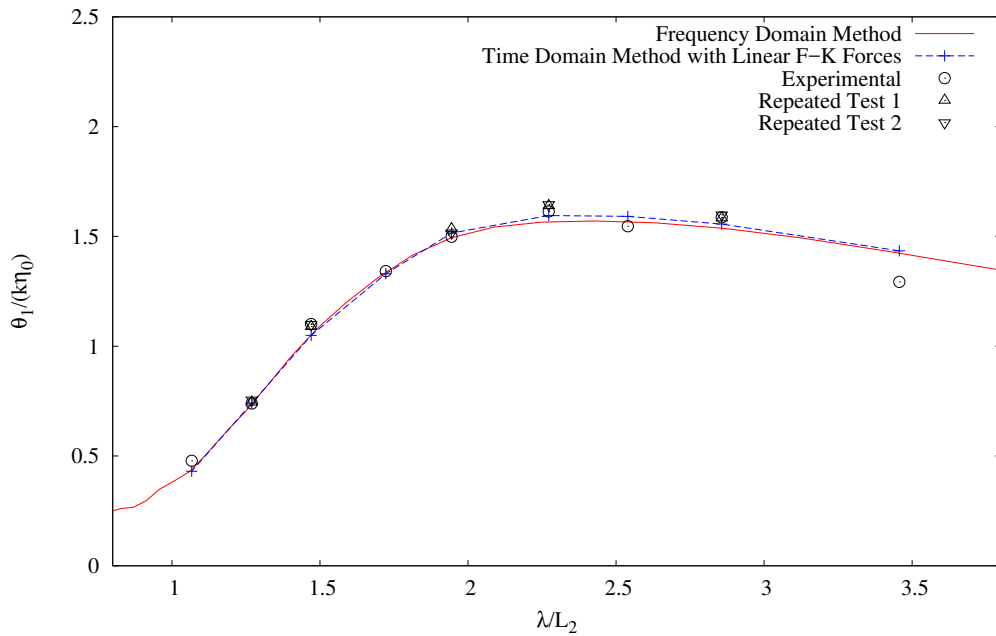


Figure 4.11: Non-dimensional Relative Pitch Angles at PTO-1 (Case T4-D0)

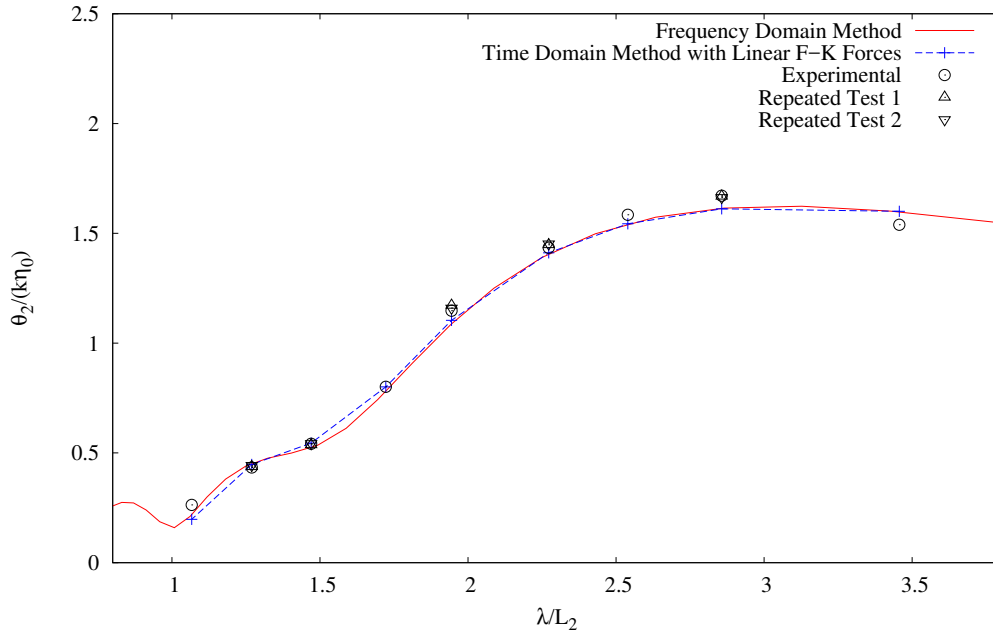


Figure 4.12: Non-dimensional Relative Pitch Angles at PTO-2 (Case T4-D0)

domain results are almost identical to the time-domain ones. Comparing the numerical results to the experimental ones, very good agreement is achieved for cases without PTOs.

#### 4.2.2.2 Damped Conditions

Tests on different damped set-ups (see Table 2.5) were conducted using Body Length Combination Case T1, as detailed in Table 2.3. Fig. 4.13 and 4.14 present the non-dimensional relative pitch angles, and Fig. 4.15 and 4.16 show the corresponding capture widths by PTO-1 and PTO-2 for Case T1-D1.

For the damping Case T1-D2, Figs. 4.17, 4.18, 4.19 and 4.20 show the non-dimensional relative pitch angles and the full scale capture widths of PTO-1 and PTO-2, respectively.

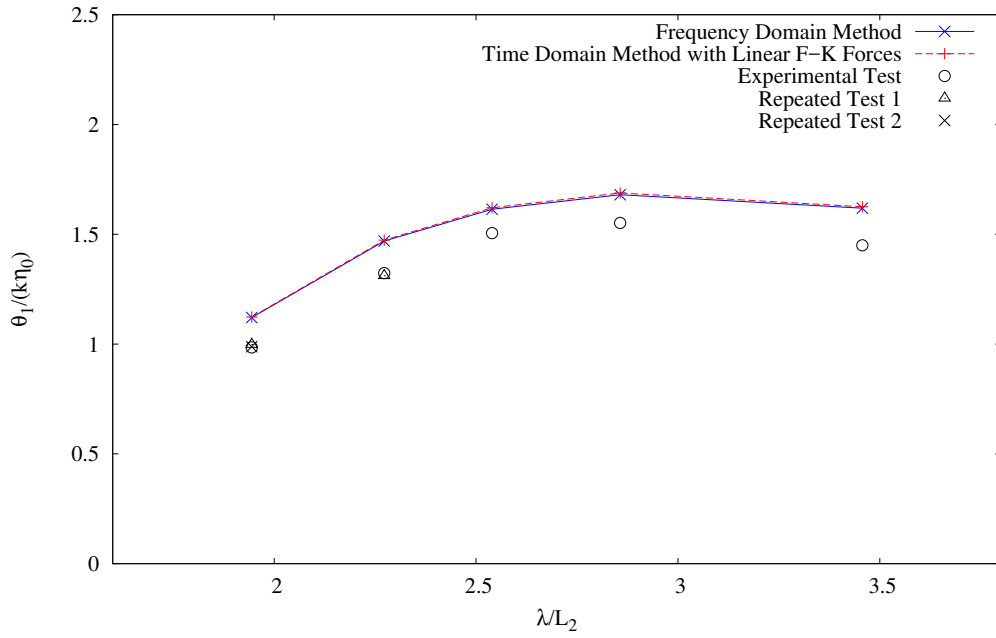


Figure 4.13: Non-dimensional Relative Pitch Angles at PTO-1 (Case T1-D1)

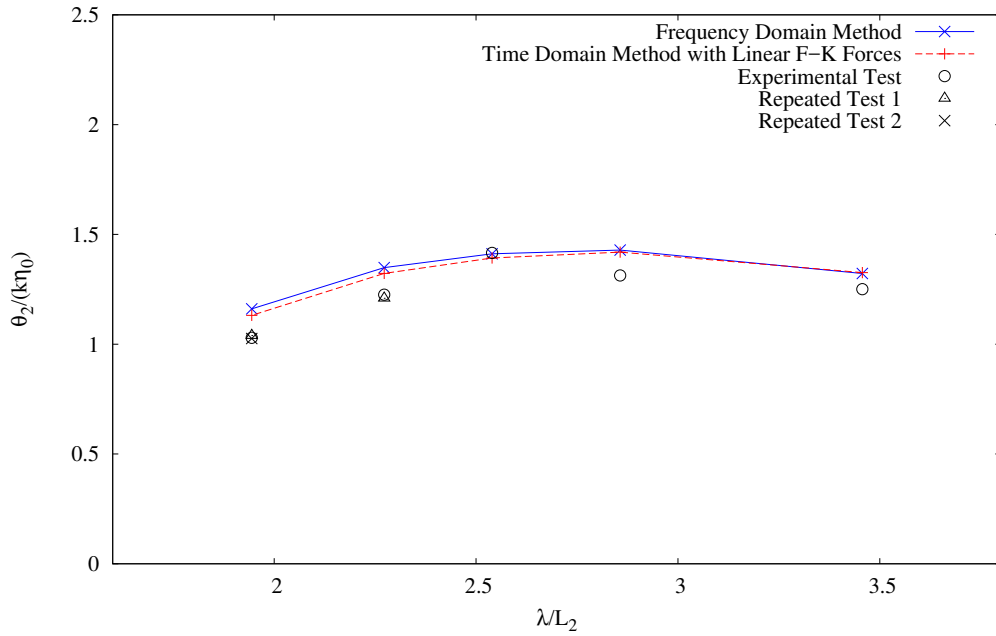


Figure 4.14: Non-dimensional Relative Pitch Angles at PTO-2 (Case T1-D1)

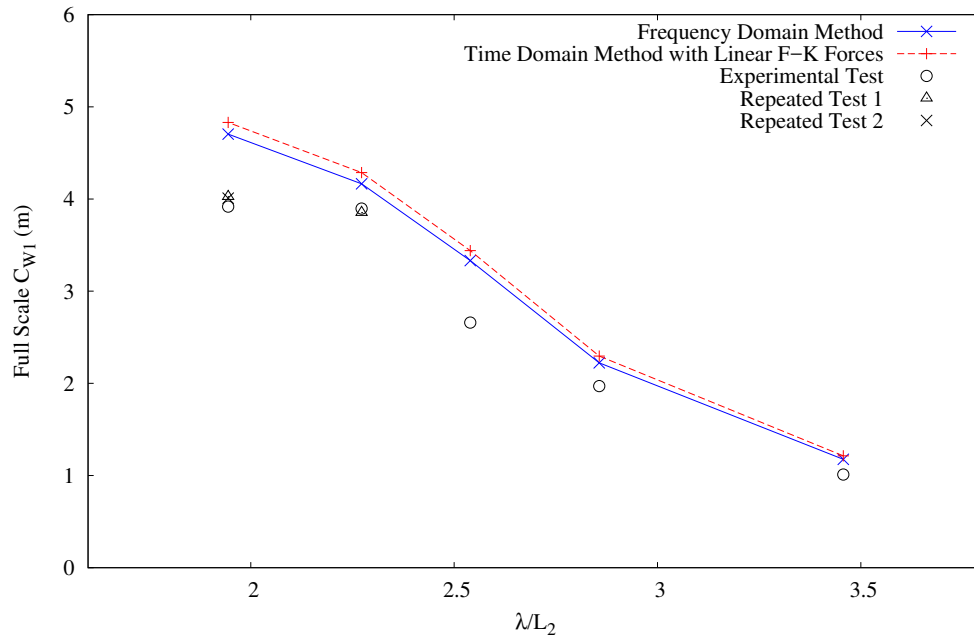


Figure 4.15: Full-scale Capture Width at PTO-1 (Case T1-D1)

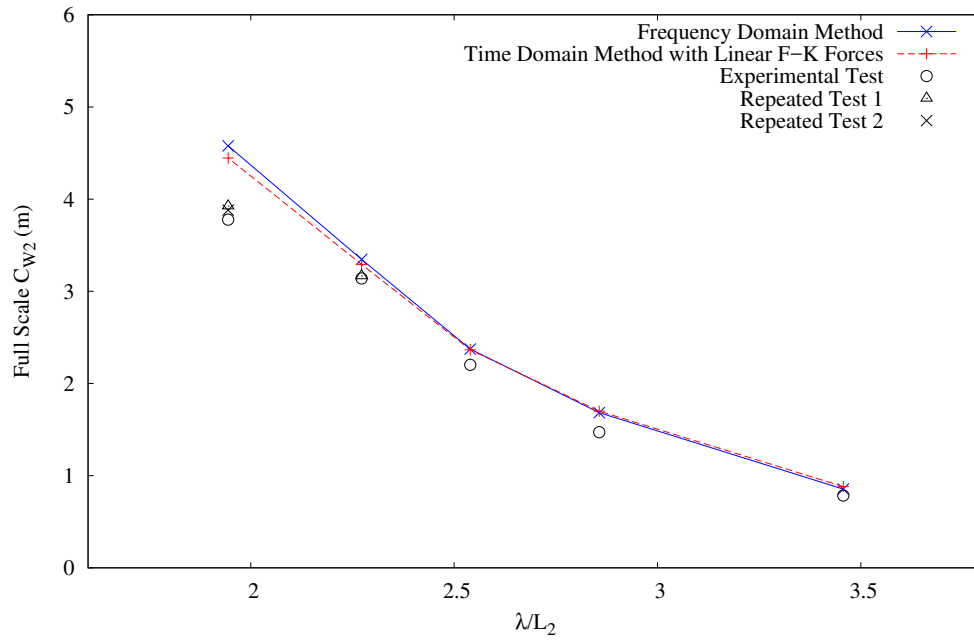


Figure 4.16: Full-scale Capture Width at PTO-2 (Case T1-D1)

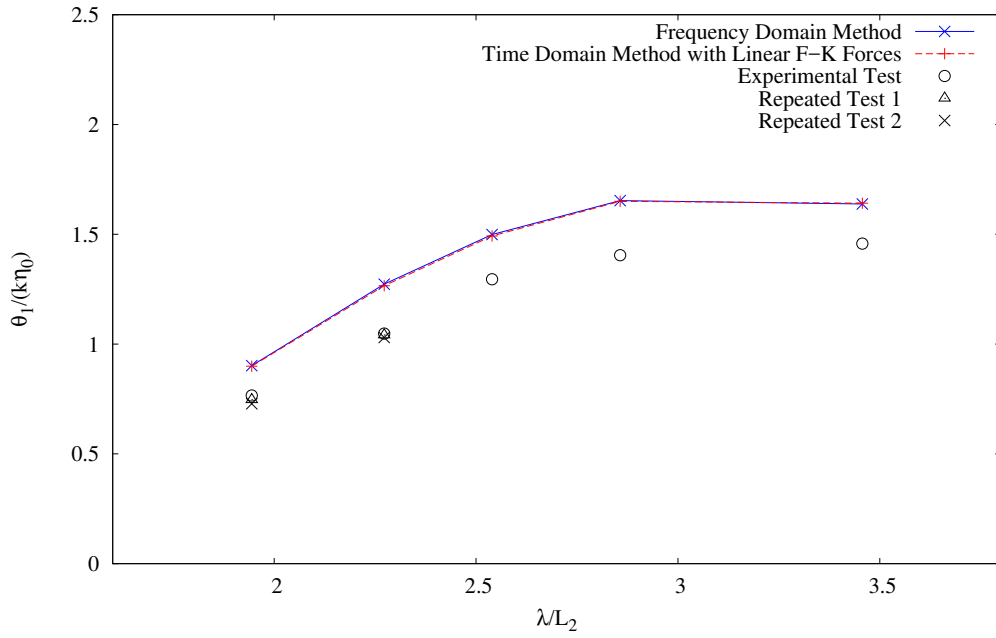


Figure 4.17: Non-dimensional Relative Pitch Angles at PTO-1 (Case T1-D2)

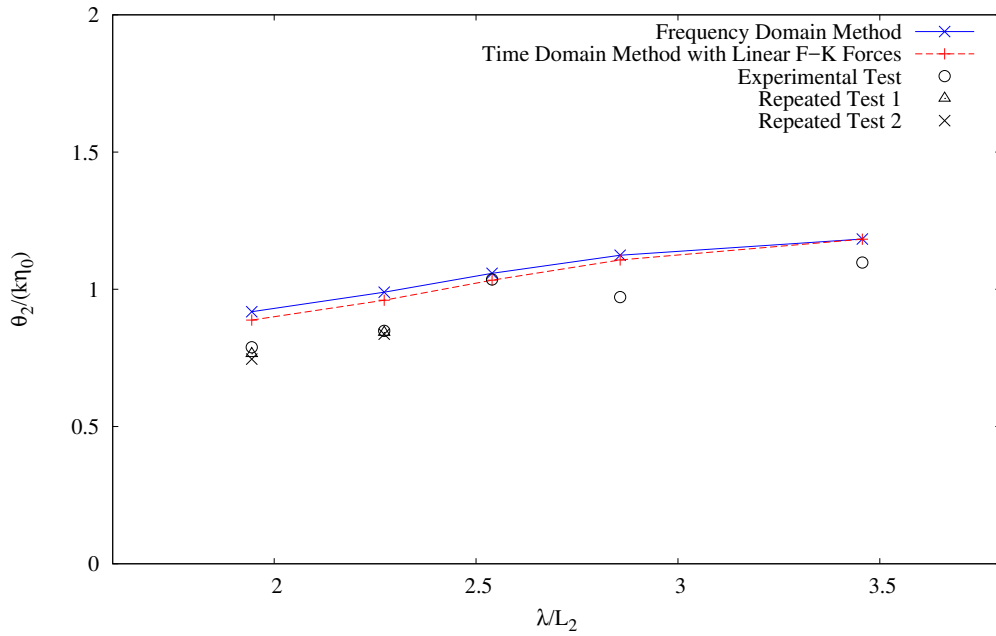


Figure 4.18: Non-dimensional Relative Pitch Angles at PTO-2 (Case T1-D2)

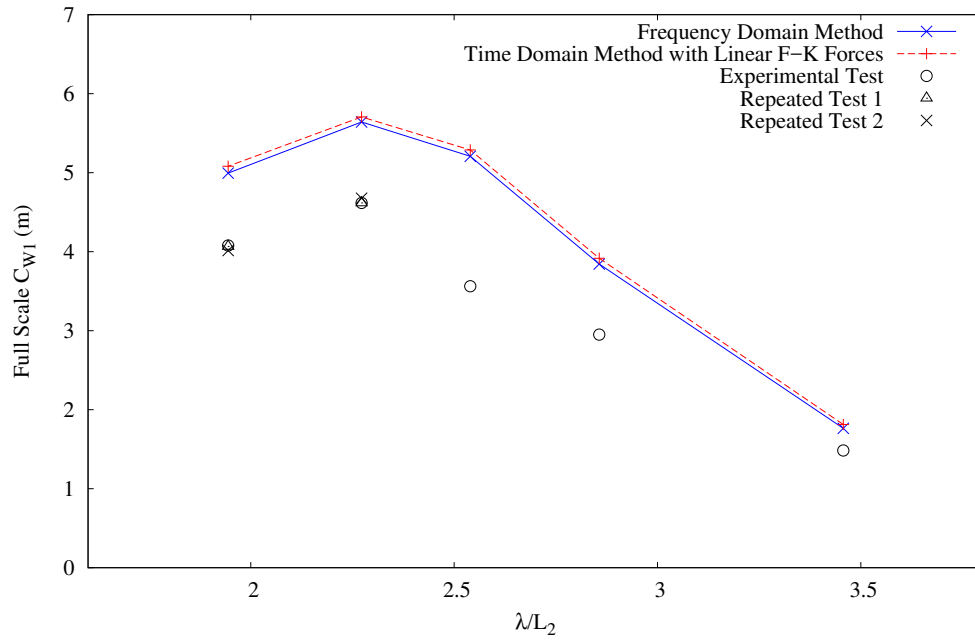


Figure 4.19: Full-scale Capture Width at PTO-1 (Case T1-D2)

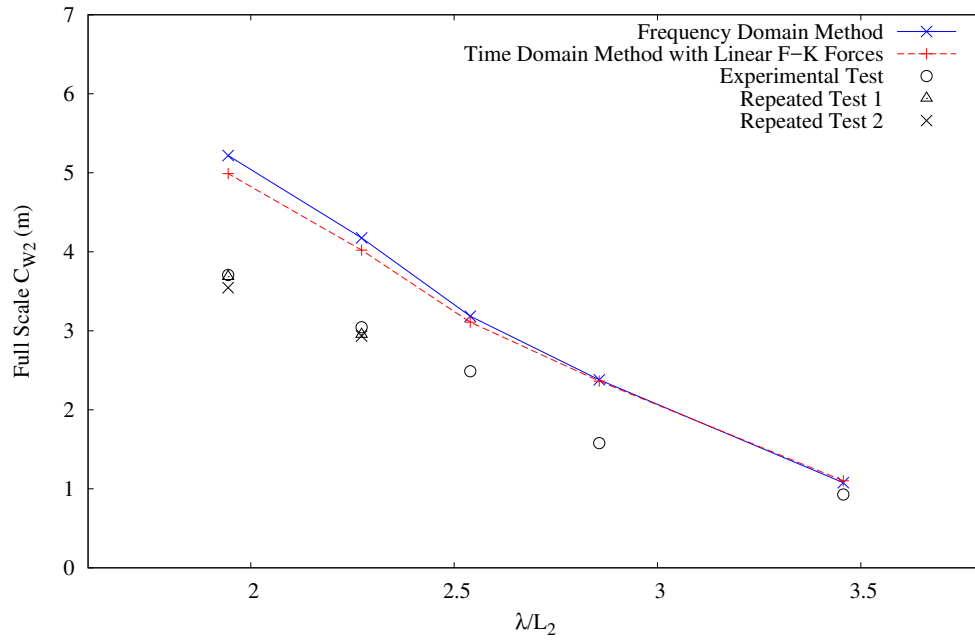


Figure 4.20: Full-scale Capture Width at PTO-2 (Case T1-D2)

For validation purposes, two additional sets of tests were conducted by activating PTO-1 and PTO-2 separately under the same damper set-up as Case T1-D2. Figs. 4.21, 4.22 and 4.23 present the relative pitch angles and capture widths for Case T1-D3 with only PTO-1 activated.

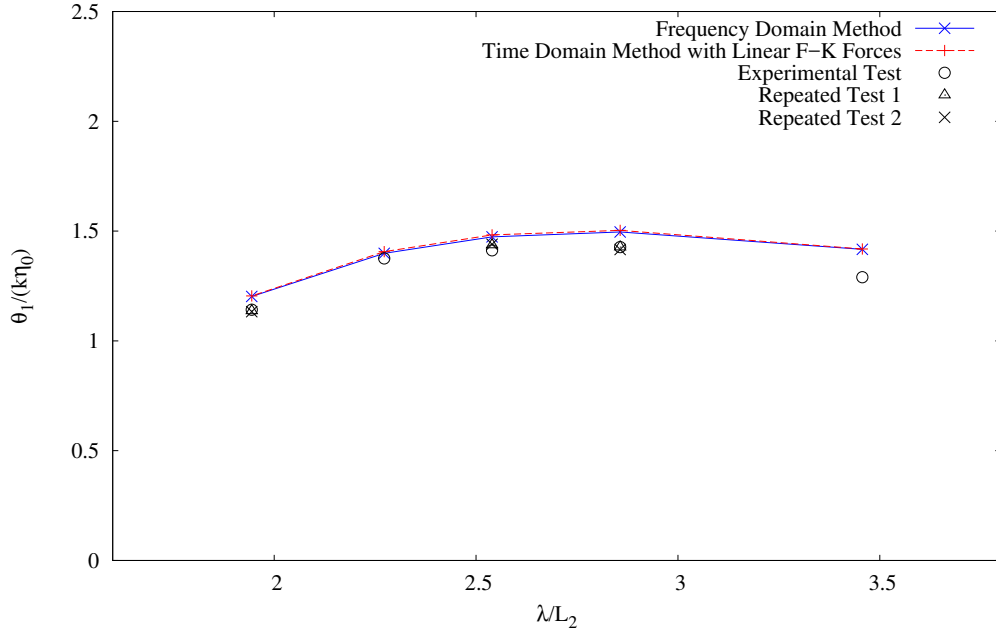


Figure 4.21: Non-dimensional Relative Pitch Angles at PTO-1 (Case T1-D3)

Figs. 4.24, 4.25 and 4.26 show the relative pitch angles and capture widths for Case T1-D4 with only PTO-2 activated.

Further increasing the damping, the responses of the PTOs were suppressed. The relative pitch angles and capture widths for Case T1-D5 are presented in Figs. 4.27, 4.28, 4.29 and 4.30.

To summarize, both frequency-domain and time-domain results agree well with the experimental data. For the damping tests, both relative pitch angles and capture

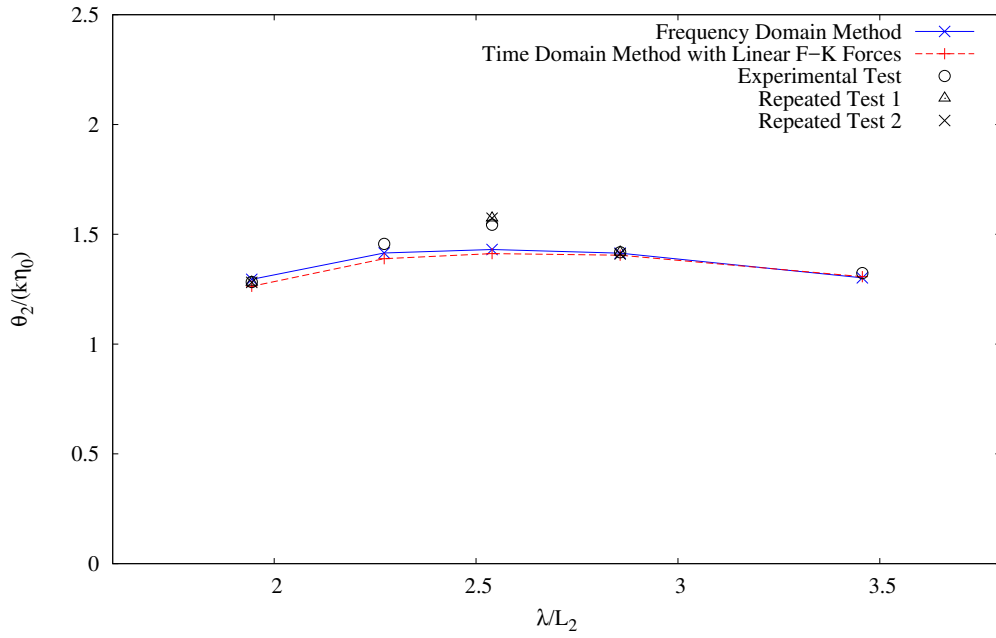


Figure 4.22: Non-dimensional Relative Pitch Angles at PTO-2 (Case T1-D3)

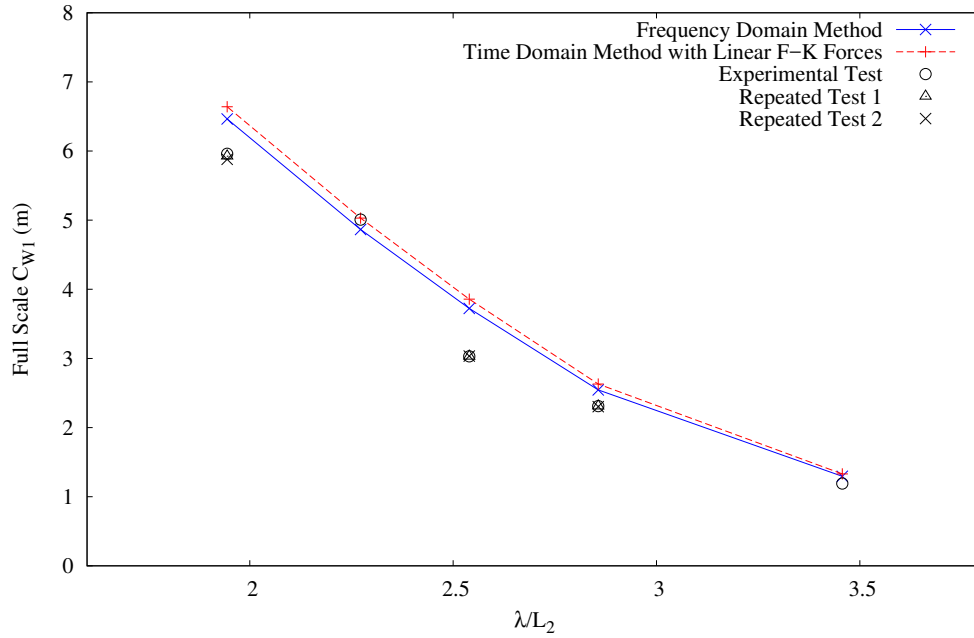


Figure 4.23: Full-scale Capture Width at PTO-1 (Case T1-D3)

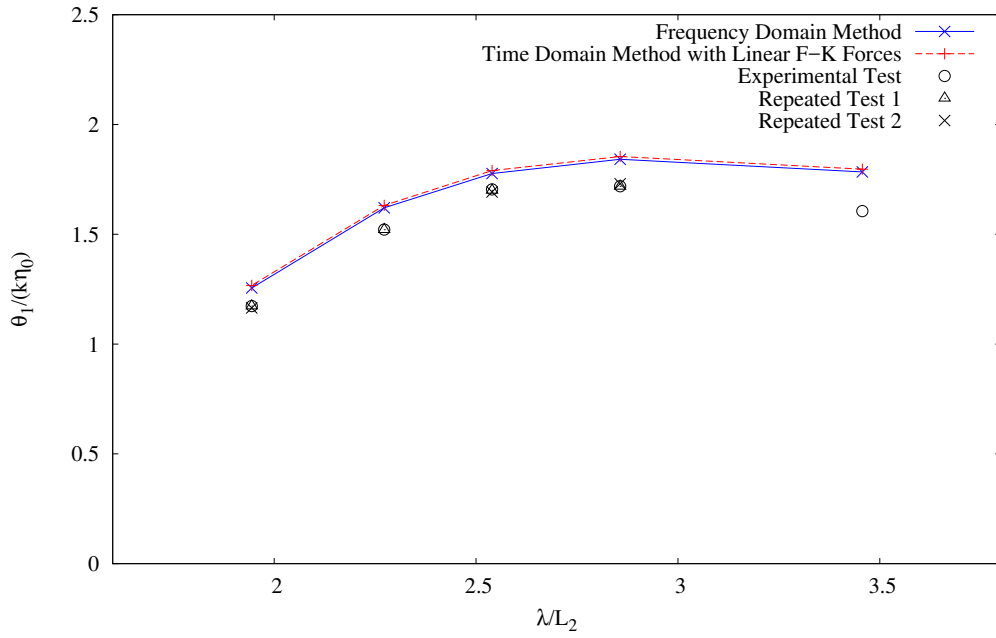


Figure 4.24: Non-dimensional Relative Pitch Angles at PTO-1 (Case T1-D4)

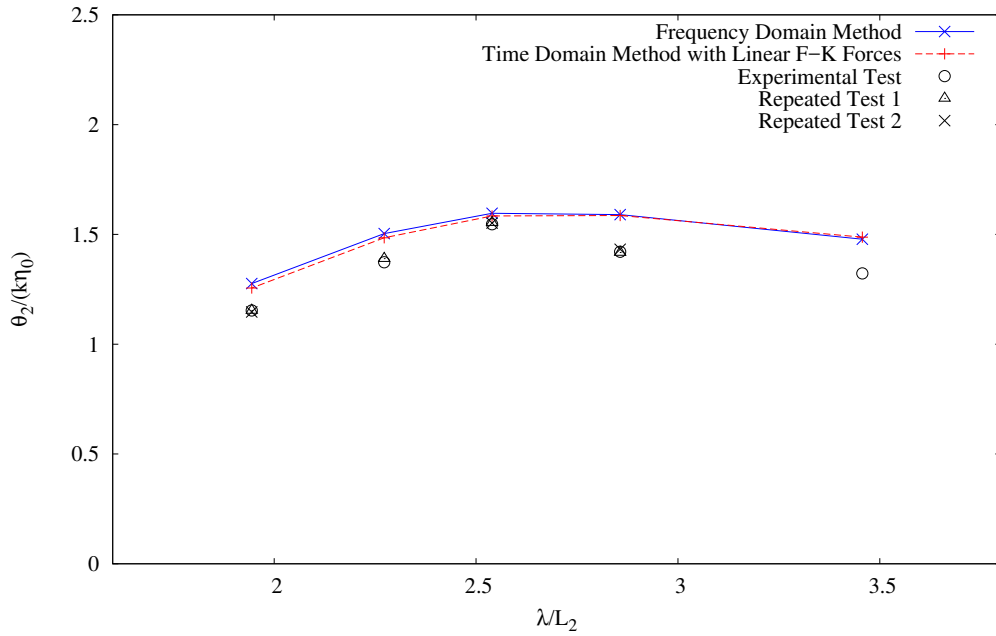


Figure 4.25: Non-dimensional Relative Pitch Angles at PTO-2 (Case T1-D4)

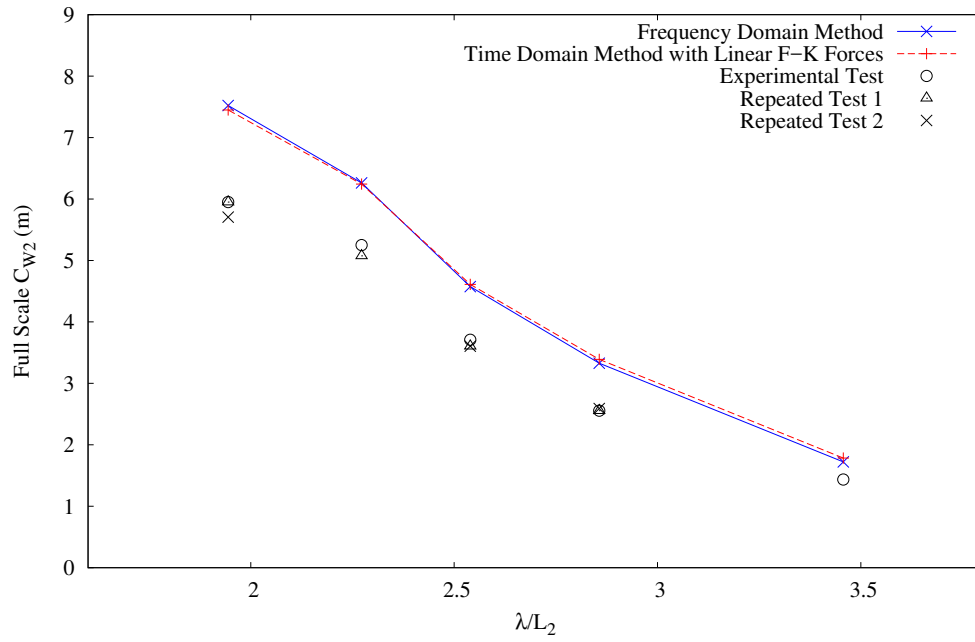


Figure 4.26: Full-scale Capture Width at PTO-2 (Case T1-D4)

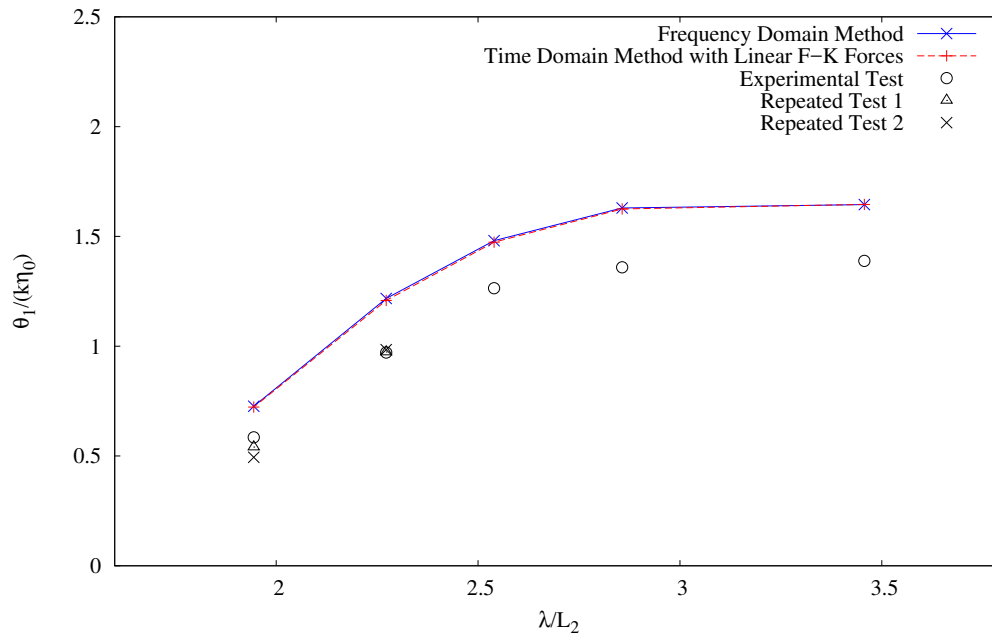


Figure 4.27: Non-dimensional Relative Pitch Angles at PTO-1 (Case T1-D5)

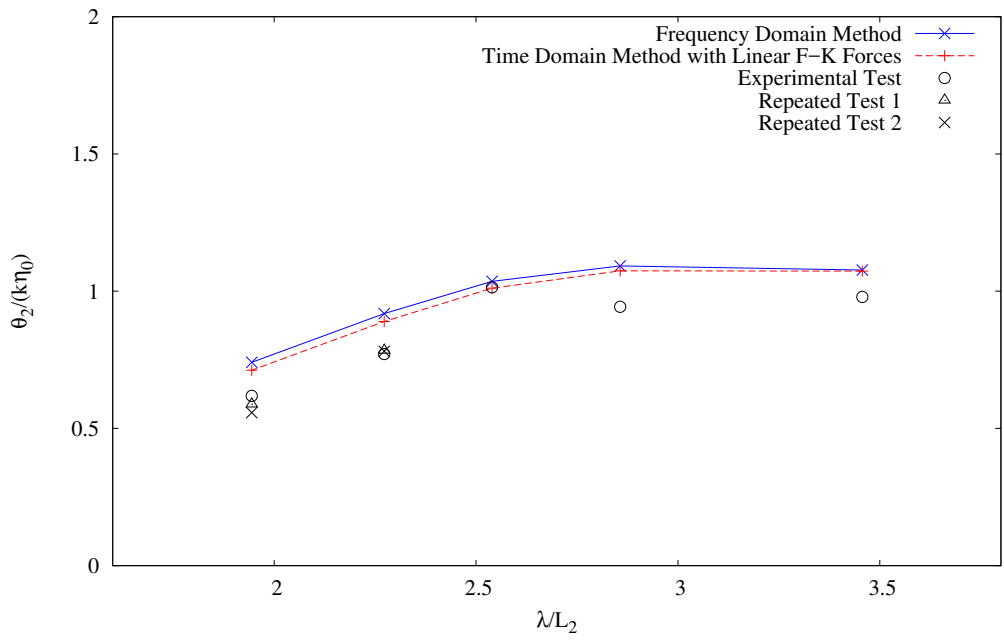


Figure 4.28: Non-dimensional Relative Pitch Angles at PTO-2 (Case T1-D5)

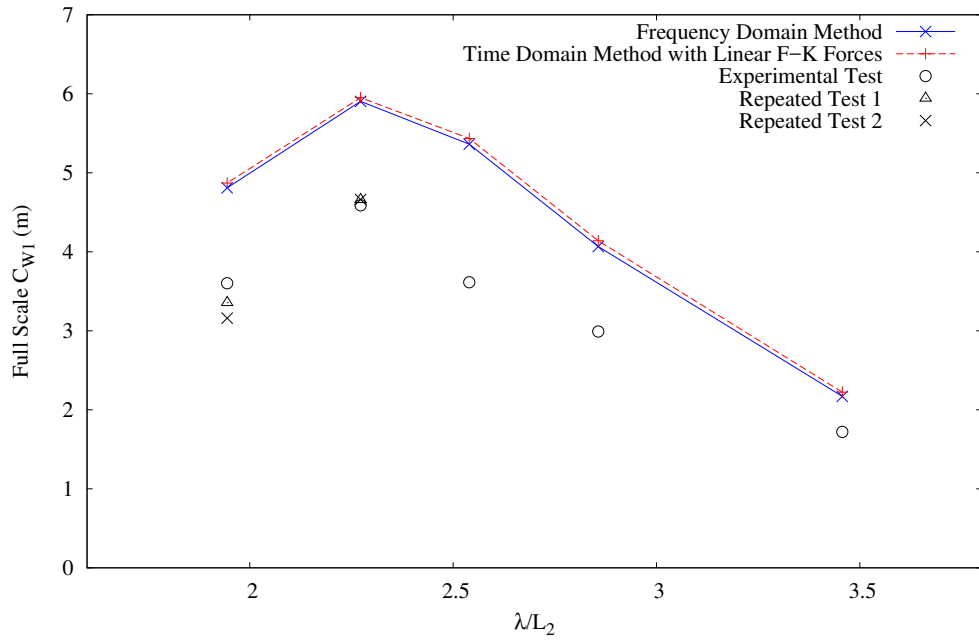


Figure 4.29: Full-scale Capture Width at PTO-1 (Case T1-D5)

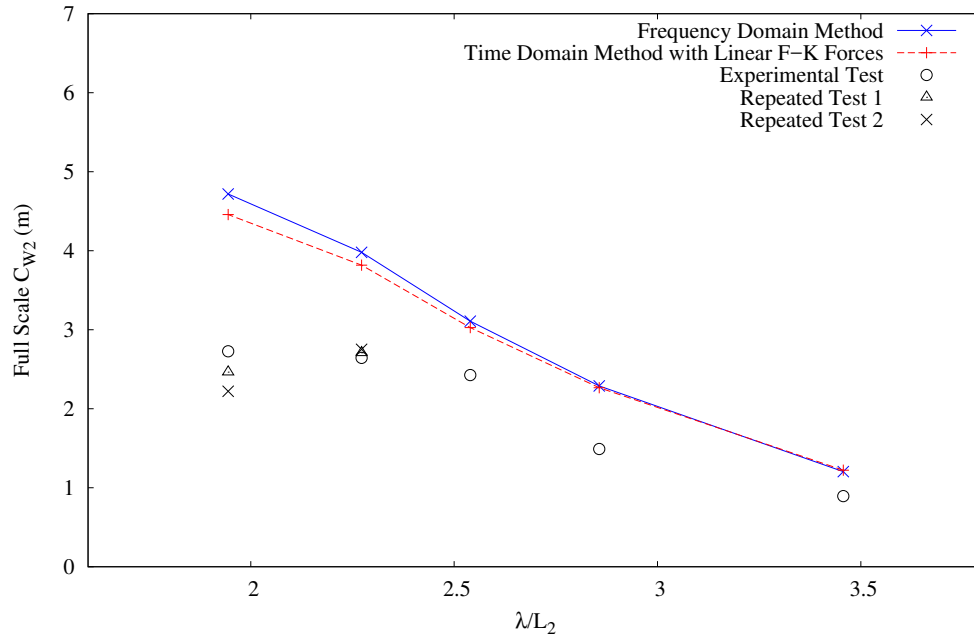


Figure 4.30: Full-scale Capture Width at PTO-2 (Case T1-D5)

width were slightly over-predicted by the present numerical method. As mentioned in the previous chapter, this is reasonable since the power extracted from the PTOs was not fully captured by the measuring system. The energy loss could be caused by the friction in the apparatus, the slight looseness between the connection parts and the measuring systems. The overall agreement between the experimental and numerical results of the free hinge and damped hinge tests is achieved. Therefore the numerical method can be further used for optimization studies.

## Chapter 5

# Optimization of the Second Generation of SeaWEED

In this chapter, optimization of the annual power absorption by SeaWEED in a particular area is studied. The design variables and the design domain are first identified. The Uniform design method is then applied to select the sample points from the geometrical design space. For each geometrical combination, the optimized damping coefficients and power absorption are determined applying the full factorial design method. The surrogate model is constructed by using the response surface method. Effects on the accuracy of the surrogate modeling by the number of sampling points and levels on the design space are investigated. After the surrogate model is verified, the desirability optimization method is used to find the optimal annual power absorption.

## 5.1 Optimization Problem

SeaWEED can be customized to operate in any intended locations with optimum efficiency, multiple design variables, including the truss lengths, drafts and damping of the WEC, were considered in the optimization. The mathematical formulation of the optimization problem is

$$\text{Maximize}[P_S^A(L_{T1}, L_{T2}, L_{T3}, D, d_1, d_2)] \quad (5.1)$$

where the objective function,  $P_S^A$ , is the annual power absorption of SeaWEED at an intended operation site, and the design variables include truss structure lengths of the three body segments,  $L_{T1}$ ,  $L_{T2}$ , and  $L_{T3}$ , as shown in Fig. 2.8, draft of the device,  $D$ , and damping coefficients at PTO-1 and PTO-2,  $d_1$  and  $d_2$ , respectively.

## 5.2 Selection of Sample Points

To determine the sample points for geometrical variables, the uniform design method (Fang et al., 2000) is utilized, which is categorized as a space-filling design. A brief overview of the application of the method is presented below. More details on the method can be found in the work of Fang et al. (2005).

Based on the good lattice point method proposed by Korobov (Niederreiter, 1978), a uniform design (UD) table is generated according to the number of sample points,  $n$ , to be selected (Fang et al., 2005). The UD table consists of  $n$  rows and  $s$  columns. In a design with  $v$  design variables and  $n$  sampling points,  $v$  out of  $s$  UD table columns are selected. For each sampling point, the locations of the  $v$  design variables

in the design domains are selected according to the index  $u$  in the selected columns. However, there are  $C_s^v$  choices, a selection criterion is thus needed. It is desirable that the resulting sampling points are uniformly distributed on the design domain. To evaluate the uniformity of the sampling, the centered  $L_2$ -discrepancy,  $CD$ , should be calculated as (Fang et al., 2005)

$$CD^2 = \frac{13^v}{12} - \frac{2}{n} \sum_{k=1}^n \prod_{j=1}^v [1 + \frac{1}{2}|x_{kj} - 0.5| - \frac{1}{2}|x_{kj} - 0.5|^2] + \frac{1}{n^2} \sum_{k=1}^n \sum_{j=1}^n \prod_{i=1}^v [1 + \frac{1}{2}|x_{ki} - 0.5| + \frac{1}{2}|x_{ji} - 0.5| - \frac{1}{2}|x_{ki} - x_{ji}|] \quad (5.2)$$

where  $x$  is the normalized form of  $u$  in the UD table, given as  $x = \frac{2u-1}{2n}$ . The lower the  $CD$  value is, the more uniform the design will be.

### 5.3 Surrogate Model Construction

Response Surface Methodology (RSM) consists of a group of mathematical and statistical techniques that can be utilized to find an empirical model to describe the relationship between the input variables and the responses (Myers et al., 1995).

An experimental optimization procedure by utilizing the RSM has the following steps (Baş et al., 2007). (1) Determine the experimental region, the independent input variables, and the level of each variable. (2) Select the experimental design method, generate the experimental matrix (choose the sampling points), and carry out the experiment. (3) Find a polynomial function to predict the experiment and verify the function. (4) Generate the response surface and the contour plots, and search the optimum values.

Polynomial functions, obtained from experiments or numerical simulations, are

used to approximate responses. From the polynomial functions, the target points, such as maximum or minimum values of a response, can be determined.

When constructing the surrogate, the adjusted R-squared value based on the sampling points should be checked. Further, to validate the regression model,  $0.25 \times$  the total number of sample points, as suggested by Forrester et al. (2008), located within the search domains but different from the sample points, should be selected to compute the errors,  $E$ , between the results obtained from direct numerical simulation and the surrogate model fitting.

$$E = \left| \frac{P_{SIM} - P_{RSM}}{P_{SIM}} \right| \times 100\% \quad (5.3)$$

where  $P_{RSM}$  is the power obtained from the response surface and  $P_{SIM}$  is the power directly calculated from simulation, respectively.

## 5.4 Optimal Response Exploration

After the surrogate model is validated, the desirability optimization methodology (Derringer et al., 1980) can be utilized to search the optimal responses. This method is based on a modified desirability function and useful in optimizing multiple response variables (Li et al., 2017).

For each response,  $Y_i(x)$ , a desirability function  $d_i(Y_i)$  ranges between zero and one can be determined. A desirability of zero represents a completely undesirable value of  $Y_i$ ; while a desirability of one means a completely desirable or ideal response value.

Different desirability functions  $d_i(Y_i)$  can be used, depending on whether a particular response  $Y_i$  is to be maximized, minimized, or assigned a target value. Der-

ringer and Suich (1980) proposed a set of desirability functions. Let  $L_i$ ,  $U_i$  and  $T_i$  ( $L_i \leq T_i \leq U_i$ ) be the lower, upper, and target values, respectively, that are desired for response  $Y_i$ .

To maximize the response, the desirability is expressed as

$$d_i(\hat{Y}_i) = \begin{cases} 0 & \text{if } \hat{Y}_i(x) < L_i \\ \left(\frac{\hat{Y}_i(x)-L_i}{T_i-L_i}\right)^s & \text{if } L_i \leq \hat{Y}_i(x) \leq T_i \\ 1.0 & \text{if } \hat{Y}_i(x) > T_i \end{cases} \quad (5.4)$$

where  $T_i$  is a large enough value for the response and  $s$  is the weight, which determines how important it is to hit the maximum value.

To minimize the response, the desirability is defined as

$$d_i(\hat{Y}_i) = \begin{cases} 1.0 & \text{if } \hat{Y}_i(x) < T_i \\ \left(\frac{\hat{Y}_i(x)-U_i}{T_i-U_i}\right)^s & \text{if } T_i \leq \hat{Y}_i(x) \leq U_i \\ 0 & \text{if } \hat{Y}_i(x) > U_i \end{cases} \quad (5.5)$$

where  $T_i$  is a small enough value for the response.

If the response is to achieve a target value, the desirability function is

$$d_i(\hat{Y}_i) = \begin{cases} 0 & \text{if } \hat{Y}_i(x) < L_i \\ \left(\frac{\hat{Y}_i(x)-L_i}{T_i-L_i}\right)^s & \text{if } L_i \leq \hat{Y}_i(x) \leq T_i \\ \left(\frac{\hat{Y}_i(x)-U_i}{T_i-U_i}\right)^t & \text{if } T_i \leq \hat{Y}_i(x) \leq U_i \\ 0 & \text{if } \hat{Y}_i(x) > U_i \end{cases} \quad (5.6)$$

where  $t$  is also a weight that attributes levels of importance to the target value.

Based on the problem of interest, the individual desirability functions can be combined using the geometric mean, resulting the overall desirability,  $D$

$$D = [d_1(Y_1)d_2(Y_2) \cdots d_k(Y_k)]^{1/k} \quad (5.7)$$

where  $k$  is the number of responses.

The maximum value of the overall desirability function,  $D$ , can then be searched to achieve the optimal responses. For problems with only one response, the overall desirability function,  $D$ , is the individual one.

## 5.5 Optimization of SeaWEED

### 5.5.1 Optimization Problem Definition

In the present work, the wave climate off the Cork Harbour in Ireland is considered, and the JONSWAP spectrum (Hasselmann, 1973) is applied. The wave climate table is generated from the percentage of the occurrence hours in the data base (SmartBay, 2015), as shown in Fig. 5.1.

Probability of Occurrence	Tp (s)													
	4.5	5.5	6.5	7.5	8.5	9.5	10.5	11.5	12.5	13.5	14.5	15.5	16.5	
Hs(m)	0.25	0.03%	0.01%	0.00%	0.01%	0.00%	0.00%	0.00%	0.00%	0.00%	0.00%	0.00%	0.00%	0.00%
	0.75	0.34%	1.26%	1.05%	0.72%	0.57%	0.70%	0.49%	0.47%	0.03%	0.16%	0.01%	0.02%	0.00%
	1.25	0.13%	2.17%	5.05%	5.49%	3.45%	2.37%	1.77%	1.60%	1.52%	0.92%	0.39%	0.08%	0.05%
	1.75	0.02%	0.38%	2.00%	4.61%	5.93%	3.86%	2.17%	1.89%	1.18%	0.82%	0.36%	0.18%	0.07%
	2.25	0.00%	0.03%	0.60%	1.58%	4.40%	4.62%	2.39%	1.29%	0.63%	0.38%	0.26%	0.05%	0.02%
	2.75	0.00%	0.00%	0.17%	0.61%	2.02%	3.98%	2.92%	1.14%	0.59%	0.22%	0.06%	0.03%	0.02%
	3.25	0.00%	0.00%	0.03%	0.32%	0.75%	1.90%	2.56%	1.16%	0.31%	0.18%	0.09%	0.03%	0.00%
	3.75	0.00%	0.00%	0.00%	0.15%	0.46%	1.05%	1.56%	0.99%	0.39%	0.13%	0.07%	0.01%	0.00%
	4.25	0.00%	0.00%	0.00%	0.03%	0.23%	0.34%	0.78%	0.69%	0.47%	0.17%	0.05%	0.00%	0.01%
	4.75	0.00%	0.00%	0.00%	0.01%	0.06%	0.16%	0.28%	0.33%	0.25%	0.08%	0.02%	0.02%	0.00%
	5.25	0.00%	0.00%	0.00%	0.00%	0.02%	0.09%	0.15%	0.09%	0.16%	0.06%	0.01%	0.00%	0.00%
	5.75	0.00%	0.00%	0.00%	0.00%	0.01%	0.02%	0.06%	0.03%	0.14%	0.09%	0.01%	0.00%	0.00%
	6.25	0.00%	0.00%	0.00%	0.00%	0.00%	0.00%	0.02%	0.00%	0.06%	0.06%	0.01%	0.00%	0.00%
	6.75	0.00%	0.00%	0.00%	0.00%	0.00%	0.00%	0.01%	0.00%	0.03%	0.01%	0.00%	0.00%	0.00%
7.25	0.00%	0.00%	0.00%	0.00%	0.00%	0.00%	0.00%	0.00%	0.01%	0.01%	0.00%	0.00%	0.00%	

Figure 5.1: Wave Climate Table off Cork Harbour in Ireland

The target is to optimize the annual power absorption of SeaWEED,  $P_S$  (see Eq.

(5.1)), for this operation site. The design domains of the design variables are listed in Table 5.1. The selection of levels of design variables will be discussed in the following context.

Table 5.1: Geometrical design variables (full-scale)

Variable	Lower Bound	Upper Bound
$L_{T1}(m)$	10.0	100.0
$L_{T2}(m)$	10.0	100.0
$L_{T3}(m)$	10.0	100.0
$D(m)$	1.0	4.0

The geometrical design variables,  $L_{T1}$ ,  $L_{T1}$ ,  $L_{T1}$  and  $D$ , and the damping design variables,  $d_1$  and  $d_2$ , are optimized in two stages. To determine the sample points for geometrical variables, the uniform design method (Fang et al., 2005) is utilized. For each sampling point, i.e. geometrical combination, the optimum damping coefficients,  $d_1$  and  $d_2$ , at the two PTOs and the annul power absorption,  $P_{Smax}^A(L_{T1}, L_{T2}, L_{T3}, D)$ , are determined using a full factorial design, as presented in Table 5.2.

Table 5.2: PTO damping coefficients (full-scale)

Variable	Upper Bound	Lower Bound	Level
$d_1(Nms)$	$8.8 \times 10^6$	$8.6 \times 10^8$	50
$d_2(Nms)$	$8.8 \times 10^6$	$8.6 \times 10^8$	50

The powers for all  $d_1$  and  $d_2$  combinations are computed using the frequency-domain program and the optimal combination with maximum power is determined. Fig. 5.2 presents an example for a case with  $L_{T1} = 10$  m,  $L_{T2} = 50$  m,  $L_{T3} = 20$  m, and  $D = 2.5$  m.

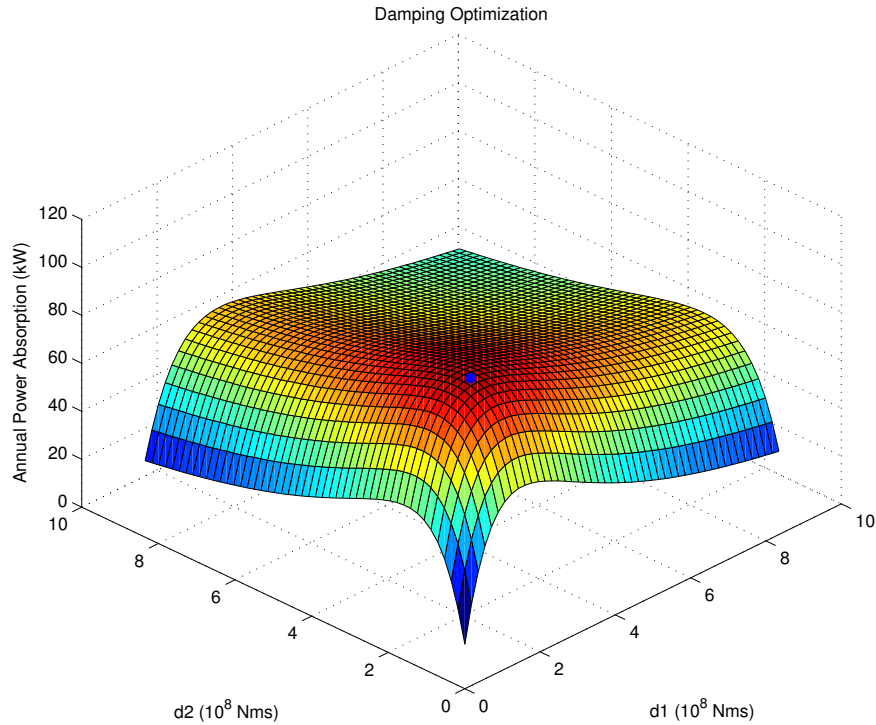


Figure 5.2: Damping Optimization

### 5.5.2 Selection of Sampling Points and Levels

Investigation on the levels of design variables and total number of sampling points were conducted. Three different level combinations (denoted as  $Level_1$ ,  $Level_2$  and  $Level_3$ , respectively) were used to discretize the design domains, as presented in Table

5.3, and 30, 60, and 100 sampling points were selected to check the quality of the surrogate model.

Table 5.3: Geometrical design variable level combination

Variable	$Level_1$	$Level_2$	$Level_3$
$L_{T1}$	3	5	10
$L_{T2}$	3	5	10
$L_{T3}$	3	5	10
$D$	3	5	5

As mentioned earlier, the centered  $L_2$ -discrepancy,  $CD$ , should be calculated to investigate the uniformity of sampling. The smaller the  $CD$  value, the more uniform the sampling points distribute on the design space. Table 5.4 presents the  $CD$  values using different number of sampling points.

Table 5.4:  $CD$  value

Number of Sampling Points	$CD$ Value
30	0.056
60	0.035
100	0.022

To investigate the level of design variables, regression models obtained using differ-

ent level combinations and sampling points were constructed and the corresponding adjusted R-squared values were calculated. As the adjusted R-squared value approaches one, the quality of the regression model increases. Usually, an adjusted R-squared value greater than 0.8 indicates a surrogate with good predictive capabilities (Forrester et al., 2008).

Figure 5.3 presents the power obtained from the response surface method and that by the direct computation with the frequency-domain method for different levels and numbers of sampling points combinations, and the corresponding adjusted R-squared values are listed in Table 5.5.

Table 5.5: Adjusted R-squared value

Number of Sampling Points	<i>Level</i> <sub>1</sub>	<i>Level</i> <sub>2</sub>	<i>Level</i> <sub>3</sub>
30	0.884	0.840	0.780
60	0.937	0.993	0.971
100	-	0.996	0.988

It can be seen that when the number of sampling points is greater than 60, the adjusted R-squared value is closer to one, indicating a better surrogate model. On the other hand, the levels of variables do not have significantly effect on the adjusted R-squared values.

Further, validations on the surrogate models were conducted. As mentioned earlier,  $0.25 \times$  the total number of sample points located within the search domains but different from the sample points were selected for each regression model, and the er-

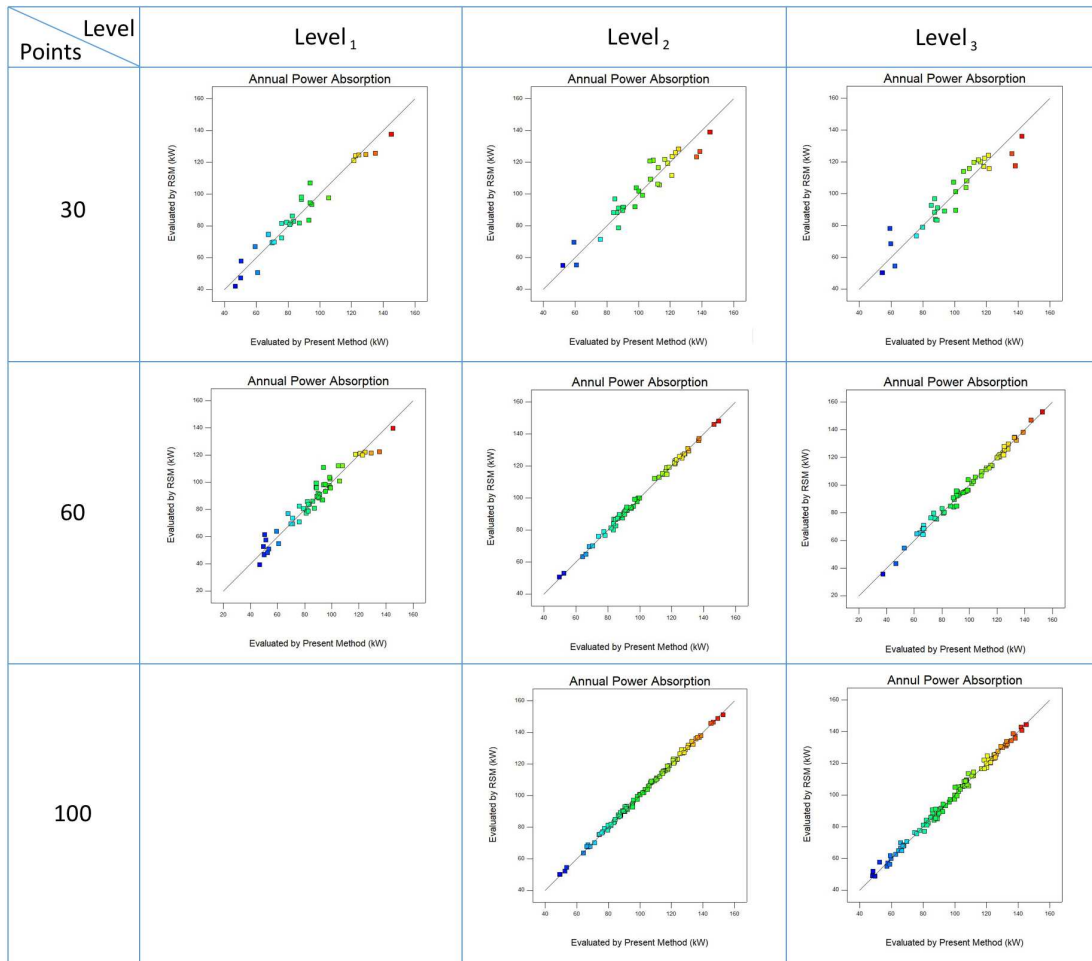


Figure 5.3: Verification of RSM

rors between the results achieved from numerical simulation and the surrogate model fitting were computed, as presented in Table 5.6.

Table 5.6: Average error

Number of Sampling Points	<i>Level</i> <sub>1</sub>	<i>Level</i> <sub>2</sub>	<i>Level</i> <sub>3</sub>
30	5.51%	5.85%	6.10%
60	5.31%	2.07%	2.11%
100	-	1.87%	1.67%

Similar to the observations from the adjusted R-squared values, sampling points more than 60 are more desirable and the levels of design variables should be greater than 3.

### 5.5.3 Optimization Results

In the optimization of SeaWEED, the design variables were discretized according to level combination *Level*<sub>3</sub> (see Table 5.3) and 100 sample points were selected. A 4<sup>th</sup>-order polynomial function was found using the Design Expert software, which can be expressed as

$$P_{Smax}^A(L_{T1}, L_{T2}, L_{T3}, D) = \sum_{i=1}^{n_p} w_i \Phi_i \quad (5.8)$$

where  $n_p$  is the total number of terms in the polynomial function,  $w_i$  is the coefficient for the  $i$ th term,  $\Phi_i$  is the  $i$ th element in  $\{\Phi\}$ , which includes a set of terms with an

Table 5.7: Optimal parameters (full-scale)

Parameter	Value
$L_{T1}$ (m)	47.13
$L_{T2}$ (m)	70.69
$L_{T3}$ (m)	45.68
$D$ (m)	2.48
$d_1$ (Nm s)	$7.893 \times 10^8$
$d_2$ (Nm s)	$6.019 \times 10^8$

order less than or equal to four

$$\{\Phi\} = \{1, L_{T1}, L_{T2}, L_{T3}, D, L_{T1}, L_{T2}, \dots, L_{T1}^4, L_{T2}^4, L_{T3}^4, D^4\} \quad (5.9)$$

The response surfaces in terms of draft and body length for annual power absorption are presented in Fig. 5.4 based on the verified polynomial functions.

As the maximum annual power absorption is the only desired response in the current problem, the desirability function is to maximize the annual power absorption. The optimal combination and its corresponding parameters are listed in Table 5.7. The predicted maximum annual power absorption is 149.56 kW. For verification, the optimal case was also simulated using the present program, and the computed result is 152.71 kW, 2.1% different from the one by the response surface method.

The optimum power capture width of SeaWEED is 6.08 m. The power matrix, calculated using Eq. 4.18 at each sea state,  $(H_s, T_p)$ , with the optimal combination of parameters, is presented in Fig. 5.5. It is noted that when the relative pitch angle is

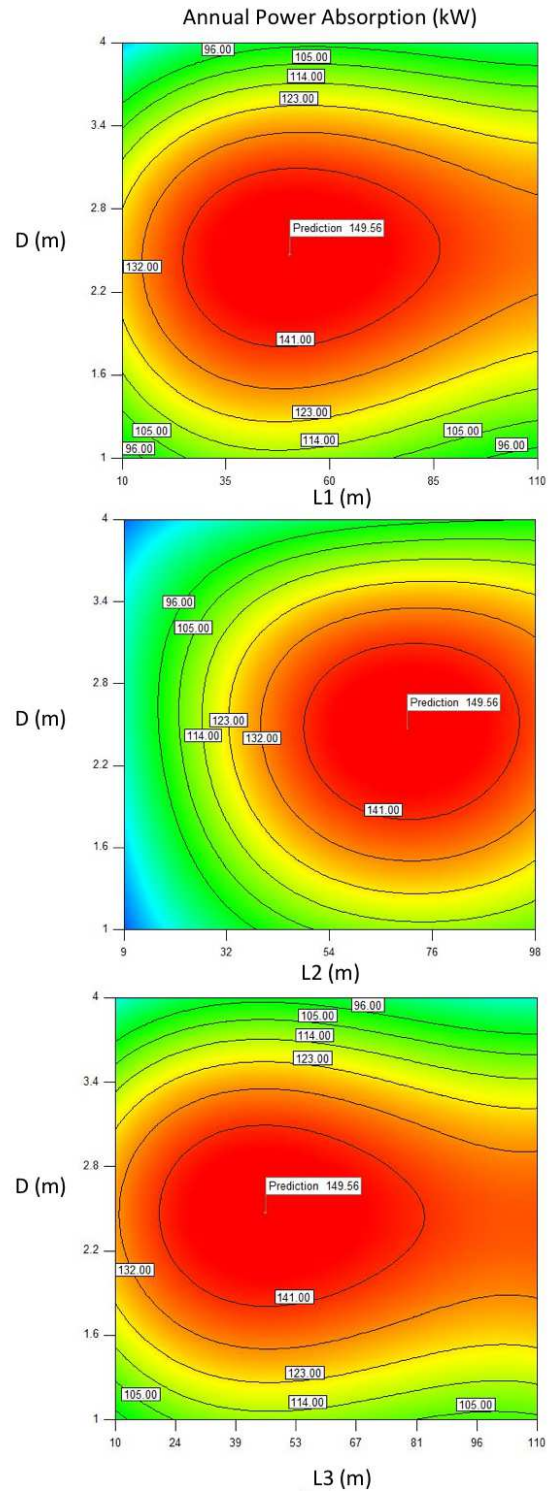


Figure 5.4: Response Surfaces for Annual Power Absorption

greater than the constraint angle in the optimization process, it was set to 30 degrees.

Power (kW)		Tp (s)												
		4.5	5.5	6.5	7.5	8.5	9.5	10.5	11.5	12.5	13.5	14.5	15.5	16.5
Hs (m)	0.25	0.455	0.743	0.755	1.257	1.809	1.991	2.041	1.896	1.549	1.302	1.040	0.816	0.696
	0.75	4.098	6.683	6.791	11.316	16.282	17.918	18.371	17.060	13.938	11.715	9.362	7.342	6.263
	1.25	11.383	18.564	18.863	31.434	45.229	49.771	51.030	47.389	38.716	32.541	26.005	20.396	17.398
	1.75	22.310	36.385	36.972	61.611	88.648	97.551	100.019	92.882	75.883	63.781	50.970	39.975	34.100
	2.25	36.881	60.146	61.117	101.848	146.541	161.259	165.338	153.539	125.440	105.434	84.257	66.081	56.370
	2.75	55.093	89.848	91.298	152.143	218.906	240.892	246.987	229.361	187.385	157.501	125.865	98.714	84.207
	3.25	76.948	125.490	127.516	212.497	305.745	336.453	344.965	320.348	261.720	219.980	175.795	137.874	117.611
	3.75	102.446	167.072	169.770	282.910	407.057	447.940	459.273	426.499	348.444	292.873	234.047	183.560	156.583
	4.25	131.586	214.595	218.060	363.382	522.842	575.355	589.910	547.814	447.557	376.180	300.621	235.772	201.122
	4.75	164.369	268.058	272.386	453.913	653.101	718.695	736.878	684.293	559.059	469.899	375.516	294.511	251.229
	5.25	200.794	327.461	332.749	554.503	797.832	877.963	900.175	835.937	682.950	574.032	458.732	359.777	306.903
	5.75	240.862	392.805	399.148	665.153	957.037	1053.158	1079.801	1002.746	819.230	688.578	550.271	431.569	368.144
	6.25	284.572	464.089	471.583	785.861	1130.715	1244.279	1275.758	1184.718	967.900	813.537	650.131	509.888	434.953
	6.75	331.925	541.314	550.054	916.628	1318.865	1451.327	1488.044	1381.855	1128.958	948.910	758.313	594.733	507.329
	7.25	382.920	624.478	634.562	1057.455	1521.489	1674.302	1716.659	1594.157	1302.406	1094.695	874.816	686.105	585.273

Figure 5.5: Power Matrix of SeaWEED

# Chapter 6

## Conclusions and Future Work

In this thesis, the experimental, numerical and optimization studies have been conducted to evaluate the performance of a multi-body floating WEC, SeaWEED.

Model tests of a 1:35 scale second generation SeaWEED model were conducted at the towing tank of MUN. A friction damper was designed to mimic the PTO unit. Detailed description of the experiment is presented.

To simulate the dynamics and power-take-off (PTO) of SeaWEED, potential-flow based time- and frequency-domain programs with the Lagrange multiplier approach have been developed. In the time-domain program, nonlinear Froude-Krylov forces were considered. Good agreement was achieved comparing the numerical results to the experimental data.

Optimization studies were further conducted involving the damping coefficients of the PTO systems, the lengths of the body segments and the drafts of the device. The uniform design method was applied to select sample points, and the response surface method was utilized to construct the surrogate model. The desirability optimization

method is applied to search for the optimum response. The optimal combination of PTO damping coefficients and geometrical parameters was determined for an intended site off the Cork Harbour in Ireland.

Optimization of SeaWEED for any operation locations can be performed in a straightforward way using the present method. The time-domain program can be extended to account for more nonlinearity by considering the exact body movements. Coupled analysis of SeaWEED with mooring lines can be further investigated by incorporating mooring line dynamics programs with the present time-domain code.

# Bibliography

- [1] AW-Energy. Waveroller. <http://aw-energy.com/waveroller/>.
- [2] A. Babarit, A. H. Clément, and J.-C. Gilloteaux. Optimization and time-domain simulation of the searev wave energy converter. In *ASME 2005 24th International Conference on Offshore Mechanics and Arctic Engineering*, pages 703–712. American Society of Mechanical Engineers, 2005.
- [3] D. Baraff. Linear-time dynamics using lagrange multipliers. In *Proceedings of the 23rd annual conference on Computer graphics and interactive techniques*, pages 137–146. ACM, 1996.
- [4] D. Baş and I. H. Boyacı. Modeling and optimization i: Usability of response surface methodology. *Journal of food engineering*, 78(3):836–845, 2007.
- [5] G. E. Box and K. B. Wilson. On the experimental attainment of optimum conditions. *Journal of the Royal Statistical Society: Series B (Methodological)*, 13(1):1–38, 1951.
- [6] E. Catto. Modeling and solving constraints. In *Game Developers Conference*, page 16, 2009.

- [7] S. Chen, C. F. Cowan, and P. M. Grant. Orthogonal least squares learning algorithm for radial basis function networks. *IEEE Transactions on neural networks*, 2(2):302–309, 1991.
- [8] S. M. Clarke, J. H. Griebisch, and T. W. Simpson. Analysis of support vector regression for approximation of complex engineering analyses. *Journal of mechanical design*, 127(6):1077–1087, 2005.
- [9] A. Clément, P. McCullen, A. Falcão, A. Fiorentino, F. Gardner, K. Hammarlund, G. Lemonis, T. Lewis, K. Nielsen, S. Petroncini, et al. Wave energy in europe: current status and perspectives. *Renewable and sustainable energy reviews*, 6(5):405–431, 2002.
- [10] C. J. Cleveland and C. G. Morris. *Handbook of energy: chronologies, top ten lists, and word clouds*. Elsevier, 2013.
- [11] Y. Dai, Y. Chen, and L. Xie. A study on a novel two-body floating wave energy converter. *Ocean Engineering*, 130:407–416, 2017.
- [12] D. G. Danmeier. *A higher-order method for large-amplitude simulations of bodies in waves*. PhD thesis, Massachusetts Institute of Technology, 1999.
- [13] G. Dantzig. *Linear programming and extensions*. Princeton university press, 2016.
- [14] A. Day, A. Babarit, A. Fontaine, Y.-P. He, M. Kraskowski, M. Murai, I. Penesis, F. Salvatore, and H.-K. Shin. Hydrodynamic modelling of marine renewable energy devices: a state of the art review. *Ocean Engineering*, 108:46–69, 2015.

- [15] C. De Boor and A. Ron. On multivariate polynomial interpolation. *Constructive Approximation*, 6(3):287–302, 1990.
- [16] J. E. Dennis, Jr and J. J. Moré. Quasi-newton methods, motivation and theory. *SIAM review*, 19(1):46–89, 1977.
- [17] G. Derringer and R. Suich. Simultaneous optimization of several response variables. *Journal of quality technology*, 12(4):214–219, 1980.
- [18] H. Dette and A. Pepelyshev. Generalized latin hypercube design for computer experiments. *Technometrics*, 52(4):421–429, 2010.
- [19] B. Drew, A. Plummer, and M. N. Sahinkaya. A review of wave energy converter technology. *Proceedings of the Institution of Mechanical Engineers, Part A: Journal of Power and Energy*, 223(8):887–902, 2009.
- [20] R. Eberhart and J. Kennedy. A new optimizer using particle swarm theory. In *Micro Machine and Human Science, 1995. MHS'95., Proceedings of the Sixth International Symposium on*, pages 39–43. IEEE, 1995.
- [21] K. Edwards, M. Mekhiche, et al. Ocean power technologies powerbuoy®: System-level design, development and validation methodology. 2014.
- [22] A. d. O. Falcão. The shoreline owc wave power plant at the azores. In *Fourth European Wave Energy Conference, Aalborg, Denmark, Dec*, pages 4–6, 2000.
- [23] K.-T. Fang, R. Li, and A. Sudjianto. *Design and modeling for computer experiments*. Chapman and Hall/CRC, 2005.

- [24] K.-T. Fang, D. K. Lin, P. Winker, and Y. Zhang. Uniform design: theory and application. *Technometrics*, 42(3):237–248, 2000.
- [25] X. Feng and W. Bai. Hydrodynamic analysis of marine multibody systems by a nonlinear coupled model. *Journal of Fluids and Structures*, 70:72–101, 2017.
- [26] A. Fischer. A special newton-type optimization method. *Optimization*, 24(3-4):269–284, 1992.
- [27] A. Forrester, A. Sobester, and A. Keane. *Engineering design via surrogate modelling: a practical guide*. John Wiley & Sons, 2008.
- [28] J. H. Friedman. Multivariate adaptive regression splines. *The annals of statistics*, pages 1–67, 1991.
- [29] J. Goggins and W. Finnegan. Shape optimisation of floating wave energy converters for a specified wave energy spectrum. *Renewable Energy*, 71:208–220, 2014.
- [30] M. Gonzalez. Wave and tidal energy experiments in san francisco and santa cruz. <http://www.outsidelands.org/wave-tidal.php>.
- [31] S. Grossberg. Nonlinear neural networks: Principles, mechanisms, and architectures. *Neural networks*, 1(1):17–61, 1988.
- [32] K. Hasselmann. Measurements of wind wave growth and swell decay during the joint north sea wave project (jonswap). *Dtsch. Hydrogr. Z.*, 8:95, 1973.
- [33] J. H. Holland. Genetic algorithms. *Scientific american*, 267(1):66–73, 1992.

- [34] R. Hooke and T. A. Jeeves. “direct search” solution of numerical and statistical problems. *Journal of the ACM (JACM)*, 8(2):212–229, 1961.
- [35] IEA. Ocean energy systems. <https://www.ocean-energy-systems.org/>.
- [36] R. Jin, W. Chen, and A. Sudjianto. An efficient algorithm for constructing optimal design of computer experiments. In *ASME 2003 International Design Engineering Technical Conferences and Computers and Information in Engineering Conference*, pages 545–554. American Society of Mechanical Engineers, 2003.
- [37] B. Jones, R. T. Silvestrini, D. C. Montgomery, and D. M. Steinberg. Bridge designs for modeling systems with low noise. *Technometrics*, 57(2):155–163, 2015.
- [38] V. R. Joseph. Space-filling designs for computer experiments: A review. *Quality Engineering*, 28(1):28–35, 2016.
- [39] V. R. Joseph, Y. Hung, and A. Sudjianto. Blind kriging: A new method for developing metamodels. *Journal of mechanical design*, 130(3):031102, 2008.
- [40] S. Khaleghi and R. K. Moghaddam. Parameters optimization to maximize the wave energy extraction. In *Technology, Communication and Knowledge (ICTCK), 2015 International Congress on*, pages 260–267. IEEE, 2015.
- [41] J. P. Kofoed and P. Frigaard. Hydraulic evaluation of the leancon wave energy converter. *Department of Civil Engineering, Aalborg University, Aalborg. DCE Technical Reports*, 2008.

- [42] J. P. Kofoed, P. Frigaard, E. Friis-Madsen, and H. C. Sørensen. Prototype testing of the wave energy converter wave dragon. *Renewable energy*, 31(2):181–189, 2006.
- [43] D. Krige. A statistical approach to some mine valuations and allied problems at the witwatersrand. master’s thesis. university of witwatersrand. 1951. *Google Scholar*, 1951.
- [44] V. Kůrková. Kolmogorov’s theorem and multilayer neural networks. *Neural networks*, 5(3):501–506, 1992.
- [45] P. Langley and H. A. Simon. Applications of machine learning and rule induction. *Communications of the ACM*, 38(11):54–64, 1995.
- [46] LeanCon. The leancon wave energy device. <http://www.leancon.com/>.
- [47] C.-H. Lee and J. Newman. An assessment of hydroelasticity for very large hinged vessels. *Journal of fluids and structures*, 14(7):957–970, 2000.
- [48] R. Lekivetz and B. Jones. Fast flexible space-filling designs for nonrectangular regions. *Quality and Reliability Engineering International*, 31(5):829–837, 2015.
- [49] Q. Li, L.-J. Sun, X.-F. Gong, Y. Wang, and X.-L. Zhao. Simultaneous optimization of multiple response variables for the gelatin-chitosan microcapsules containing angelica essential oil. *Iranian journal of pharmaceutical research: IJPR*, 16(1):50, 2017.
- [50] Y. Li, H. Peng, W. Qiu, B. Lundrigan, and T. Gardiner. Hydrodynamic analysis and optimization of a hinged type wave energy converter. In *ASME 2016*

- 35th International Conference on Ocean, Offshore and Arctic Engineering*, pages V006T09A024–V006T09A024. American Society of Mechanical Engineers, 2016.
- [51] B. Lundrigan. Competitive analysis, tech. rep. *Grey Island Energy Inc.*, 2013.
- [52] L. Margheritini, D. Vicinanza, and P. Frigaard. Ssg wave energy converter: Design, reliability and hydraulic performance of an innovative overtopping device. *Renewable Energy*, 34(5):1371–1380, 2009.
- [53] G. Matheron. Principles of geostatistics. *Economic geology*, 58(8):1246–1266, 1963.
- [54] M. D. McKay, R. J. Beckman, and W. J. Conover. A comparison of three methods for selecting values of input variables in the analysis of output from a computer code. *Technometrics*, 42(1):55–61, 1979.
- [55] G. Mørk, S. Barstow, A. Kabuth, and M. T. Pontes. Assessing the global wave energy potential. In *Proc. of 29th International Conference on Ocean, Offshore and Arctic Engineering, ASME, paper*, volume 20473, 2010.
- [56] M. D. Morris and T. J. Mitchell. Exploratory designs for computational experiments. *Journal of statistical planning and inference*, 43(3):381–402, 1995.
- [57] F. Mouwen. Presentation on wavebob to engineers ireland. *December, 9th*, 2008.
- [58] R. H. Myers, D. C. Montgomery, et al. *Response surface methodology: process and product optimization using designed experiments*, volume 4. Wiley New York, 1995.

- [59] J. Newman. Wave effects on deformable bodies. *Applied ocean research*, 16(1):47–59, 1994.
- [60] H. Niederreiter. Quasi-monte carlo methods and pseudo-random numbers. *Bulletin of the American Mathematical Society*, 84(6):957–1041, 1978.
- [61] NRC. Ocean engineering basin of national research council-institute. <https://ittc.info/media/5690/offshore-engineering-basin.pdf>.
- [62] D. M. Olsson and L. S. Nelson. The nelder-mead simplex procedure for function minimization. *Technometrics*, 17(1):45–51, 1975.
- [63] A. B. Owen. Controlling correlations in latin hypercube samples. *Journal of the American Statistical Association*, 89(428):1517–1522, 1994.
- [64] M. Ó’Catháin, B. J. Leira, J. V. Ringwood, and J.-C. Gilloteaux. A modelling methodology for multi-body systems with application to wave-energy devices. *Ocean Engineering*, 35(13):1381–1387, 2008.
- [65] A. Pecher and J. P. Kofoed. *Handbook of Ocean Wave Energy*. Springer, 2017.
- [66] D. Pizer, C. Retzler, and R. Yemm. The opd pelamis: experimental and numerical results from the hydrodynamic work program. In *Proceedings of Fourth European wave energy conference, Aalborg*, pages 227–33, 2000.
- [67] P. Z. Qian, B. Tang, and C. J. Wu. Nested space-filling designs for computer experiments with two levels of accuracy. *Statistica Sinica*, pages 287–300, 2009.
- [68] P. Z. Qian and C. J. Wu. Sliced space-filling designs. *Biometrika*, 96(4):945–956, 2009.

- [69] W. Qiu and H. H. Peng. Numerical solution of body-exact problem in the time domain. *Journal of Ship Research*, 57(1):13–23, 2013.
- [70] E. Renzi, K. Doherty, A. Henry, and F. Dias. How does oyster work? the simple interpretation of oyster mathematics. *European Journal of Mechanics-B/Fluids*, 47:124–131, 2014.
- [71] J. Sacks, S. B. Schiller, and W. J. Welch. Designs for computer experiments. *Technometrics*, 31(1):41–47, 1989.
- [72] J. Sacks, W. J. Welch, T. J. Mitchell, and H. P. Wynn. Design and analysis of computer experiments. *Statistical science*, pages 409–423, 1989.
- [73] S. H. Salter. Wave power. *Nature*, 249(5459):720–724, 1974.
- [74] Seabased-technology. Seabased technology. <https://www.seabased.com/>.
- [75] SmartBay. 2015 smartbay ireland latest data. <https://www.smartbay.ie/>.
- [76] L. Sun, P. Stansby, J. Zang, E. C. Moreno, and P. H. Taylor. Linear diffraction analysis for optimisation of the three-float multi-mode wave energy converter m4 in regular waves including small arrays. *Journal of Ocean Engineering and Marine Energy*, 2(4):429–438, 2016.
- [77] L. Sun, R. E. Taylor, and Y. S. Choo. Responses of interconnected floating bodies. *The IES Journal Part A: Civil & Structural Engineering*, 4(3):143–156, 2011.
- [78] L. Sun, R. E. Taylor, and Y. S. Choo. Multi-body dynamic analysis of float-over installations. *Ocean Engineering*, 51:1–15, 2012.

- [79] Z. Sun, J. Wang, R. Li, and C. Tong. Lif: A new kriging based learning function and its application to structural reliability analysis. *Reliability Engineering & System Safety*, 157:152–165, 2017.
- [80] B. Tang. Orthogonal array-based latin hypercubes. *Journal of the American statistical association*, 88(424):1392–1397, 1993.
- [81] V. Toropov, A. Filatov, and A. Polynkin. Multiparameter structural optimization using fem and multipoint explicit approximations. *Structural optimization*, 6(1):7–14, 1993.
- [82] Y. Torre-Enciso, I. Ortubia, L. L. de Aguilera, and J. Marqués. Mutriku wave power plant: from the thinking out to the reality. In *Proceedings of the 8th European wave and tidal energy conference, Uppsala, Sweden*, volume 710, pages 319–329, 2009.
- [83] D. Vicinanza and P. Frigaard. Wave pressure acting on a seawave slot-cone generator. *Coastal Engineering*, 55(6):553–568, 2008.
- [84] J. Wheeler et al. Methods for calculating forces produced by irregular waves. In *Offshore Technology Conference*. Offshore Technology Conference, 1969.
- [85] D. Whitley. A genetic algorithm tutorial. *Statistics and computing*, 4(2):65–85, 1994.
- [86] A. Witkin. An introduction to physically based modeling: Constrained dynamics. *Robotics Institute*, 1997.

- [87] K. Q. Ye. Orthogonal column latin hypercubes and their application in computer experiments. *Journal of the American Statistical Association*, 93(444):1430–1439, 1998.
- [88] R. Yemm, D. Pizer, C. Retzler, and R. Henderson. Pelamis: experience from concept to connection. *Phil. Trans. R. Soc. A*, 370(1959):365–380, 2012.